TOPICAL REVIEW

Nuclear diagnostics for Inertial Confinement Fusion (ICF) plasmas

View the article online for updates and enhancements.

IOP ebooks™

Bringing you innovative digital publishing with leading voices to create your essential collection of books in STEM research.

Start exploring the collection - download the first chapter of every title for free.

Topical Review

Nuclear diagnostics for Inertial Confinement Fusion (ICF) plasmas

J A Frenje

Massachusetts Institute of Technology, Cambridge, MA 02139, United States of America

E-mail: jfrenje@psfc.mit.edu

CrossMark

Abstract

The field of nuclear diagnostics for Inertial Confinement Fusion (ICF) is broadly reviewed from its beginning in the seventies to present day. During this time, the sophistication of the ICF facilities and the suite of nuclear diagnostics have substantially evolved, generally a consequence of the efforts and experience gained on previous facilities. As the fusion yields have increased several orders of magnitude during these years, the quality of the nuclear-fusion-product measurements has improved significantly, facilitating an increased level of understanding about the physics governing the nuclear phase of an ICF implosion. The field of ICF has now entered an era where the fusion yields are high enough for nuclear measurements to provide spatial, temporal and spectral information, which have proven indispensable to understanding the performance of an ICF implosion. At the same time, the requirements on the nuclear diagnostics have also become more stringent. To put these measurements into context, this review starts by providing some historical remarks about the field of ICF and the role of nuclear diagnostics, followed by a brief overview of the basic physics that characterize the nuclear phase and performance of an ICF implosion. A technical discussion is subsequently presented of the neutron, gamma-ray, charged-particle and radiochemistry diagnostics that are, or have been, routinely used in the field of ICF. This discussion is followed by an elaboration of the current view of the next-generation nuclear diagnostics. Since the seventies, the overall progress made in the areas of nuclear diagnostics and scientific understanding of an ICF implosion has been enormous, and with the implementation of new high-fusion-yield facilities world-wide, the next-generation nuclear diagnostics will play an even more important role for decades to come.

Keywords: nuclear diagnostics, neutron, gamma-ray, charged particle, plasma, Inertial Confinement Fusion, ICF

(Some figures may appear in colour only in the online journal)

1. Introduction

1.1. Inertial Confinement Fusion (ICF)—historical remarks

The history of ICF can be traced back to a meeting organized by Edward Teller in 1957, which focused on the use of hydrogen bombs for peaceful purposes. One of the outcomes of that meeting was the initiation of John Nuckolls work on significantly scaling down the secondary (the fusion part of a hydrogen bomb), while still generating energy gain. This early work pointed to the idea that a small spherical capsule filled with deuterium–tritium (DT) fuel, positioned inside a small cylindrical hohlraum, could be imploded by x-rays produced in the hohlraum [1, 2]. However, at the time it was not clear how to heat the hohlraum and generate x-rays and drive the capsule. With the introduction of the laser in 1960, it became clear that the laser represented a suitable driver for ICF applications. As a result, a large body of theoretical and computational work was conducted in the United States (US), Europe, Japan and the Union of Soviet Socialist Republics (USSR) in the 60s and early 70s, which laid the foundation

for laser-driven ICF, both in direct-drive mode (where lasers directly illuminate the capsule), and indirect-drive mode (where lasers illuminate the inside of a hohlraum for production of x-rays that drive the capsule). Other types of driver concepts were also investigated such as electrons, heavy ions and magnetic fields [3, 4]. This era culminated in 1972 with the first unclassified ICF paper 'Laser Compression of Matter to Super-High Densities' published by Nuckolls *et al* in Nature [5], which formulates the foundation for the direct-drive ICF scheme where 100 kJ–1 MJ lasers are used to implode a millimeter-sized spherical capsule, filled with DT gas, to densities and temperatures high enough for significant thermonuclear fusion, ignition and energy gain to occur. The scheme and the many challenges presented in this seminal paper are still relevant today.

After Nuckolls' paper was published, several large-scaled (hundreds of joule) laser facilities were built or used to explore the spherical implosion concept. In Japan, the Gekko-II laser was used to conduct spherical implosion experiments in 1973 [6, 7]. In 1974, the KMS Fusion in the US used a two-beam laser system, capable of delivering up to 200 J in 100 ps pulse, to irradiate a set of DT gas-filled capsules, which generated thermonuclear conditions and neutron yields up to $\sim 10^7$ [8]. At Lawrence Livermore National Laboratory (LLNL), similar experiments were conducted in 1974 with the single-beam JANUS laser, and in 1975 neutron yields in excess of 10^8 were generated [9]. By early 1976, the upgraded 2-beam ARGUS laser generated ion temperatures of ~ 10 keV and neutron yields up to $\sim 10^{10}$, which represented a big step forward in terms of performance. At about the same time, the six laser-beam ZETA system was built at the Laboratory for Laser Energetics (LLE) at the University of Rochester, where a series of symmetrical implosion experiments utilizing gas-filled, thin-glass capsules was carried out. These experiments generated impressive results in terms of implosion symmetry and neutron yields up to 1.5×10^9 [10].

The downside with these first experiments was that they were performed with thin-glass capsules that could not generate the required densities for ignition to occur. The program at LLNL was therefore redirected toward implosions based on isentropic compression required for high convergence and high fuel densities. In 1978, fuel densities of order $10\times$ liquid density were achieved in experiments with the 2 kJ ARGUS laser, and about a year later fuel compression of about $100\times$ was achieved with the 10 kJ SHIVA laser [11]. The ion temperature in these experiments was low (~ 0.5 keV) to maximize fuel density but to provide sufficient thermonuclear yields for diagnostics purposes [11]. Several experiments at SHIVA also explored the indirect-drive concept using hohlraums.

The results from these first experiments were very encouraging and led to the development of several new, larger ICF facilities around the world, such as NOVA in the US [12], Gekko-XII in Japan [13], Phebus in France [14], ISKRA-4 (followed by ISKRA-5) in the USSR [15, 16], SG-I in China [17] and OMEGA-24 in the US [18]. Hot-spot experiments at Gekko-XII generated impressive results, including ion temperatures of ~ 10 keV and neutron yields of

$\sim 10^{13}$ [19]. At NOVA, the first fully integrated indirect-drive experiments were conducted in 1985 [20], and in 1990, experiments with the upgraded NOVA laser symmetrically compressed DT implosions about $100\times$ in a 300 eV hohlraum with little preheat. The enhanced NOVA capability also produced neutron yields up to $\sim 10^{13}$, which were made possible by increasing the energy output per beam and by substantially improving the suite of diagnostics. In parallel, a series of implosion experiments with the OMEGA-24 system demonstrated $100–200\times$ liquid-DT density in 1988 [21], which was facilitated in part by implementing and using an extensive array of diagnostics. In 1996, OMEGA-24 was upgraded to OMEGA-60 [22] to achieve better uniformity and to lay the foundation for validating the direct-drive approach for achieving ignition.

The findings from the experiments in the 80s and early 90s were reviewed by the National Academy of Science that issued the Koonin Report [23], which stated that most milestones in the efforts in achieving the required implosion conditions had been met to initiate a large-scaled ignition program. In that report, it was concluded that the predicted fuel densities were achieved, while neutron yields were orders of magnitude lower than predicted, indicating that the formation of the hot spot and resulting ion temperature were impeded mainly by Rayleigh–Taylor (RT) instabilities. It was also concluded that the required conditions for ignition could not be achieved with the facilities at hand, which initiated the effort of building the MJ-class lasers: the National Ignition Facility (NIF) [24] at LLNL, and the Laser Mega Joule (LMJ) [25] in France; which are primarily designed for indirect-drive experiments. At the NIF, the first light was obtained in 2003, while the full operation of the system started in 2009, with the first phase being the National Ignition Campaign that produced highest fuel areal density (ρR) to date (~ 1.6 g cm^2) [26]. This campaign was followed by several campaigns that involved more stable implosions, which led to a hot-spot pressures in excess of 350 Gbar and record neutron yields of $\sim 2 \times 10^{16}$ [27, 28]. The LMJ system started partial operation in 2014. In parallel, a cryogenic DT campaign at OMEGA-60 was initiated in 2006 to validate the direct-drive approach for achieving ignition. In the subsequent years, several important milestones were achieved, culminating in a ρR of ~ 300 mg cm^{-2} [29], hot-spot pressure of 56 Gbar and neutron yields in excess of 10^{14} [30].

The Chinese ICF program continued to advance the SG-series. In 2001 the SG-II facility was operated at 6 kJ, and in 2014 the SG-II upgrade operated at 24 kJ [31]. The 48-beam, 180 kJ SG-III laser facility was commissioned in 2015 and subsequently started operation [32]. In addition, the MJ-class SG-IV laser represents the next step in China's ICF program, and is being designed to explore ignition and burn [33]. This facility is projected to be in operation within the next decade. In Russia, the 192-beam, 2.8 MJ UFL-2M laser is currently being built at the Russian Federal Nuclear Center in Sarov [34]. This system is a 2ω laser system for direct-drive experiments.

The fast-ignition approach in which the fuel compression is decoupled from the heating of the hot spot [35], has been

explored in parallel with the standard hot-spot approach. Fast ignition experiments have been conducted at Gekko-XII, culminating in neutron yields up to 3.5×10^7 [36, 37]. The facilities that are being implemented and have been proposed to pursue fast ignition are Fast Ignition Research Experiment at Osaka University [38], and High Power laser Energy Research facility in the United Kingdom (UK) [39], respectively. If fast-ignition approach is successfully implemented and ignition is achieved, it would in principle lower the amount of energy required to be coupled to the capsule by an order of magnitude.

Another promising approach that has recently emerged in the field of ICF is the Magnetized Liner Inertial Fusion (MagLIF) method [40]. This method, which was developed at Sandia National Laboratory, uses imploding magnetic fields of a cylindrical beryllium liner (Z-pinch) combined with a heater laser beam. The MagLIF concept is today mainly operating with pure D_2 fuel, and has to date generated up to $\sim 10^{13}$ neutrons [41]. The long-term plan for the MagLIF approach is to gradually switch over to DT fuel operation.

1.2. Role of nuclear diagnostics

In retrospect, each decade has displayed the development of ICF facilities and nuclear diagnostics that were orders of magnitude more capable than those used during the preceding decade. This is generally a consequence of the fact that the efforts, lessons learned, and experience gained on previous facilities enabled more sophisticated diagnostics on the next-generation facilities. Higher fusion yields also facilitated higher-quality measurements, which facilitated an increased level of understanding about the physics governing the nuclear phase of an ICF implosion. This in turn provided essential guidance of the ICF programs, resulting in improvements in the fusion yield. The field of ICF has now entered an era where the fusion yields are high enough for unprecedented nuclear measurements with spatial, temporal or spectral information, which are indispensable in understanding the performance of an ICF implosion. With the implementation of new high-fusion-yield facilities worldwide, the next-generation nuclear diagnostics will play an even more important role for decades to come.

2. Brief overview of the physics governing the nuclear phase of an ICF implosion

The concept of an ICF implosion involves a spherical capsule made of either plastic (CH), high-density carbon (HDC), or beryllium (Be) that is filled with milligrams of DT[1] fuel in the form of gas at vapor pressure at the center surrounded by a cryogenic ice-layer on the inside of the capsule [42][2]. In the case of laser-driven ICF, the energy from the driver is delivered to the outer part of the capsule (or ablator), which

heats and radially expands outward. As the outer part of the ablator expands, the remaining inner part is forced inward to conserve momentum. This process is generally done quasi-isentropically [42, 43], and at peak compression the fuel is nearly isobaric and typically represented by two regions: a hot central plasma (called hot spot), containing a small fraction of the fuel, and a denser (and colder) fuel-shell surrounding the hot spot. The fuel-shell has several functions: first, it compresses and heats the hot spot by acting as a piston, secondly, it provides inertial confinement, and thirdly, it traps the *dt*-alphas for self-heating. At peak compression, the fusion process is initiated by several carefully tailored shocks that converge at the center of the implosion, significantly raising the ion temperature and density of the hot spot. If the temperature and density are high enough, hot-spot ignition occurs. In addition, if the ρR of the surrounding fuel-shell is sufficient to stop majority of the *dt*-alphas and the fuel is kept together for long enough time, a thermonuclear burn wave will propagate through the main fuel-shell. The energy coupled to the hot spot is small (a few kJ), but if hot-spot ignition is followed by burn of the main fuel, the energy output is amplified significantly.

As discussed in the literature [44], a simple form that represents the ignition condition for a steady-state plasma can be derived by balancing the alpha-power density with the power-loss density mainly due to heat loss caused by fuel-shell expansion and thermal conduction[3]. Often referred to a Lawson-type criterion, the ideal ignition condition is expressed as

$$\varepsilon_\alpha \frac{n^2}{4} \langle \sigma v \rangle = \varepsilon_\alpha \frac{P^2}{16} \frac{\langle \sigma v \rangle}{T_i^2} > \frac{3}{2} \frac{P}{\tau_E}, \qquad (2.1)$$

where ε_α is the kinetic energy of the DT-alpha, n is the total ion-number density, $\langle \sigma v \rangle$ is the fusion reactivity for a thermal plasma, P is the hot-spot pressure, T_i is the hot-spot ion temperature, and τ_E is the energy-confinement time[4]. Here, it is assumed that the pressure profile is constant in the hot spot and thus can be expressed as $P = 2nT_i$. Equation (2.1) can be rewritten as

$$P\tau_E > \frac{24T_i^2}{\varepsilon_\alpha \langle \sigma v \rangle}. \qquad (2.2)$$

As shown by equation (2.2), the Lawson criterion depends on $T_i{}^2$. In the case of an ICF implosion, the $T_i{}^2/\langle \sigma v \rangle$ is minimized for a T_i of ~ 13 keV for the *dt* reaction [45]. However, to achieve this temperature using the spherical-implosion concept, the implosion velocity must be ~ 700 km s^{-1}, which is unrealistically high because the implosion is hydrodynamically unstable and severely breaks up in-flight. A lower implosion velocity of ~ 400 km s^{-1}, which generates T_i of ~ 5 keV, is optimal for a stable implosion. With these implosion parameters, the ideal ignition condition $P\tau_E$ is

---

[1] D and T represent a deuterium and tritium atom, respectively. This should be contrasted to d and t that represent a deuteron and triton, respectively.
[2] In the case of MagLIF, the implosion involves a cylindrical Be liner filled with pure D_2 gas in most experiments.

[3] When the density in the surrounding fuel-shell is high, most of the radiation is absorbed in the fuel-shell and the energy is recycled back into the hot spot by increasing the ablation of the inner surface of the fuel-shell.
[4] τ_E represents the characteristic plasma-energy relaxation time due to electron heat conduction.

$\sim$20 atm s (and not $P\tau_{E,\min} \sim 8$ atm s, which is required for a T_i of $\sim$13 keV).

To assess the performance of an ICF implosion and how it compares to the ideal ignition condition, the experimental $P\tau$ is often normalized to the ideal ignition condition $P\tau_{E,\min}$. This ratio is called the ignition parameter (χ) [45]. During the deceleration phase of the implosion, the kinetic energy of the fuel-shell is converted into hot-spot thermal energy, which means that the hot-spot pressure scales as $P \sim mv^2/R^3$, where $m \sim \rho R(R^2)$ represents the fuel-shell mass, R represents the fuel radius, and $v \sim R/\tau$ is the implosion velocity (where τ represents the implosion time scale). Using these relations, χ can be expressed as

$$\chi = \frac{P\tau}{P\tau_{E,\,\min}} \sim \rho R \cdot v \cdot T_i, \qquad (2.3)$$

where ρR is the burn-averaged areal density of the fuel-shell, and T_i is the burn-averaged ion temperature. Here, it is assumed that $\langle \sigma v \rangle$ is approximately proportional to $T_i{}^3$ in the range of 3.5–7.0 keV. On the basis of analytical and numerical modeling, Betti $et\ al$ showed that the implosion velocity v in equation (2.3) can be expressed as $T_i{}^{0.8}/\rho R^{0.2}$ [45], which leads to

$$\chi \approx \rho R^{0.8} \left(\frac{T_i}{4.7} \right)^{1.6}, \qquad (2.4)$$

and

$$P\tau > 8 \cdot (\rho R \cdot T_i)^{0.8}, \qquad (2.5)$$

where $P\tau$ is given in atm s, ρR is given in g cm^{-2} and T_i is given in keV. It is important to note that these expressions were derived in the limit of one dimension (1D). In three dimensions (3D), the effect of asymmetries [46] and RT-induced mix of hot and cold fuel must also be considered [47, 48], as they can impact the proper formation of the hot spot and reduce T_i, burn volume and Y_n due to reduced pressure. To account for the 3D effects, Betti $et\ al$ showed numerically that equations (2.4), (2.5) should be reformulated as

$$\chi = \rho R^{0.8} \left(\frac{T_i}{4.3} \right)^{1.6} \left(\frac{Y_n}{Y_{1D}} \right)^{0.4}, \qquad (2.6)$$

and

$$P\tau > 8 \cdot (\rho R \cdot T_i)^{0.8} \left(\frac{Y_n}{Y_{1D}} \right)^{0.4}, \qquad (2.7)$$

where Y_n and Y_{1D} are the measured and 1D-simulated neutron yields, respectively. The assumption made here is that 3D effects fully explain the discrepancy between simulations and experiments. It should also be noted that from equations (2.4)–(2.7) it is clear that the DT fuel must to be spherically assembled to maximize ρR and T_i, while at the same time keep the fuel assembled for long enough time for a substantial number of fusion reactions to take place. To evaluate the performance of an ICF implosion, during the nuclear phase, it is also clear that Y_n, T_i, ρR, burn duration, burn profiles, and their 3D asymmetries must be diagnosed.
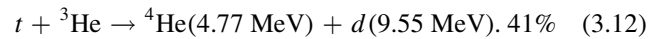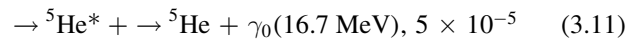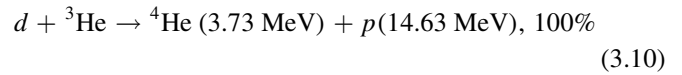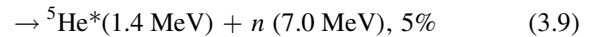
As discussed in the next sections, this can be done through spectral, spatial and temporal measurements of the nuclear fusion products emitted from an ICF implosion.

3. Nuclear fusion products from an ICF implosion

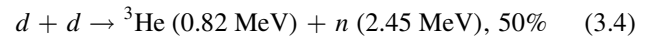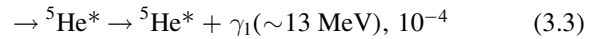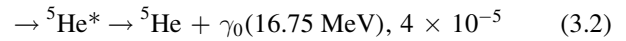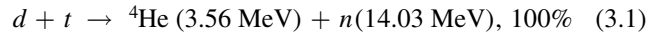In an ICF implosion with DT fuel, a certain set of reactions take place. In surrogate implosions with either pure D$_2$ fuel or D^{3}He fuel, another set of reactions take place. In this review paper, we discuss the primary, secondary and tertiary reactions, in these fuels, which are used routinely to diagnose an ICF implosion[5]. A detailed discussion about the information carried by the fusion products is made in section 4.

3.1. Primary

The primary reactions and reaction products that are used routinely for diagnostics purposes are:

$$d + t \rightarrow {}^4\mathrm{He}\,(3.56\ \mathrm{MeV}) + n(14.03\ \mathrm{MeV}),\ 100\% \quad (3.1)$$

$$\rightarrow {}^5\mathrm{He}^* \rightarrow {}^5\mathrm{He} + \gamma_0(16.75\ \mathrm{MeV}),\ 4 \times 10^{-5} \quad (3.2)$$

$$\rightarrow {}^5\mathrm{He}^* \rightarrow {}^5\mathrm{He}^* + \gamma_1(\sim 13\ \mathrm{MeV}),\ 10^{-4} \quad (3.3)$$

$$d + d \rightarrow {}^3\mathrm{He}\,(0.82\ \mathrm{MeV}) + n\,(2.45\ \mathrm{MeV}),\ 50\% \quad (3.4)$$

$$\rightarrow {}^3\mathrm{H}\,(1.01\ \mathrm{MeV}) + p\,(3.02\ \mathrm{MeV}),\ 50\% \quad (3.5)$$

$$\rightarrow {}^4\mathrm{He}^* \rightarrow {}^4\mathrm{He} + \gamma_0(23.8\ \mathrm{MeV}),\ 10^{-7} \quad (3.6)$$

$$t + t \rightarrow {}^4\mathrm{He}\,(<3.8\ \mathrm{MeV}) + 2n\,(<9.4\ \mathrm{MeV}),\ 85\% \quad (3.7)$$

$$\rightarrow {}^5\mathrm{He}\,(1.7\ \mathrm{MeV}) + n\,(8.7\ \mathrm{MeV}),\ 10\% \quad (3.8)$$

$$\rightarrow {}^5\mathrm{He}^*(1.4\ \mathrm{MeV}) + n\,(7.0\ \mathrm{MeV}),\ 5\% \quad (3.9)$$

$$d + {}^3\mathrm{He} \rightarrow {}^4\mathrm{He}\,(3.73\ \mathrm{MeV}) + p(14.63\ \mathrm{MeV}),\ 100\% \quad (3.10)$$

$$\rightarrow {}^5\mathrm{He}^* + \rightarrow {}^5\mathrm{He} + \gamma_0(16.7\ \mathrm{MeV}),\ 5 \times 10^{-5} \quad (3.11)$$

$$t + {}^3\mathrm{He} \rightarrow {}^4\mathrm{He}(4.77\ \mathrm{MeV}) + d(9.55\ \mathrm{MeV}).\ 41\% \quad (3.12)$$
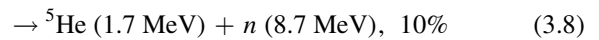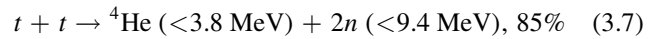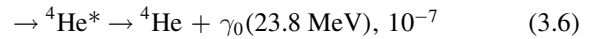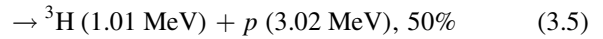
Here, the kinetic energies of the fusion products for a zero-temperature plasma are shown in the parentheses. The strength of the different reaction branches is also indicated. Among these reactions, the $d + t$ (dt) reaction is the most viable one from an energy gain point of view due to its highest cross-section (about two orders of magnitude higher than the cross sections for the other reactions) at temperatures that can be readily achieved in an ICF implosion. In the dt case, 80% of the kinetic energy is carried by the neutron, while the remaining kinetic energy is carried by the alpha particle.
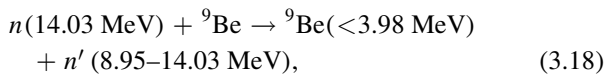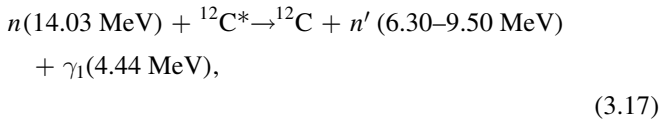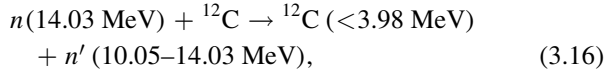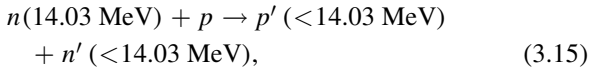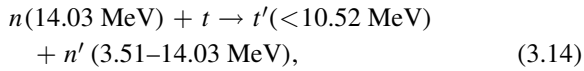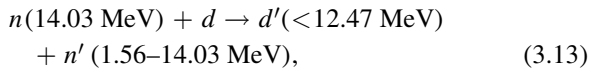
3.2. Secondary

In an ICF implosion, a large fraction of the primary-reaction products interact (or react) with the ions in the fuel and ablator (or liner). In the case of the DT fuel, the dt neutrons

---

[5] In some experiments, a dopant of a particular element is introduced into the fuel or ablator, targeting a specific reaction that can be measured by a certain set of nuclear diagnostics probing certain physics. These particular cases are discussed in some of the diagnostics sections.

interact (or react) with the ions in the fuel and ablator (or liner) as described by

$$n(14.03 \text{ MeV}) + d \rightarrow d'(<12.47 \text{ MeV})$$
$$+ n'(1.56–14.03 \text{ MeV}), \quad (3.13)$$

$$n(14.03 \text{ MeV}) + t \rightarrow t'(<10.52 \text{ MeV})$$
$$+ n'(3.51–14.03 \text{ MeV}), \quad (3.14)$$

$$n(14.03 \text{ MeV}) + p \rightarrow p'(<14.03 \text{ MeV})$$
$$+ n'(<14.03 \text{ MeV}), \quad (3.15)$$

$$n(14.03 \text{ MeV}) + {}^{12}C \rightarrow {}^{12}C(<3.98 \text{ MeV})$$
$$+ n'(10.05–14.03 \text{ MeV}), \quad (3.16)$$

$$n(14.03 \text{ MeV}) + {}^{12}C^* \rightarrow {}^{12}C + n'(6.30–9.50 \text{ MeV})$$
$$+ \gamma_1(4.44 \text{ MeV}), \quad (3.17)$$

$$n(14.03 \text{ MeV}) + {}^{9}Be \rightarrow {}^{9}Be(<3.98 \text{ MeV})$$
$$+ n'(8.95–14.03 \text{ MeV}), \quad (3.18)$$

where the energy ranges of the reaction products are given in the parentheses. Here, n' represents the down-scattered neutron. The up-scattered ion is often called 'knock-on' ion. Additional processes such (n, 2n) and (n, p) reactions take place in the fuel and ablator, but these processes are not generally used for diagnostic purposes. At energies above $\sim$10 MeV, but below the primary-neutron peak, the neutron spectrum is dictated by elastic-scattering processes [50]. At lower energies, neutrons originating from break-up reactions and multiple scattering also play a role. If the reaction goes through an excited target nucleus, a gamma ray is generated, as illustrated by reaction (3.17), which shows neutron inelastic scattering on the first excited state of ^{12}C. Inelastic neutron scattering on the second and third excited state of ^{12}C generates neutrons in the energy range 3.7–6.2 MeV and 2.1–4.1 MeV, respectively.
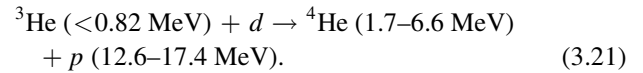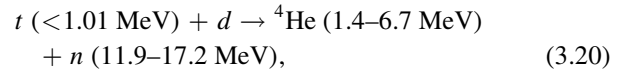
The dt alphas, born with an average energy of 3.56 MeV, traverse the plasma and mainly interact with the electrons and lose energy as a result. During this process they may also elastically scatter off the fuel ions, either through Coulomb- or nuclear-elastic scattering, and generate populations of supra-thermal deuterons and tritons with energies up to a few MeV. These supra-thermal ions may in turn react with the thermal ions, generating a broad secondary-neutron spectrum from $\sim$10 to $\sim$20 MeV, with a yield from 10^{-6} to 10^{-3} relative to the primary yield, depending on the electron temperature. Even though this alpha knock-on component is a weak feature in the ICF neutron spectrum, this component typically dominates at energies in the range 16–20 MeV, where it can be probed for an assessment of the alpha heating of the plasma ions. Further discussions about the generation and use of the alpha knock-on component in the neutron spectrum is not made in this review paper, but additional information can be found in the papers by Fisher *et al* [51], Ballabio *et al* [52], and Källne *et al* [53] for tokamak plasmas.

In the case of pure D$_2$ fuel, there are several secondary-reaction processes that take place in an implosion, but only a few are relevant to ICF as discussed in section 4. One process involves primary *dd* neutrons elastically scattering off the Be liner (in a MagLIF experiment), as described by the reaction
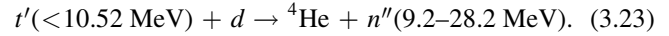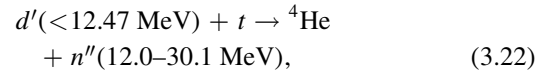
$$n(2.45 \text{ MeV}) + {}^{9}Be \rightarrow {}^{9}Be(<0.88 \text{ MeV})$$
$$+ n'(1.57–2.45 \text{ MeV}). \quad (3.19)$$
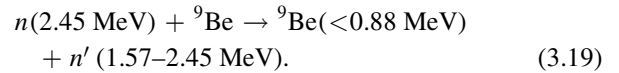
Other secondary-reaction processes that are used to diagnose an implosion are initiated by the 1.01 MeV tritons and 0.82 MeV ^{3}He-ions generated by the *dd* reactions (reactions (3.4) and (3.5)). A small fraction of these nuclear-fusion products react with the thermal deuterons as they traverse the plasma, as described by the following reactions

$$t (<1.01 \text{ MeV}) + d \rightarrow {}^{4}He (1.4–6.7 \text{ MeV})$$
$$+ n (11.9–17.2 \text{ MeV}), \quad (3.20)$$

$${}^{3}He (<0.82 \text{ MeV}) + d \rightarrow {}^{4}He (1.7–6.6 \text{ MeV})$$
$$+ p (12.6–17.4 \text{ MeV}). \quad (3.21)$$

Here, the spectra of the secondary fusion products are broad due to the high center-of-mass energy and isotropic motion of the reactants.

3.3. Tertiary

A small fraction of the up-scattered deuterons (d') or tritons (t') produced in reactions (3.13) and (3.14) undergo reactions with thermal ions while traversing the fuel. These reactions produce tertiary neutrons (n'') as described by

$$d'(<12.47 \text{ MeV}) + t \rightarrow {}^{4}He$$
$$+ n''(12.0–30.1 \text{ MeV}), \quad (3.22)$$

$$t'(<10.52 \text{ MeV}) + d \rightarrow {}^{4}He + n''(9.2–28.2 \text{ MeV}). \quad (3.23)$$

The probability for generating tertiary neutrons above 20 MeV depends on ρR and ρR^2 for high-ρR and low-ρR implosions, respectively [54]. However, as the generation of tertiary neutrons is a tree-step process, the probability for generating these is extremely small and results in a tertiary neutron yield of order 10^{-6} relative to the primary neutron yield, which makes it difficult to probe. Since higher yields, than achieved to date, are required to probe this component, it will not be discussed further in this review paper. Additional reading about tertiaries produced in DT^{3}He fuel can be found in the paper by Petrasso *et al* [54].

Figure 1 illustrates ICF neutron spectra simulated by the hydrodynamic code LASNEX for three DT implosions at the NIF. As shown in the figure, the width and magnitude of the primary-neutron spectrum for the ignited case is significantly larger than the primary-neutron spectra produced in the failed implosions, indicating a significantly higher T_i and Y_n in the ignited case, respectively. When comparing the ρR values for the failed implosions, it is also clear that a higher ρR is achieved in failure 1 than in failure 2.

4. Information carried by the fusion products

As fusion yields have increased about ten orders of magnitude since the beginning of the experimental ICF program, the quality of the nuclear-fusion-product measurements has
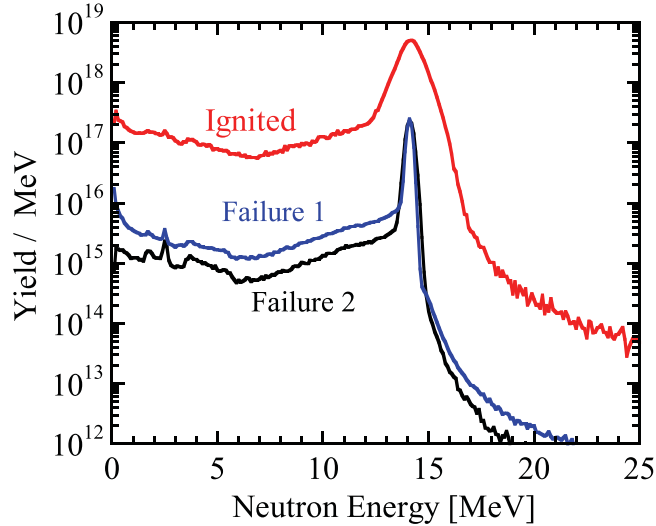
Figure 1. ICF neutron spectra simulated by the hydrodynamic code LASNEX for three *dt* implosions at the NIF. The details of the spectra are dictated by primary, secondary and tertiary neutrons, as discussed in the text. The red spectrum is for an ignited implosion, producing a neutron-burn averaged T_i of ~40 keV and Y_n of 6×10^{18}. The blue and black spectra are produced by implosions that failed to ignite, generating a T_i of ~5 keV and significantly lower Y_n. The blue spectrum is originating from an implosion with a ρR of 2.0 g cm^{-2} that failed due to electron-conduction issues, while the black spectrum is originating from an implosion with a ρR of 1.0 g cm^{-2} that failed due to entropy issues. As illustrated by these two spectra (which have been normalized to each other using Y_n), the Failure-1 implosion produces a significantly higher down-scattered-neutron component than the Failure-2 implosion. Reproduced courtesy of IAEA. Figure from [50]. Copyright 2013 IAEA.
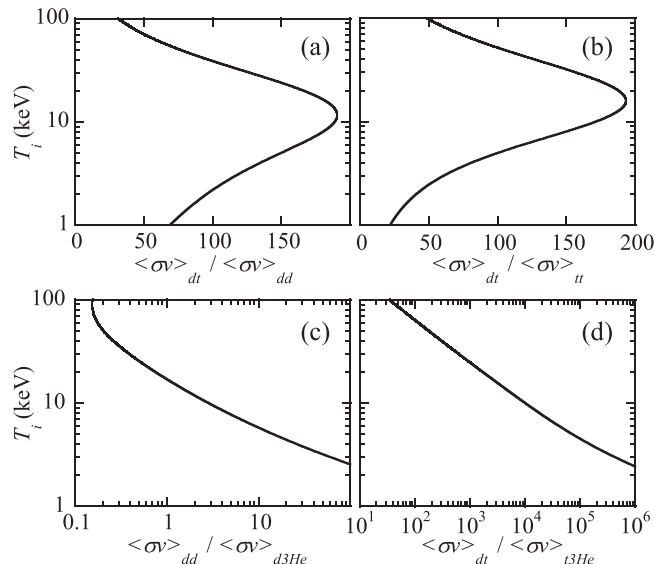
Figure 2. T_i-dependence on the reactivity ratio (a) *dt/dd*, (b) *dt/tt*, (c) *dd/d³He*, and (d) *dt/t³He*.

improved significantly, facilitating an increased level of understanding about the physics governing the nuclear phase of an ICF implosion. As discussed in this section, the field of ICF has now entered an era where the fusion yields are high enough to provide high-fidelity nuclear data with spatial, temporal and spectral information, which have proven
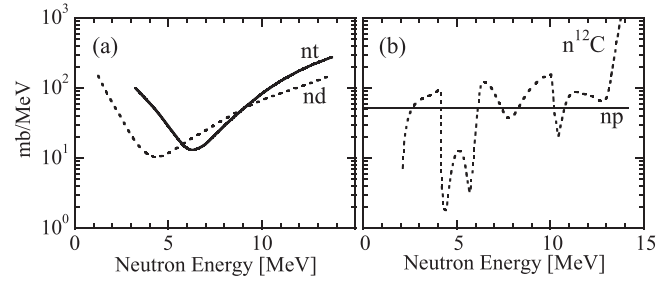
Figure 3. (a) The differential cross sections for the *nd* and *nt* elastic scattering at a neutron energy of 14 MeV. (b) The differential cross sections for the *np* elastic scattering, and n^{12}C elastic and inelastic scattering. The elastic n^{12}C scattering generates neutrons in the range 10.05–14.03 MeV, and inelastic n^{12}C scattering on the first, second and third excited state of ^{12}C generates neutrons in the energy range 6.3–9.5 MeV, 3.7–6.2 MeV and 2.1–4.1 MeV, respectively. Reproduced courtesy of IAEA. Figure adapted from [50]. Copyright 2013 IAEA.

indispensable to understanding the performance of an ICF implosion. In the case of a high-density ICF implosion, only neutral reaction products such as neutrons (and gamma-rays at much lower yields) readily escape. Measurements of the directional emission of primary, down-scattered and secondary neutrons are therefore arguably the most important probe of the conditions in the hot spot and surrounding high-density shell of an ICF implosion, as these types of neutrons carry information about absolute nuclear yield, ion temperature, nuclear burn history, fuel and ablator ρR, and morphology of the implosion. In addition, primary and secondary charged particles emitted from a lower- to medium-ρR implosion carry similar information, as well as information about magnetic and electric fields. This is discussed in detail in this section.

4.1. Nuclear yield

Nuclear yield (Y_{ij}) is an integral quantity that provides important information about the overall performance of an ICF implosion. It depends on several factors and is normally expressed as

$$Y_{ij} = \iint \frac{n_i n_j}{1 + \delta_{ij}} \langle \sigma v_{rel} \rangle_{ij} dV d\tau, \qquad (4.1)$$

where δ_{ij} is the Kronecker delta that is equal to 1(0) for reactant i equal(unequal) to reactant j, n_i and n_j are the ion-number density of the reactants i and j, respectively, $\langle \sigma v_{rel} \rangle_{ij}$ is the fusion reactivity, and $n_i n_i \langle \sigma v_{rel} \rangle_{ij}$ is the reaction rate that is integrated over the burn volume (V) and burn duration (τ). The fusion reactivity is expressed as

$$\langle \sigma v_{rel} \rangle_{ij} = \iint f_i(v_i) f_j(v_j) v_{rel} \sigma(v_{rel}) dv_i dv_j, \qquad (4.2)$$

where $f_i(v_i)$ and $f_j(v_j)$ are normalized velocity distributions of the two reactants, v_{rel} is the relative velocity between the two reactants, and $\sigma(v_{rel})$ is the fusion cross section. In calculations of $\langle \sigma v_{rel} \rangle_{ij}$ and Y_{ij}, it is routinely assumed that the velocity distributions are Maxwellian. In addition, equation (4.1) implies that information about T_i, burn volume, and burn duration and their spatial and temporal variations is critical for evaluating the implosion performance.
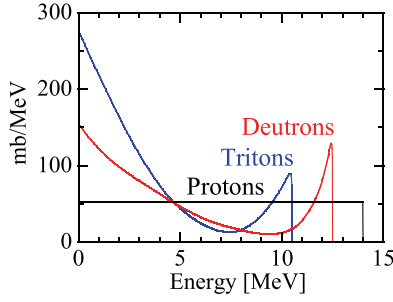
Figure 4. Birth spectra of up-scattered deuterons, tritons and protons, generated by 14 MeV neutrons elastically scattering of these ions. The shape of the spectra are dictated by the differential cross-sections for elastic scattering. The effective cross sections for the high-energy deuteron and triton peaks are 104 mb and 142 mb, respectively.

4.2. Ion temperature

As discussed in section 2, T_i is a central performance metric for an ICF implosion. The information about T_i is encoded in the nuclear-yield ratio between two primary reactions and Doppler-broadened primary fusion-product spectrum. This complementary information, when used concurrently, is invaluable to the efforts in understanding the nature of the reacting ions.

In the case of a thermal plasma, the local velocity distribution of the reacting ions and $\langle \sigma v_{rel} \rangle_{ij}$ are uniquely described by a local ion temperature T_i. This means that information about T_i is encoded in the yield ratio between two nuclear reactions with different reactivity sensitivity to T_i changes. For an equimolar plasma ($n_i = n_j$), T_i can be expressed in terms of reactivities as

$$T_i \propto \frac{Y_{ii}}{Y_{ij}} = \frac{1}{2} \frac{\langle \sigma v_{rel} \rangle_{ii}}{\langle \sigma v_{rel} \rangle_{ij}}. \qquad (4.3)$$

This expression is derived under the assumption that the burn volume V and burn duration τ are the same for the two nuclear reactions. As the differences in burn duration and burn profile of the reacting constituents result in only minor corrections to the inferred T_i (burn durations are similar and the different reactions are dominated by the high-T_i region near the center), the uncertainty associated with yield-ratio-inferred T_i is typically smaller than the uncertainties in the quantities common to both reactions such as burn volume V and burn duration τ. This has been discussed by Casey *et al* for the dt/dd and dt/tt ratios [55]. Figure 2 illustrates the Ti-dependence on the reactivity ratio for several light-ion reactions.

As discussed by Brysk [56], Ballabio *et al* [57], Appelbe *et al* [58], and Munro [59], T_i is also encoded in the width (ΔE_D) of the Doppler broadened primary fusion-product spectrum. For a thermal plasma, the shape of the spectrum is to the first order represented by a Gaussian, and T_i is expressed in terms of ΔE_D as

$$T_i \approx 9 \times 10^{-5} \frac{m_3 + m_4}{m_4 \langle E_4 \rangle} \Delta E_D^2, \text{ (keV)}, \qquad (4.4)$$

where m_3 and m_4 are the masses of fusion products 3 and 4, respectively, and $\langle E_4 \rangle$ is the mean kinetic energy of the fusion product 4 (given in MeV), and the width ΔE_D is given in

keV. Here, ΔE_D is dictated by the center-of-mass-velocity (V_{CM}) distribution of the reactants along the spectrometer line of sight (LOS). E_4 is relativistically expressed as [57, 60]

$$E_4 = (\xi - m_4) + \left(\frac{\xi}{(m_1 + m_2)} + \frac{m_3^2 - m_4^2}{(m_1 + m_2)^2} \right) K$$
$$+ \frac{1}{2} \xi V_{CM}^2 + V_{CM} \cos \theta \sqrt{\xi^2 - m_4^2}, \qquad (4.5)$$

where m_1 and m_2 are the masses of reactants 1 and 2, respectively, K is the total kinetic energy of the reactants in the CM system, θ is the angle between the V_{CM} direction and the fusion-product direction in the CM system, and $\xi = [(m_1 - m_2)^2 + m_4^2 - m_3^2]/[2(m_1 + m_2)]$. The first term in equation (4.5) represents the energy of the fusion product 4 for a zero-temperature plasma (this term is dictated by the Q value of the reaction as shown by equations (3.1)–(3.12)), the second term represents the energy upshift of fusion product 4 due to a finite-temperature plasma, and the third and fourth terms represent the CM energy. For a thermal plasma in which V_{CM} and emission direction of the fusion products are isotropic, the last term in equation (4.5) vanishes, i.e.

$$\langle E_4 \rangle = (\xi - m_4) + \left(\frac{\xi}{(m_1 + m_2)} + \frac{m_3^2 - m_4^2}{(m_1 + m_2)^2} \right) \langle K \rangle$$
$$+ \frac{1}{2} \xi \langle V_{CM}^2 \rangle. \qquad (4.6)$$

As discussed in the next section, macroscopic flows modify the V_{CM} distribution and affect the mean energy (1st moment), width (2nd moment) and shape (higher-order moments) of the primary fusion-product spectrum.

4.3. Macroscopic plasma flows

The field of ICF has recently come to the realization that the width of the primary fusion-product spectrum is an inadequate representation of T_i [61]. The main reason for this is that macroscopic flows in the fuel are often comparable to the thermal velocities of the reactants, indicating that the width of the primary fusion spectrum is in fact a representation of both thermal and macroscopic-flow variances. When considering both these processes, Murphy showed that the width (ΔE) of the primary fusion-product spectrum can be expressed as [62]

$$\Delta E^2 = \Delta E_D^2 + \Delta E_K^2 = 32 \ln 2 m_4 \langle E_4 \rangle \left[\frac{k_B T_i}{m_3 + m_4} + \sigma_{KE}^2 \right]. \qquad (4.7)$$

Here, σ_{KE}^2 is the macroscopic-flow variance and is given by $2E_{KE}/3M$, where E_{KE} is the kinetic energy of the fuel and M is the total mass of the fuel. Given that $k_B T_i$ can be expressed as $\langle A \rangle E_{TH}/2MN_A$, where $\langle A \rangle$ is the average mass number of the reactants, E_{TH} is the fuel thermal energy, and N_A is the Avogadro's constant, equation (4.7) can be rewritten as

$$\Delta E^2 = \frac{32 \ln 2 m_4 \langle E_4 \rangle}{M} \left[\frac{1}{3} \frac{\langle A \rangle}{(m_3 + m_4)N_A} E_{TH} + \frac{2}{3} E_{KE} \right]. \qquad (4.8)$$

For an equimolar DT plasma where $\langle A \rangle$ is equal to 2.5, equation (4.8) points to the fact that the relative impact of E_{KE} on ΔE is four times more effective than E_{TH}, and that E_{KE} affects the width of the *dt*-neutron spectrum 1.25 times more than the *dd*-neutron spectrum.[6] From an optimal implosion performance point of view, E_{TH} and E_{KE} must be maximized and minimized, respectively.

As discussed by Gatu Johnson *et al* [60], Munro *et al* [61], and Murphy *et al* [62], macroscopic flows not only affect ΔE, but also $\langle E_4 \rangle$. While a finite T_i always increases $\langle E_4 \rangle$, a macroscopic plasma flow (V_{flow}) either 'red shifts' or 'blue shifts' the primary fusion-product spectrum, depending on the effective velocity vector relative to the spectrometer LOS. Under the assumption that $V_{CM} \approx V_{flow}$ and $K \ll Q$, which is generally the case for an ICF implosion, the mean energy shift (δE_{flow}) due to macroscopic plasma flows is given by

$$\delta E_{flow} = E_4 - E_0 = \frac{1}{2}\xi V_{flow}^2 + V_{flow}\cos\theta\sqrt{\xi^2 - m_4^2},$$
$$(4.9)$$

where $E_0 = \xi - m_4$. For the *dt* reaction, Gatu Johnson *et al* [60] showed that equation (4.9) can be approximated by

$$\delta E_{flow} = 5.3 \times 10^{-6}V_{flow}^2 + 0.54 \cdot V_{flow}\cos\theta. \qquad (4.10)$$

Here, V_{flow} is given in km s^{-1} and δE_{flow} is given in keV. For a typical ICF implosion, V_{flow} is small, which means that the first term can be neglected. For bulk velocities approaching 1000 km s^{-1}, the two terms start to be comparable.

4.4. Nuclear burn profile and volume

Information about the fuel assembly of an ICF implosion is, in part, encoded in the nuclear burn profile and overall burn volume, as indicated by equation (4.1). This type of data, combined with other data, carries information about fuel-shell mix, implosion asymmetries, radiation and heat transport, and hot-spot pressure P.

4.5. Nuclear-burn history

The nuclear burn history provides critical information about shock convergence, shock reverberations, dynamics of the high-density fuel-shell during the deceleration phase, impact of alpha heating, and a multitude of failure mechanisms. Having this information is critical for assessing the energy-confinement time τ_E and performance of an ICF implosion, as shown by equations (2.1)–(2.7) and (4.1).

4.6. Areal density of fuel and ablator

Information about the fuel assembly of an ICF implosion is encoded in the fuel and ablator ρR. Understanding spatial ρR asymmetries (discussed in section 4.8) are also central in our efforts in understanding the implosion performance.

As ρR represents the number of target ions in the fuel and ablator that are 'in the way' of a primary, secondary or tertiary

fusion product (per unit area normal to its direction of motion), ρR is a measure of the probability for interactions between a fusion product and target ions in the fuel and ablator. Given that nuclear cross sections govern neutron interactions and that Coulomb cross sections govern charged-particle interactions, a higher ρR value enhances the yield of down-scattered neutrons and secondary fusion products, whereas it increases the average energy downshift of charged fusion products emitted from an ICF implosion. More specifically, information about ρR is carried by

1. Yield ratio between down-scattered neutrons and primary neutrons.
2. Yield ratio between up-scattered ions and primary neutrons.
3. Yield ratio between 4.44 MeV gamma-rays from ^{12}C(n, $n\gamma$) reactions and primary neutrons.
4. Relative yield between un-scattered primary neutrons emitted in different directions.
5. Energy loss of charged fusion products.
6. Yield ratio between secondary *dt* neutrons (or d^3He protons) and primary *dd* neutrons.

1. Yield ratio between down-scattered neutrons and primary neutrons

A fraction of the produced primary neutrons elastically scatter of the fuel and ablator ions, generating an energy continuum of down-scattered neutrons as described by expressions (3.13)–(3.19). The shape and magnitude of the down-scattered neutron spectrum is, to the first order, dictated by the differential cross section for the elastic-scattering process, and in some cases by both elastic and inelastic scattering processes, which are generally well known [60–65] (see figure 3).

The ratio between down-scattered-neutron yield ($Y_{n'}$), in a certain energy range, and primary-neutron yield (Y_n) is typically called the down-scattered ratio (dsr) and is an important performance metric for an ICF implosion. To illustrate the dependence between the total ρR and dsr, in the simplest possible fashion, a 1D hot-spot model of uniform *dt* fuel surrounded by CH ablator is used, where all primary *dt* neutrons are produced in the center of the implosion. In this case, the total ρR is to the first order related to the dsr by[7]

$$\rho R = \rho R_{dt} + \rho R_{CH} = \int_{E_1}^{E_2}\left(\frac{(2\alpha + 3)m_p}{\alpha\sigma_{nd} + \sigma_{nt}}\mathrm{dsr}_{dt}(E)\right.$$
$$\left. + \frac{(\beta + 12)m_p}{\beta\sigma_{np} + \sigma_{n^{12}\mathrm{C}}}\mathrm{dsr}_{CH}(E)\right)dE.$$
$$(4.11)$$

Here, m_p is the proton mass, and σ_{nd}, σ_{nt}, σ_{np}, and $\sigma_{n^{12}\mathrm{C}}$ are the effective *nd*, *nt*, *np* and *n*^{12}C cross sections for generating down-scattered neutrons in a certain energy interval $E_1 - E_2$, respectively. For an equimolar *dt* fuel and CH ablator, $\alpha = n_d/n_t = 1$ and $\beta = n_p/n_c = 1$. As

---

[6] The coefficient in front of the thermal term in equation (4.8) is 1/6 for the *dt*-neutron spectrum and 5/24 for the *dd*-neutron spectrum.

[7] The first term in equation (4.11) is derived under the assumption that $\rho R = \int \rho R dr = (\alpha m_d + m_t)\int n_t(r)dr$ and $Y_n = (\alpha\sigma_{nd} + \sigma_{nt})Y_n \int n_t(r)dr$.

$[\sigma_{nd} + \sigma_{nt}]$(10–12 MeV) and $[\sigma_{np} + \sigma_{n^{12}C}]$(10–12 MeV)[8] are 400 mb and 250 mb, respectively, equation (4.11) is reduced to[9]

$$\rho R = \rho R_{dt} + \rho R_{CH} \approx 21 \mathrm{dsr}_{dt} + 87 \mathrm{dsr}_{CH}. (\mathrm{g\ cm}^{-2}) \quad (4.12)$$

This expression indicates that the down-scattered neutrons in the energy range 10–12 MeV primarily probe ρR_{dt} and are relatively insensitive to the ρR_{CH} due to different interaction probabilities per unit ρR. According to radiation hydrodynamic simulations, ρR_{CH} is also typically 10%–20% of the ρR_{dt} in an implosion at the NIF [50], indicating that thee second term in equation (4.12) can often be omitted. However, as the total ρR dictates the confinement time τ of the hot spot, information about ρR_{CH} is also important. If a different ablator is used, the coefficient in front of the second term is different. In addition, as ρR increases, equations (4.11), (4.12) gradually become invalid because multiple scattering becomes increasingly important[10].

Although the dsr value provides information about ρR_{dt}, it does not provide sufficient information for building a complete picture of the assembled fuel. Additional information about the birth location of the primary neutrons and scattering locations generating the down-scattered neutrons is necessary. This information can in principle be accessed because the scattering angle between the incoming primary and outgoing down-scattered neutron uniquely defines the energy of the down-scattered neutron as described by $E_{n'} = E_n [1 - 4A\mathrm{Cos}^2\theta/(A + 1)^2]$ [66], where E_n is the energy of the primary neutron, A is the mass number of target ion, and θ is the scattering angle between the incoming primary neutron and outgoing recoil ion. This expression illustrates that a more accurate ρR value can be assigned to the dsr value, if the effect of the primary-neutron-source and high-density profile, both 3D in nature, are known (see discussion in section 4.8 and [50]). In this case, the fuel density is not integrated radially, but rather over the density-weighted primary-neutron path-length distribution $\langle L \rangle$ through the fuel. This applies to all yield-ratio methods. In addition, a more complete picture of the assembled fuel can be obtained with dsr values assigned to different portions of the implosion.

2. Yield ratio between up-scattered ions and primary neutrons

As illustrated by the scattering processes (3.13)–(3.15), up-scattered ions (deuterons, tritons or protons) are

generated, and the yield ratio between one of these ions and primary neutrons is governed by the same physics dictating the dsr value. In the case of up-scattered deuterons, ρR_{dt} can in its simplest form be expressed in terms of (Y_{nd}/Y_n) as

$$\rho R_{dt} = \frac{(2\alpha + 3)m_p}{\alpha\sigma_{nd}} \frac{Y_{nd}}{Y_n}, \quad (4.13)$$

where σ_{nd} is the effective cross section for generating up-scattered deuterons in a certain energy interval. Similar expressions exist for up-scattered tritons and protons from the fuel and CH ablator, respectively. For low-ρR_{dt} cases (<50 mg cm^{-2}), the high-energy peak of the up-scattered deuteron and triton spectra are effectively used to infer ρR_{dt}. At higher ρR_{dt} values, most of these ions are ranged out, significantly distorting the spectrum, which prevents the use of the high-energy peak [67]. Up-scattered protons from the CH ablator provide information about the ρR_{CH} up to ~ 250 mg cm^{-2}. Since the differential cross section and spectrum of up-scattered protons are practically flat, the yield per unit energy (Y_{np}) can be used for a ρR_{CH} determination as described by

$$\rho R_{CH} = \frac{(\beta + 12)m_p}{\beta\sigma_{np}} \frac{Y_{np}}{Y_n}, \quad (4.14)$$

where σ_{np} is the effective cross section for generating up-scattered protons in a certain energy range.

3. Yield ratio between 4.44 MeV gamma-rays and primary neutrons

A small fraction of the produced primary neutrons inelastically scatter of the ^{12}C nuclei in a CH or HDC ablator, generating 4.44 MeV gamma-rays (equation (3.17)) that are emitted quasi-isotropically. Along the same discussion as for down-scattered neutrons and up-scattered ions, the yield ratio between 4.44 MeV gamma-rays and primary neutrons carries information about ρR_{CH} as described by

$$\rho R_{CH} = \frac{(\beta + 12)m_p}{\sigma_{n^{12}C*}} \frac{Y_\gamma}{Y_n}. \quad (4.15)$$

Here, $\sigma_{n^{12}C*}$ is the inelastic cross section for generating 4.44 MeV gamma-rays and Y_γ is the yield of 4.44 MeV gamma-rays from the first, excited state of ^{12}C. In the case of an HDC ablator, $\beta = 0$. Given that the gamma-rays are emitted quasi-isotropically, this expression represents a spatially-averaged ablator ρR.

4. Relative yield of un-scattered primary neutrons emitted in different directions

As the yield of down-scattered neutrons depends on ρR, the yield of un-scattered primary neutrons (Y_{unsc}), above certain energy, also carries information about the ρR_{dt} of the region traversed by the primary neutrons (the effect of the ρR_{CH} is small and can be

---

[8] The down-scattered-neutron spectrum in the 10–12 MeV range is dictated by the elastic-scattering process.
[9] The coefficient in front of the second term is incorrect in [50].
[10] For an equimolar DT implosion, with no ablator remaining, the single-down-scatter-neutron yield $Y_{n'}$ scales as $(\sigma_{nd}/5m_p)\ \rho R Y_n$, while the double-down-scatter-neutron yield $Y_{n''}$ at ~ 11 MeV scales as $(\sigma_{dt}^2/20m_p)\ \rho R_{dt}^2\ Y_n$. This means that the double-down-scatter process removes $\sim 10\%$ and $\sim 20\%$ of the single-down-scattered neutrons in the energy range of 10–12 MeV for a ρR_{dt} of 1 and 2 g cm^{-2}. Here, we have neglected that the source distributions of n and n' are different.

neglected in this discussion). This can be shown by first expressing Y_{unsc} in terms of the yield difference between produced primary neutrons and down-scattered neutrons

$$Y_{unsc} = Y_n - Y_{n'} = \left(1 - \frac{\alpha\sigma_{nd} + \sigma_{nt}}{(2\alpha + 3)m_p}\rho R_{dt}\right)Y_n, \qquad (4.16)$$

where σ_{nd} and σ_{nt} are the effective nd and nt elastic-scattering cross sections, respectively, for generating down-scattered neutrons below a certain energy. For an equimolar dt fuel, $\alpha = n_d/n_t = 1$, and equation (4.16) can be reformulated in terms of Y_{unsc}/Y_n

$$\rho R_{dt} = \frac{5m_p}{\sigma_{nd} + \sigma_{nt}}\left(1 - \frac{Y_{unsc}}{Y_n}\right). \qquad (4.17)$$

Looking at this quantity in several emission directions allows for the generation of an un-scattered neutron-yield map or a ρR_{dt} map. As it is challenging to directly quantify Y_n in high-ρR implosions, a spatial average of the un-scattered yield $\langle Y_{unsc}\rangle$ is more practical to use in equation (4.17). Replacing Y_n with $\langle Y_{unsc}\rangle$ makes the diagnosed ρR_{dt} a relative quantity.

5. Energy loss of charged fusion products

While yields of down-scattered neutrons or up-scattered ions, relative to the primary yield, carry information about ρR, energy loss of primary and secondary charged fusion products carry information about ρR as described by

$$\rho R = -\int \frac{d(\rho R)}{dE}dE = -\int \frac{1}{\frac{1}{\rho}\frac{dE}{dR}}dE, \qquad (4.18)$$

where dE/dR (or dE/dX in planar geometry) represents the rate of energy loss per unit distance traversed by the charged fusion product (called plasma stopping power). In general, the plasma stopping power is expressed in its most basic form as [68]

$$\frac{dE}{dX} = -\left(\frac{Z_i e}{v_i}\right)^2 \omega_p^2 G\left(\frac{v_i}{v_{th}}\right)\ln\Lambda_e, \qquad (4.19)$$

where $\omega_p = (4\pi n_e e^2/m_e)^{1/2}$ is the electron plasma frequency, n_e is the electron-number density, Z_i and v_i are the charge and velocity of the charged fusion product, respectively, v_{th} is the average velocity of the thermal electrons, $\ln\Lambda_e$ is the Coulomb logarithm that is a central parameter determining the interplay between long and short distance Coulomb interactions and thus the characteristics of the plasma stopping power. A few qualitative statements can be made. First, dE/dX is practically independent of T_e for high-energy primary or secondary fusion products with velocities v_i much higher than v_{th}, enabling ρR to be uniquely determined from the energy loss. Secondly, dE/dX depends strongly on both n_e and T_e when $v_i \sim v_{th}$. As described

extensively in the literature [69–73], the challenge is to determine the functional form of both $G(v_i/v_{th})$ and $\ln\Lambda_e$, which depend on the ion velocity and plasma conditions.

6. Yield ratio between secondary dt neutrons (or d^3He protons) and primary dd neutrons

Given that the velocities of the 1.01 MeV tritons and 0.82 MeV ^{3}He ions (produced by the dd reactions shown by equations (3.4)–(3.5)) are comparable to v_{th} in a typical ICF implosion, the energy loss depends strongly on ρR_d, T_e and plasma composition in an ICF implosion. This means that the yield ratios between secondary dt neutrons and dd neutrons (Y_{2n}/Y_n) and secondary d^3He protons and primary dd neutrons (Y_{2p}/Y_n) provide information about these parameters, which has been discussed extensively in the literature by Azechi et al [74–76], Cable et al [77], Séguin et al [78], and Kurebayashi et al [79]. Recently, Rinderknecht et al extended this work by demonstrating that the combined information from Y_{2n}/Y_n and Y_{2p}/Y_n provides information of at least two of above-mentioned plasma parameters [80]. The reason for this is that $\langle\sigma v_{rel}\rangle_{dt}$ increases and $\langle\sigma v_{rel}\rangle_{d^3He}$ decreases as the tritons and ^{3}He ions lose energy in the plasma, respectively. Given that the range of the tritons is also $\sim 10\times$ longer than that of ^{3}He ions, the combined information provided by the two yield ratios elucidates unique information about the hot spot for ρR_d values up to ~ 100 mg cm^{-2}. In addition, as the range of the 1.01 MeV tritons and 0.82 MeV ^{3}He ions depends strongly on the magnitude of the plasma stopping power, which approximately scales as $1/T_e$, an increased T_e reduces the stopping power, leading to increased ion ranges and increased probabilities for the secondary fusion reactions and higher Y_{2n}/Y_n and Y_{2p}/Y_n [74–80].

4.7. Electron temperature

For fuel ρR_d values above 100 mg cm^{-2}, both Y_{2n}/Y_n and Y_{2p}/Y_n generally saturate. In this regime, the yield ratio provides information about T_e of the region traversed by the tritons and ^{3}He ions assuming mix of high-Z material into the fuel is insignificant.

4.8. 3D asymmetries

The discussion in section 4 has so far been limited to 1D observables. Understanding the impact of 3D asymmetries on the implosion performance is also an essential prerequisite for obtaining a complete picture of the fuel assembly and hot-sport formation, because a non-spherical assembly of the main fuel reduces the efficiency of converting shell kinetic energy to hot-spot thermal energy at stagnation, leading to lower hot-spot pressure P and reduced confinement τ [81]. The 3D information can be accessed by diagnosing the implosion along different LOS. An example of 3D data is the spatial variation in the first and second moments in the primary fusion-product spectra. Large variations in these parameters are indicators of turbulent macroscopic flows in the hot spot, significantly affecting V_{CM} in the laboratory system. Other examples of 3D asymmetries are spatial variations in

the nuclear burn profile, dsr, and Y_{unsc}, which indicate a non-spherical hot spot and spatial ρR variations in the high-density fuel shell surrounding the hot spot.

4.9. Kinetic and multi-ion effects

When a converging shock rebounds at the center of an ICF implosion, it significantly raises T_i and n_i and initiates the nuclear burn. At this time, the mean-free path for ion-ion collisions is sufficiently long, relative to the plasma-scale length, that both the shock front itself and the resulting hot spot are governed by kinetic and multi-ion physics. Under these conditions, the combined information of absolute primary yields, primary-yield ratios, T_i and burn profiles carry information about kinetic and multi-ion effects in an ICF implosion. These phenomena can be explored by comparing average-ion hydrodynamic simulations to experiments [82–86]. In addition, nuclear burn profiles and burn histories carry information that goes beyond zero-dimensional, burn-integrated quantities, providing spatially and temporally resolved information about kinetic and multi-ion effects [87].

4.10. Magnetic and electric fields

Strong electric and magnetic fields often persist in plasmas relevant to ICF [88–92], and information about these fields is carried by the primary charged fusion products, generated in reactions (3.1)–(3.12). As discussed in some detail section 7.7, the direction of the incoming and outgoing quasi-mono-energetic charged fusion products, when produced by an external point source, carry information about the electric and magnetic fields in direct-drive, cone-in shell, and indirect-drive implosions.

5. Neutron diagnostics

To probe the wealth of information carried by neutrons, a wide range of neutron diagnostics have been implemented and extensively used at the different ICF facilities worldwide. Given that fusion yields have increased several orders of magnitude since the initiation of the experimental ICF program in the early 70s, the quality of the neutron measurements has improved significantly, facilitating an increased level of understanding about the physics governing the nuclear phase of an ICF implosion. At the biggest facilities, such as the NIF, fusion yields are now high enough for neutron measurements to provide spatial, temporal and spectral information, which have proven indispensable to understanding the performance of an ICF implosion. At the same time, the requirements on these measurements have also become more stringent. Fusion yields need to be measured over several orders of magnitude, up to $\sim 2 \times 10^{16}$ or $\sim 50\,\text{kJ}$ of fusion energy; ion temperatures need to be measured with high accuracy up to $\sim 10\,\text{keV}$; nuclear burn profiles and temporal histories need to be measured with spatial and temporal resolution of order $10\,\mu\text{m}$ and $10\,\text{ps}$, respectively.

Given that a particular diagnostic has its own set of limitations, different types of diagnostics are commonly used for measurements of a certain implosion parameter. In this section, we present the neutron diagnostics that are, or have been, routinely used to measure the parameters relevant to the nuclear phase of an ICF implosion.

5.1. Neutron activation diagnostics

The main objective with the Neutron Activation Diagnostic (NAD) is to measure the absolute yield of neutrons emitted in a certain direction from an ICF implosion[11]. Generally, a NAD, made of a suitable element, is positioned at a known distance from the implosion and is irradiated by the emitted neutrons. When neutrons, above a certain reaction threshold, interact with the chosen diagnostic material element, nuclear reactions occur that create a radioactive isotope of the element. After the neutron exposure, the NAD is removed and brought, either manually or automatically, to a counting station where the subsequent decay of the radioactive isotope is measured, from which the number of neutrons passing through the NAD can be quantified. The absolute yield of emitted neutrons, above a certain reaction threshold, is determined by

$$Y_{unsc} = \frac{4\pi d^2 A N_\gamma}{m_{NAD} f_{BR} f_a N_A \varepsilon_d \sigma_{eff} e^{-\lambda \Delta t_1}(1 - e^{-\lambda \Delta t_2})}. \quad (5.1)$$

Here, d is the detector distance to the implosion, A is the mass number of the isotope used for the detection, N_γ is the number of measured gamma-rays emitted by the decay, m_{NAD} is the mass of the NAD, f_{BR} is the branching ratio producing the gamma-rays of interest, f_a is the abundance of the isotope in the NAD, N_A is Avogadro's number, ε_d is the detection efficiency, σ_{eff} is the neutron-spectrum-weighted effective cross section, λ is the decay time constant of the radioactive isotope, Δt_1 is the time between the implosion time and start of the radioactive-decay measurement, and Δt_2 is the time duration for the radioactive-decay measurement. It should be noted that the effects of neutron scattering and absorption by nearby structures and the NAD itself are not considered by equation (5.1) [93]. In addition, for an accurate assessment of σ_{eff} and yield of the emitted neutrons, the data must be analyzed using the actual neutron spectrum from the implosion. Historically, the analysis has used a Gaussian primary-neutron spectrum and thus not considered the down-scattered-neutron component above the reaction threshold, which can have an impact on the analysis.

In the case of low neutron yields, a high-efficiency system is required. This means that a NAD with a large mass (tens of grams) must be used, which complicates the absolute calibration of the detector, as the fluence of the neutrons through the NAD changes and self-absorption of the gamma-rays emitted by the system may be significant. These issues are typically addressed by exposing the NAD to a known

---

[11] This should be distinguished from the absolute neutron yield Y_n produced in a high-ρR implosion, as the unscattered primary-neutron yield $\langle Y_{unsc} \rangle$ is significantly less than Y_n.
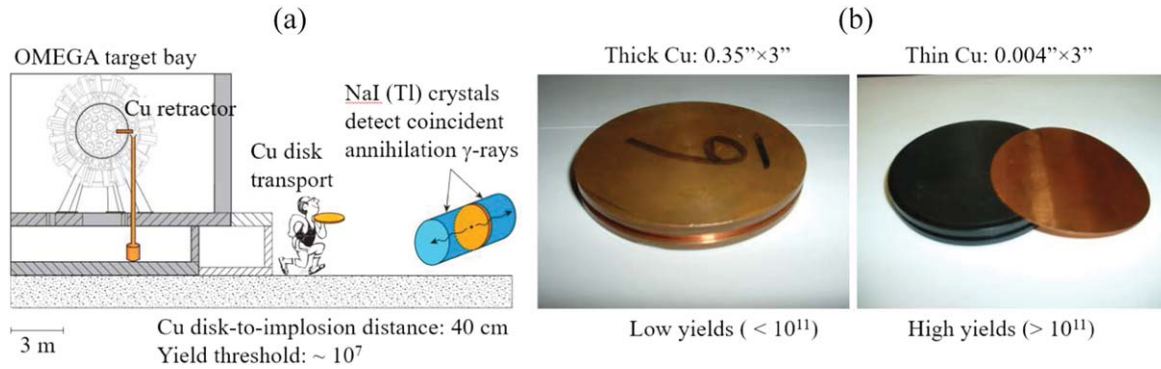
Figure 5. (a) The copper-activation system on OMEGA-60. (b) Thick Cu activation, which is used for low-yield implosions ($Y_n < 10^{11}$), and thin Cu activation, which is used for high-yield implosions ($Y_n > 10^{11}$).

neutron-fluence spectrum generated by a neutron generator in which the neutron production is monitored with the associated-particle technique [94].

In the following sections, the different types of NADs routinely used in the field of ICF are reviewed. For more detailed discussions about the NAD diagnostics, the reader is referred to the papers by Barnes *et al* [95], Bleuel *et al* [96], and Yeamans *et al* [97].

5.1.1. Copper. Copper has been used as NAD material since the beginning of the experimental ICF program for measurements of the emitted DT neutron yield [98, 99]. The technique is based on the $^{63}Cu(n, 2n)^{62}Cu(\beta+)$ reaction that has a threshold of 10.9 MeV. As ^{62}Cu is radioactively unstable, with a half-life of 9.8 min, it decays into ^{62}Ni through positron emission. The emitted positron annihilates with an electron and produces two 0.511 MeV gamma-rays emitted in opposite directions. The Cu-activation system on OMEGA-60 is schematically shown in figure 5(a), where two NaI inorganic scintillators are used to detect the emitted gamma-rays. Similar Cu-activation systems exist at the Z-facility [100], the NIF [101] and LMJ [102, 103].

With a threshold of 10.9 MeV, the Cu-activation measurement is sensitive to both down-scattered and primary *dt* neutrons. In the case of high-ρR implosions at the NIF, down-scattered neutrons with energies above the reaction threshold will affect the yield measurement, and according to calculations [99], typical neutron spectra at the NIF, with a significant down-scattered-neutron component, have been predicted to generate a ~10% lower induced activity than a mono-energetic *dt*-neutron source.

5.1.2. Zirconium. Zirconium is used as activation element in the most NAD systems on the NIF for measurements of mainly un-scattered primary *dt* neutrons [96, 97, 104]. For the detection, the $^{90}Zr(n, 2n)^{89}Zr$ reaction is utilized, and this reaction has a reaction threshold of 12.1 MeV and cross section that gradually increases up to ~0.8 b at 15 MeV. The ^{89}Zr has a 3.27 day half-life and $\beta+$ decays to ^{89m}Y, which subsequently emits a 909 keV *gamma*-ray. The gamma-rays are measured with lead-shielded high-purity germanium detectors in a low-background counting facility. The

uncertainty in the measured un-scattered yield has been estimated to be ~7%, dominated by uncertainties in the calibration and counting-geometry corrections (estimated to be ~5%). Uncertainties associated with absorption and scattering in nearby structures play a role. On the other hand, the $^{90}Zr(n, 2n)$ cross section is known to a 1% uncertainty and does not significantly impact the total uncertainty. It has also been demonstrated that a mono-energetic *dt*-neutron spectrum and a Doppler-broadened *dt*-neutron spectrum with $\Delta E_d = 350$ keV generate spectrum-weighted cross sections of 596 mb and 595 mb, respectively, demonstrating an insensitivity to changes in ΔE_d [96].

The advantage of using zirconium as opposed to copper is that the reaction threshold is higher, which makes the system less sensitive to down-scattered neutrons and thus more ideal to probe un-scattered neutrons emitted in various directions. As the yield of un-scattered primary neutrons carry information about the ρR_{dt} of the region traversed by the primary neutrons (equation (4.17)), a relative ρR_{dt} map can be generated from data obtained with several NADs located around the implosion. These maps often show angular variations consistent with low-mode ρR asymmetries. On about half of the high-foot implosions [105] at the NIF, the FNADs data are fitted with spherical harmonic distributions with modal numbers up to $L = 2$, which show regions of high ρR at the poles (see example in figure 6(a)). The other 50% of the data show residual RMS deviation from the $L = 2$ fit, implying the existence of *L*-mode numbers >2. In implosions of capsules not held with a thin membrane inside the hohlraum, a high ρR feature are often observed close to the fill-tube axis suggesting that at least in the case of a 30 μm diameter fill tube, the impact on the shell symmetry is significant (an example of a ρR perturbation possibly due to the fill tube is shown in figure 6(b)).

The disadvantage of using Zirconium instead of Copper is that the half-life is much longer (3.27 d versus 9.8 min), which means that it takes a longer time to collect data with good statistics. This is not adequate at OMEGA-60 and other smaller ICF facilities where the shot cycle is about an hour, while it is acceptable at the NIF operating at a lower shot rate. In addition, relatively high ρR_{dt} and ρR_{dt} asymmetries are required for this method to be effective.
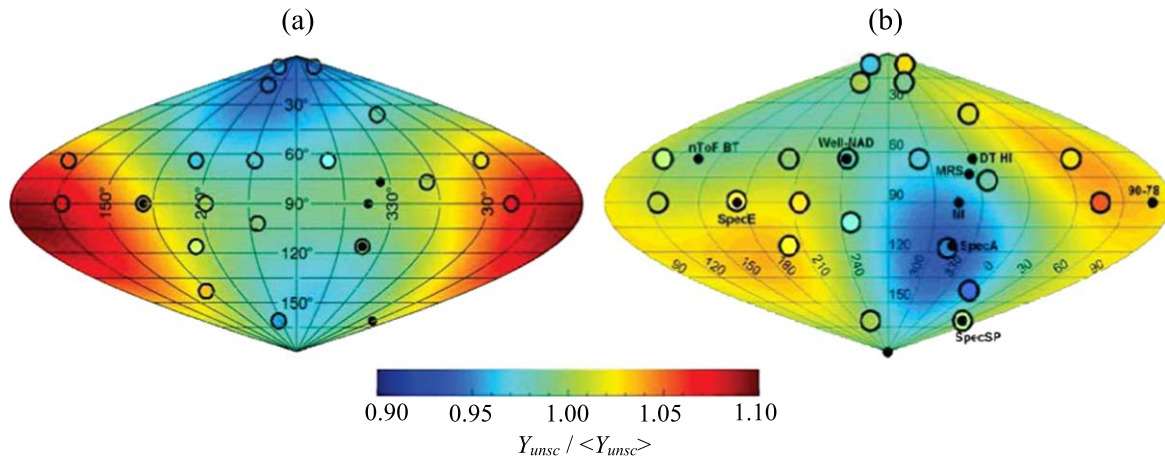
Figure 6. $Y_{unsc}/\langle Y_{unsc}\rangle$ ratio measured with several zirconium NADs (positions indicated by the open circles) for NIF implosions (a) N150422 and (b) N160628. Smaller black data points indicate the positions of the nTOF and the MRS neutron spectrometers used for the dsr measurements (discussed in sections 5.2 and 5.6), from which directional ρR values are determined. The color map was generated by fitting a low-mode spherical harmonics to the data. The data shown in (a) illustrate high ρR values at the poles, while the data in (b) show a high ρR feature at the location of the fill tube. This mass perturbation and associated radiation shadowing may be seeding a large defect that could perturb the stagnated high-density shell. A $Y_{unsc}/\langle Y_{unsc}\rangle$ variation of about $\pm 10\%$ roughly corresponds to a ρR asymmetry of about $\pm 500\,\mathrm{mg\,cm^{-2}}$.

5.1.3. Indium. For detection of *dd* neutrons (equation (3.4)), indium is used as activation element in which the $^{115}\mathrm{In}(n, n')^{115m}\mathrm{In}$ reaction is utilized [101]. As the $^{115}\mathrm{In}(n, n')^{115m}\mathrm{In}$ cross section increases rapidly between 1 and 2 MeV and remains relatively constant around 2.45 MeV, it is quite insensitive to T_i variations, or rather ΔE_d variations. On the other hand, due to low *dd*-neutron yields, a relatively low reaction threshold and a higher sensitivity to scattered neutrons, the indium sample must be positioned close to the implosion, where the mass of nearby structures is minimal. The $^{115m}\mathrm{In}$ isomer emits 336.2 keV gamma-rays with a 4.5 h half-life, and detection of these gamma-rays typically results in a yield uncertainty of $\sim 10\%$. Indium has been used routinely in the past at both OMEGA-60 and the NIF. Today it is used for *dd*-neutron yield measurements at the Z-facility [100] and Shenguang-II facility [106, 107].

5.1.4. Other material. In addition to the standard activation materials, carbon has been explored as an activation element for tertiary neutrons above 22 MeV [108]. As briefly touched upon in section 3.3, the motivation for this measurement was to determine the total ρR of an implosion using the yield ratio between tertiary and primary neutrons. To accurately measure the yield of tertiary neutrons, it was concluded that the carbon sample cannot contain contaminants more than one part per million for this technique to work. In particular, the air with $^{14}\mathrm{N}$ must be removed from the carbon material.

5.2. nTOF spectrometers

For decades, nTOF spectrometers have been used extensively for measurements of the primary *dd* or *dt* neutron spectrum at most large-scaled ICF facilities around the world [109–113]. In addition, nTOFs are now being used for measurements of the down-scattered neutron spectrum [114], primary neutron spectrum (the first three moments) [59, 114], and tt neutron

spectrum [115, 116]. For substantial coverage of the implosion, a suite of nTOF spectrometers with different LOS and distances to the implosion are typically used to probe different aspects of the ICF neutron spectrum.

The nTOF spectrometers are generally based on a current-mode system consisting of a detection medium, either made of a scintillator or chemical vapor deposition (CVD) diamond (new materials, such as quartz crystal is also being implemented as discussed in section 9.1). In the case of a scintillator, it is optically coupled to a photomultiplier tube (PMT) or a vacuum photodiode (PD). High-bandwidth digital oscilloscopes are used to record the nTOF signal trace $s(t)$, which can be described by

$$s(t) = f[E(t)] \cdot \varepsilon[E(t)] \cdot a[E(t)]\frac{dE}{dt}IRF(t), \qquad (5.2)$$

where $f[E(t)]$ is the neutron spectrum, $\varepsilon[E(t)]$ is the energy-dependent efficiency of the nTOF system, $a[E(t)]$ is the beam-line transmission factor, $E(t)$ is the neutron energy versus time-of-flight and expressed as $E(t) = m_n c^2(\gamma - 1)$, where m_n is the neutron mass, $\gamma = (1 - \beta^2)^{-1/2}$, and $\beta = t\gamma/t$ with $t\gamma$ being the time-of-flight of a photon. dE/dt converts the neutron spectrum from energy to time-of-flight and is expressed as $m_n c^2\gamma^3\beta^3/t\gamma$, and $IRF(t)$ is the instrument response function. The nTOF signal trace is typically analyzed by using a forward fit of the data (deconvolution is sometimes used), which involves an analytical description of the neutron spectrum and the different factors in equation (5.2). Examples of nTOF signal traces that have been analyzed using the forward-fit technique are shown in figure 7. From the measured *dt* signal trace, Y_{unsc}[12] can be determined by integrating the signal over the time window corresponding to a neutron-energy range of 13–15 MeV. As

---

[12] Given that the primary-neutron signal is integrated from 13 to 15 MeV, Y_{unsc} discussed here is slightly different from the zirconium-measured Y_{unsc}.
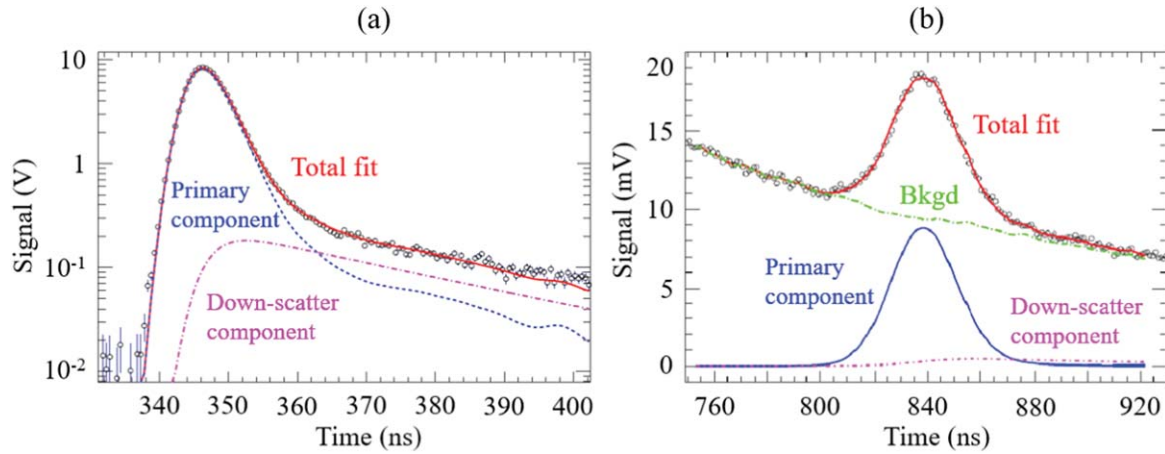
Figure 7. Example of nTOF-signal traces for (a) *dt*-primary and down-scattered neutrons, and (b) *dd*-primary neutrons that is recorded on top of the down-scattered *dt* neutron signal. These signal-traces were obtained with one of the nTOF spectrometers positioned ∼20 m away from the implosion at the NIF. Reproduced from [118]. © IOP Publishing Ltd. All rights reserved.

this is a relative measurement, an absolute yield calibration must be obtained by using other absolute Y_{unsc} measurements. When calibrated, the primary-yield accuracy is typically ∼7%, while the dsr accuracy is ∼10%. The modeling of nTOF data is described in detail in [117].

Positioning an nTOF spectrometer at a large distance from an implosion, while at the same ensuring the solid angle and efficiency are adequate, T_i (the second moment) can be determined from the spread of the neutron arrival times at the detector, which is dictated by the neutron velocity distribution. This spread is caused by Doppler broadening and macroscopic flows in the plasma, as discussed in sections 4.2 and 4.3. If flows are insignificant, T_i can be expressed as

$$T_i = c_1^2 \frac{\Delta t_D^2}{d^2}, \text{ (keV)} \tag{5.3}$$

where Δt_D is the Doppler spread (FWHM) of the neutron-arrival-time distribution in nanoseconds at the detector, d is the neutron flight path in meters, and $c_1 = 1.3$ for *dd* neutrons and $c_1 = 7.8$ for *dt* neutrons. For a given neutron-arrival-time spread and nTOF distance, T_i is 36 times larger for *dt* neutrons than for *dd* neutrons. The accuracy in the T_i measurement is generally in the range of 100–300 eV.

To determine the energy-peak shift (first moment), the time offset of the measured signal must be known to very high accuracy. As discussed in [118], the absolute timing of the detected signal is affected by several terms as described by

$$t = t_0 + t_{offset} + t_{BT} + t_E(E) + t_{fidu}, \tag{5.4}$$

where t_0 is the time between the rise of the drive and actual time when the drive (laser or magnetic drive) hits the target, t_{offset} is the time offset that has to be determined from an x-ray timing shot, t_{BT} is the bang time (peak nuclear burn), $t_E(E)$ is the energy-dependent neutron-time-of-flight time from the implosion to the nTOF spectrometer, and t_{fidu} is the position of the timing fiducial on the oscilloscope trace. At the NIF, t_0 has been established to be ∼30 ps.

X-ray timing shots, which produce x-rays over a short period of time, are routinely used to establish the x-ray-IRF

for an nTOF spectrometer. To convert this x-ray-IRF to a neutron-IRF, the neutron transit time through detecting medium must be taken into account in the analysis. This is done by using neutron-transport simulations, in which the time duration of the neutron-induced charged-particle energy deposition is determined and convolved with the x-ray IRF.

5.2.1. Scintillator-based systems. When neutrons interact with a scintillator they generate charged particles through elastic-scattering processes or nuclear reactions, and these charged particles deposit their energy in the scintillator and produce light mainly in the visible range. The light is subsequently transported to a PMT where it is converted to an electrical signal that is amplified. At high neutron yields, the PMT is often replaced with a lower-gain PD. The first nTOF spectrometers implemented on ICF facilities were generally on-axis systems where the PMT was directly exposed to the incoming neutrons. This was not optimal from a signal-to-background (S/B) point of view, as unwanted background was generated in the PMT. More recent nTOFs are off-axis systems, where the PMT is positioned behind a shielding and outside the collimated beam of incoming neutrons. To obtain highest possible signal-to-noise (S/N) ratio, a scintillator is often viewed by up to four off-axis PMTs/PDs. The signals from these are recorded on several oscilloscope channels with different sensitivity settings, and the data obtained are often stitched together to generate a complete signal time trace that includes both the primary and down-scattered-neutron signals. Examples of off-axis nTOF spectrometers on OMEGA, the NIF, and the Z-facility are shown in figure 8.

Fast plastic scintillators were initially used for the nTOF spectrometers on most ICF facilities, but at OMEGA and the NIF these plastic scintillators were replaced by liquid Xylene scintillator with a faster decay time [110]. At the NIF, the Xylene detectors were in turn recently replaced by Bibenzyl crystals [119, 120], which are even faster than the liquid Xylene. This feature made it possible to reduce the mass in the nTOF spectrometers, as illustrated in figure 8(b), which
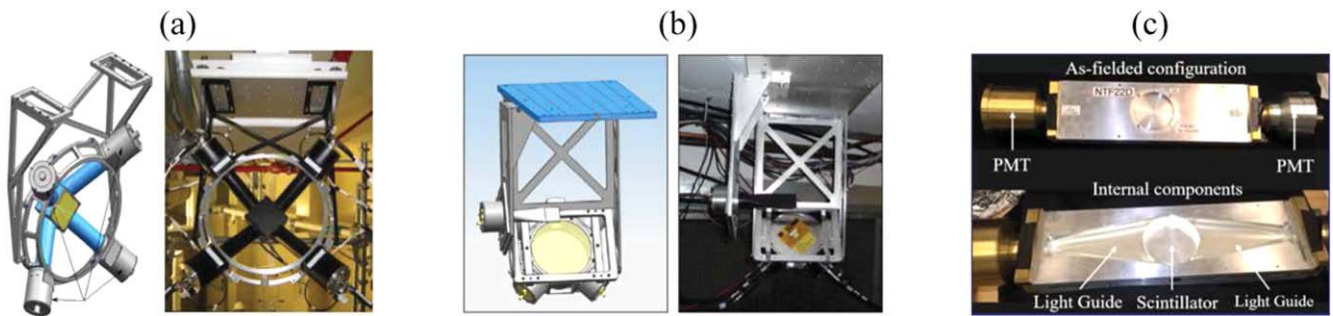
Figure 8. Off-axis nTOF spectrometers on (a) the NIF, (b) OMEGA-60 and (c) the Z-facility. A collimated beam of neutrons hits the scintillator (marked yellow in (a) and (b)), which is observed by a set of off-axis PMTs/PDs positioned around the scintillator. In the case of OMEGA-60, a smaller off-axis system is also positioned in front of the bigger nTOF spectrometer.
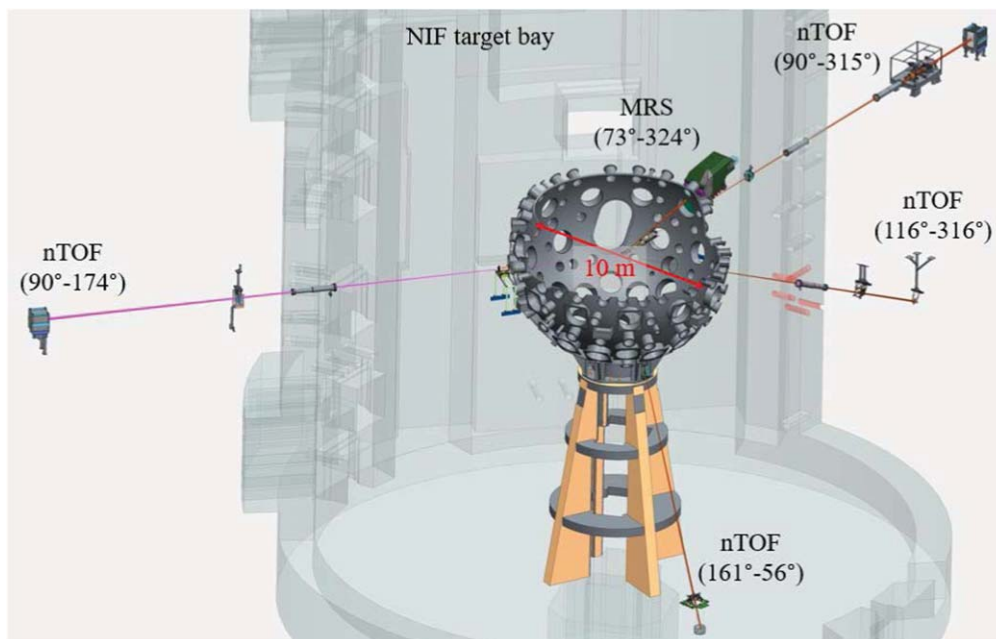
Figure 9. The nTOF spectrometers on the NIF for measurements of primary and down-scattered-neutrons. These spectrometers are positioned $\sim$20 m from the implosion, and each system consists of collimators, a scintillator, and off-axis PMTs/PDs that are shielded. Each LOS is specified in the figure by the polar-azimuthal angles. Additional nTOFs for primary and down-scattered neutron measurements have been fielded at 90°–315° and close to the North Pole. The magnetic recoil spectrometer (MRS), positioned on the 10 m diameter chamber, is also shown. The MRS is discussed in detail in section 5.6.

resulted in a lower background of scattered neutrons. The locations of the $\sim$20 m nTOF spectrometers on the NIF for both primary and down-scattered neutron measurements are shown in figure 9. More detailed discussions about nTOF systems on OMEGA-60, the NIF, the Z-facility, LMJ, Gekko-XII and Shenguang III can be found in [109–113].

5.2.2. Chemically-vapored-deposition (CVD) diamond detector. A CVD diamond detector is ideal for measurements of neutrons, gamma-rays and charged particles. Given its fast time response (of $\sim$200 ps) and relatively low efficiency, it has been used routinely for measurements of primary neutrons in high-yield applications at OMEGA-60 [121] and for measurements of bang time in implosions at the NIF [122]. The CVD is made of a wafer that is biased along its axis, and when high-energy particles

interact with the material they generate electron–hole pairs that are drawn out by a bias field, which produces a time-dependent voltage that is recorded on an oscilloscope.

As the CVD diamond detector is compact and vacuum-compatible, it can be fielded close to an implosion to maximize signal statistics and minimize particle time-of-flight spread, making it ideal for yield and bang-time measurements. Given that the CVD sensitivity to protons is about three orders magnitude higher than for neutrons, when considering interaction probabilities, it is used for simultaneous measurements of shock- and compression-bang times using d^3He protons ($\sim$10^8) and dd neutrons ($\sim$10^{11}), respectively, in D^{3}He gas-filled surrogate experiments at the NIF. This diagnostic is called particle time-of-flight (pTOF) diagnostic [122], and is illustrated in figure 10. An example of pTOF data is shown in figure 11. With a fast rise time, the
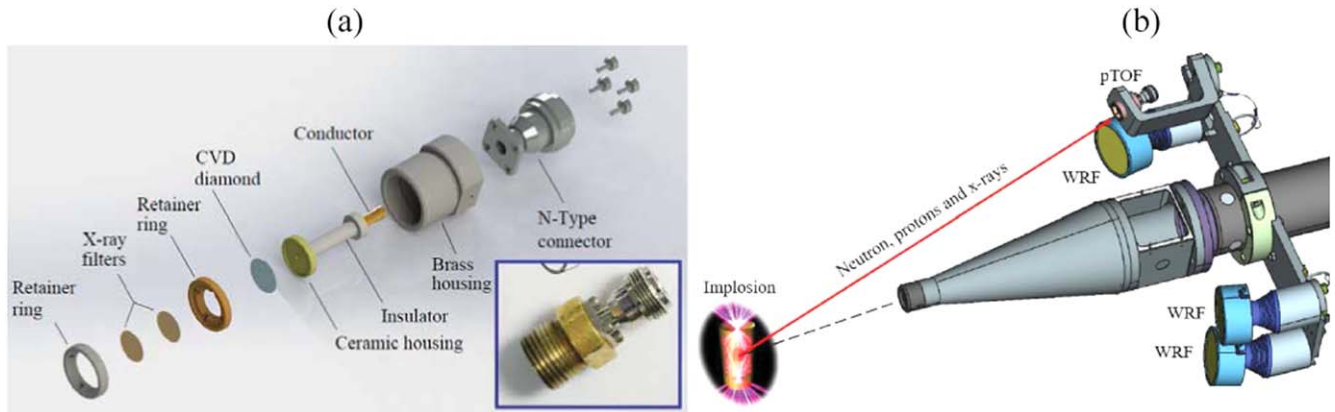
Figure 10. (a) Components of the CVD diamond detector used in the pTOF diagnostic on the NIF. The insert illustrates the assembled system. (b) A CAD model of the pTOF diagnostic mounted on an external bracket attached to a diagnostic insertion manipulator (DIM). Three wedge range filter (WRF) spectrometers, discussed in detail in section 7.2, are also mounted externally on the 90°–78° DIM.
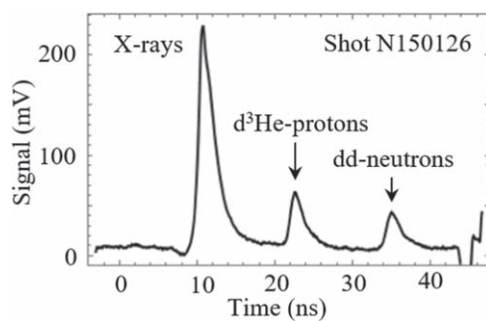
Figure 11. Example of a pTOF signal trace from NIF shot N150126. This trace shows the hohlraum x-rays, d^3He protons originating from the shock-burn phase, and dd neutrons from the subsequent compression phase. During the compression phase, the ρR is often high enough to range out the d^3He protons. At ~46 ns, the negative timing fiducial signal is observed.

signal is measured with a timing accuracy that is better than ± 50 ps.

5.2.3. Single-hit spectrometers. Single-hit spectrometers have been used extensively for low-yield applications at NOVA [123, 124], OMEGA-60 [125] and Gekko XII [126]. These systems, which are high-efficiency spectrometers, consisted of an array of scintillators, each coupled to a PMT, followed by a discriminator, Time-to-Digital Converter and Analog-to-Digital Converter that were used to record the neutron arrival time and pulse height. From the distribution of the neutron arrival times, a neutron spectrum could be constructed. At NOVA, the large area neutron scintillator array (LaNSA) comprised of 960 scintillators that were positioned 20 m away from the implosion [123]. This system was capable of measuring secondary dt-neutron yields as low as $\sim 2 \times 10^5$ (100 detected hits) with a resolution of 2.3 ns (or 170 keV for 14 MeV neutrons with a flight path of 20 m), from which a fuel ρR in D_2 gas-filled, low-CR implosions was determined [127, 128]. As the system had very high efficiency, the primary dd-neutron spectrum could not be measured because of too many channels were triggered. However, LaNSA was used to diagnose the high-

energy tail of the primary dd-neutron spectrum [129]. Another single-hit spectrometer was the Tion diagnostic that was implemented by Los Alamos National Laboratory (LANL) on NOVA. This system consisted of 1020 detectors each made up of a scintillator and photomultiplier tube. The Tion array was $\sim 100 \times$ less sensitive than LaNSA and thus could operate at higher yields. In particular, the capability to measure the leading edge of the neutron-arrival-time distribution (before it saturated by the bulk of the primary neutrons). It was also used to characterize mix in ICF implosions either by measuring the yield from deuterated plastic capsule implosions, or energy spectra of secondary neutrons produced in medium-converging implosions [130].

5.3. Nuclear burn-history detectors

The nuclear burn history, or the fusion reaction rate, was first measured in the 90s with a Neutron Temporal Diagnostic (NTD) on NOVA [131]. Using the experience gained with this diagnostic, another NTD was built and optimized for OMEGA-60 about a decade later [132]. Building upon the NTD technique, the Particle Temporal Diagnostic (PTD) was subsequently implemented on OMEGA-60 for measurements of primary dd and d^3He burn histories as well as the secondary d^3He burn history [133], followed by the implementation of the Particle x-ray Temporal Diagnostic (PXTD) for simultaneous measurements of multiple burn histories and x-ray emission history (in different energy bands) [134].

These systems are all based on a fast organic scintillator (BC-422) that is positioned close to the implosion for minimization of the particle time-of-flight broadening (see equation (5.3)). Thin scintillators are also used to minimize the transit time of the particles across the thickness of the scintillator for optimal time resolution. When neutrons, charged particles and x-rays interact with the scintillator, light is generated that is collected by a collection lens. This light is subsequently transported through an optical-relay system to an optical streak camera, positioned either outside the target chamber or behind the target-bay wall. A schematic of the PTD is illustrated in figure 12.
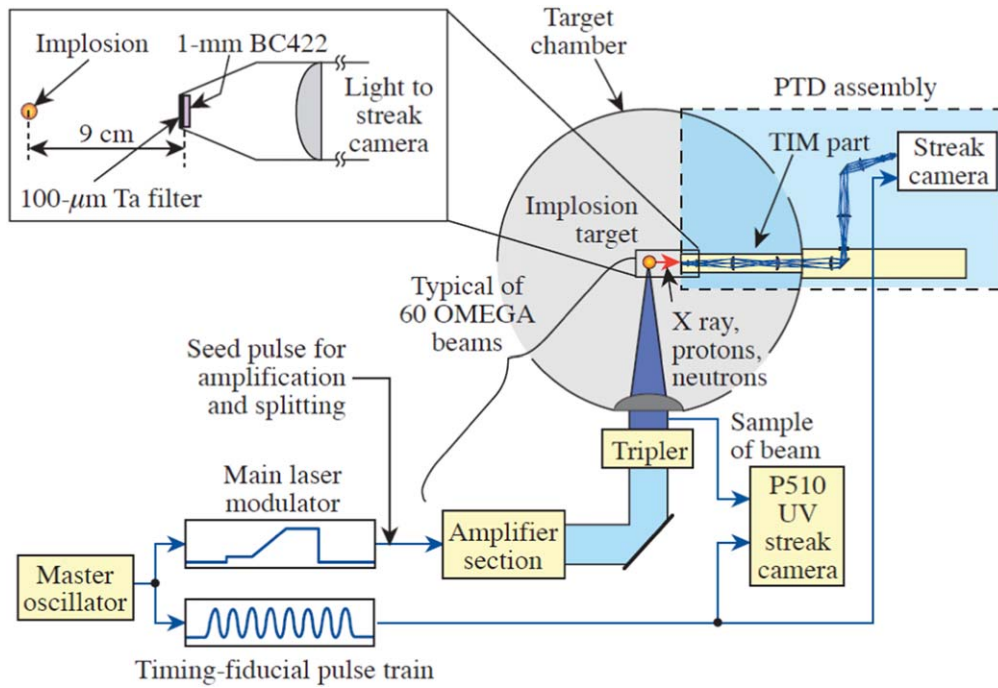
Figure 12. Schematic of the PTD on OMEGA-60. This system uses a 3.5 m optical relay to transport light from the scintillator positioned at 9 cm from the implosion to an optical streak camera outside the target chamber. The timing-fiducial system provides cross-timing between the signals and incident laser pulse, which are recorded on the P510 UV streak camera. A zoomed-in schematic view of the PTD front end is also shown, which consists of a 1 mm thick scintillator with 100 μm tantalum filter in front. Part of this figure is reprinted from [132], with the permission of AIP Publishing.

As the BC-422 scintillator has a fast rise time (<20 ps) and long decay time (~ 1.4 ns), the information of the nuclear burn history is encoded in the leading edge of the streaked signal image. To obtain this information, the effect of the scintillator decay is deconvolved from the recorded signal, and the model used for this is given by

$$S_i = T_i - \sum_{j=0}^{i-1} S_j e^{\frac{(i-j)\Delta t_p}{\tau}}. \tag{5.5}$$

Here, S_i is the measured signal at the pixel location i, which is the difference between the total signal T_i and the sum of previous signals that decay exponentially. In addition, Δt_p is the time separation of two pixels. As discussed in [132], this method is fast, reliable and insensitive to noise in the streak camera signal. Although the scintillator is positioned close to the implosion, the temporal broadening of the signal due to spectral broadening must also be considered in the deconvolution process.

An example of a raw PTD streaked image and projected primary-dd and secondary-d^3He signals are shown in figure 13. For an absolute timing reference of the streaked image, timing fiducials are used to generate a series of light pulses spaced 548 ps apart (see top-part of the image), which is delivered via an optical fiber. The fiducial pulses are also used to correct for any sweep nonlinearities.

To enable measurements of multiple nuclear-reaction and x-ray-emission histories (in different energy bands), the PXTD was recently implemented. This system uses either two or three scintillators combined with more complex filtering. The main challenge with this diagnostic is to keep the signals

levels well within the dynamic range of the optical streak camera. The reason for this is that dd neutrons produce $\sim 600\times$ less photons than d^3He protons. This is due to the fact that a small fraction of neutrons interacts and deposits energy in the scintillator, whereas every d^3He proton deposits energy in the scintillator. In the case of Bremsstrahlung x-rays, the signal levels vary significantly depending on the energy band. For a robust simultaneous measurement of these emission histories, the signal levels must be within a factor of five, which is accomplished by adjusting the light-attenuation filters behind each scintillator. Figure 14 illustrates examples of streak images from the 2-channel or 3-channel PXTD.

5.4. Imaging systems

A neutron-imaging system typically consists of a pinhole (and/or penumbral aperture), a mechanical alignment system for the pinhole/aperture, and an imaging detector. Due to the penetrating nature of the neutrons, the pinhole/aperture must be very thick, which results in a narrow field of view and very tight alignment tolerances. The detector typically consists of either a bundle of scintillation fibers or capillary tubes filled with a liquid scintillator. Either penumbral or pinhole imaging (or in some cases both techniques) are used to image an ICF implosion [135]. Penumbral imaging involves a coded aperture and conceptually it is similar to pinhole imaging, with the essential difference that the aperture is larger than the source. The detected image consists of an umbra and a penumbra. The former region is exposed to the entire source through the aperture, while the latter is progressively obscured from the
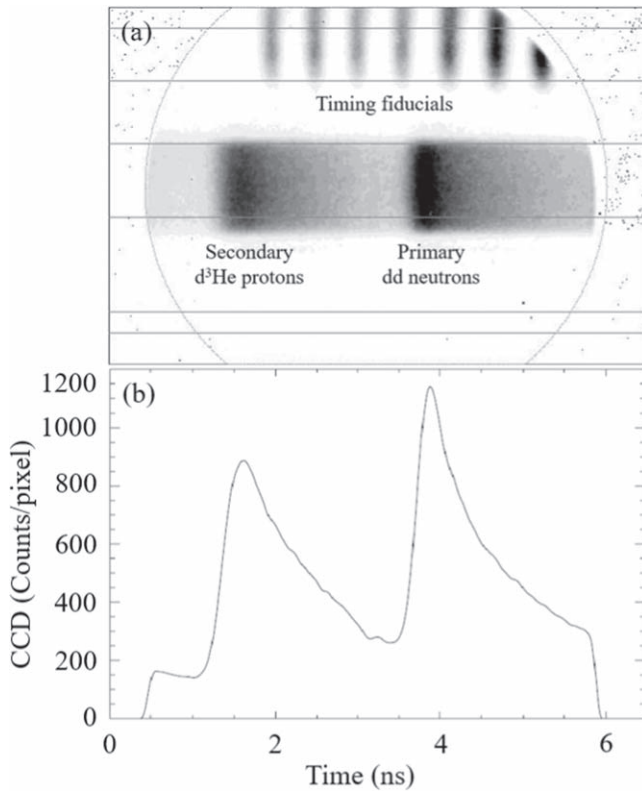
Figure 13. (a) PTD streak image for a D_2 gas-filled capsule implosion (shot 38309). This image illustrates secondary d^3He-proton and primary dd-neutron signals. Due to a higher velocity, the d^3He protons arrive at the scintillator before the dd neutrons. The fiducials appear at the top of the streak image and are used for absolute timing relative to the laser pulse, and for possible adjustment of any sweep non-linearities. (b) Projected signal on the time axis. Both signals are sitting on top a decaying x-ray background.

source by the aperture edges. The information about the source is therefore encoded in the penumbra.

In the case of a penumbral aperture, the neutron transmission through the material in the aperture determines the spatial resolution. In the small-angle approximation, the spatial blurring of the point spread function is dictated by the field-of-view and aperture-to-implosion distance (L_0). When considering the detector resolution (ΔS_{det}), the total resolution (ΔS_{tot}), represented by the FWHM, is given by

$$\Delta S_{tot} = \sqrt{\left(\frac{\ln 2 \cdot FOV}{2\mu L_0}\right)^2 + \Delta S_{det}^2 \left(\frac{L_0}{L_i}\right)^2}, \qquad (5.6)$$

where μ is the attenuation of the neutrons through the aperture material and L_i is the detector-to-implosion distance.

The first neutron-imaging system was implemented on NOVA in the 80s [136]. This system was based on a penumbral coded aperture, and provided the first neutron images of an ICF implosion. In these measurements, shock-driven implosions were imaged with a limited spatial resolution ($\sim$60 μm), dictated by the relatively low magnification and long range of the elastically-scattered recoil protons in the scintillator.

At OMEGA-60, the Commissariat à l'Énergie Atomique (CEA) fielded and successfully used a penumbral imaging system combined with a detector based on 85 μm diameter capillary tubes filled with a liquid scintillator [137]. This was done in preparation for the implementation of a system on the LMJ laser. Figure 15 shows a schematic of the imaging system on OMEGA-60. The first reincarnation of the detector had a resolution of $\sim$650 μm (FWHM) at 14 MeV, which was dictated by the track length of elastically-scattered recoil protons in the scintillator material. With this system, images were recorded with a resolution of $\sim$20 μm and signal-to-noise (S/N) ratio of $\sim$40 [138]. Images of dd neutrons from D_2 gas-filled capsule implosions were also recorded with this system.

A one-dimensional neutron imager, called ODIN, has been implemented on the Z-facility for imaging dd-neutrons [139]. This system is primarily intended for imaging MagLIF cylindrical implosions that are about 10 mm long and 100 μm in diameter. As discussed in the paper by Ampleford *et al* [139], ODIN system uses an extended, rolled-edge slit that is centered 22 cm from the implosion. CR-39 is used as the principle detector that is positioned 79.5 cm from the slit, providing a modest magnification of 3.6. This system is designed to provide a 500 μm axial resolution over the entire implosion length with good signal-to-noise ratio for dd-neutrons yields above 10^{12}. The key components of ODIN is shown in figure 16.

At the NIF, the first neutron-imaging system has been implemented and extensively used to diagnose the size and shape (in particular low-mode asymmetries) of the hot-spot and surrounding the high-density shell [140]. This is done by imaging primary dt-neutrons and down-scattered neutrons (that mainly scatter within the surrounding high-density fuel shell). To separate these neutrons, the detector system is gated to record primary neutrons with energies between 13 and 17 MeV and down-scattered neutrons from 6 to 12 MeV. For a high-quality image of the down-scattered neutrons, which are recorded after the primary neutrons, the scintillator output from the primary signal must decay at least three orders of magnitude before the lower-energy neutrons can be recorded.

The imaging system on the NIF, shown in figure 17, consists of an array of pinholes and penumbral apertures (see insert in figure 17) positioned 26.5 cm from the implosion, and a scintillating fiber array positioned 28 m from the implosion, which provides a magnification of $\sim$85 [141, 142]. This system was designed to provide a spatial resolution in the vicinity of 10 μm for yields above 10^{15}. Examples of primary and down-scattered neutron images are shown in figure 18.

5.5. CR-39 detectors

CR-39 is a transparent plastic with a chemical composition of $C_{12}H_{18}O_7$, and this material has been used to detect neutrons, from which an absolute yield of primary neutrons emitted from an ICF implosion was determined [143]. The CR-39 detection of neutrons is a two-step process. The first step is the generation of an energetic charged particle in the CR-39, either through elastic scattering or nuclear reaction. This charged particle leaves a trail of damage along its path in the CR-39 in the form
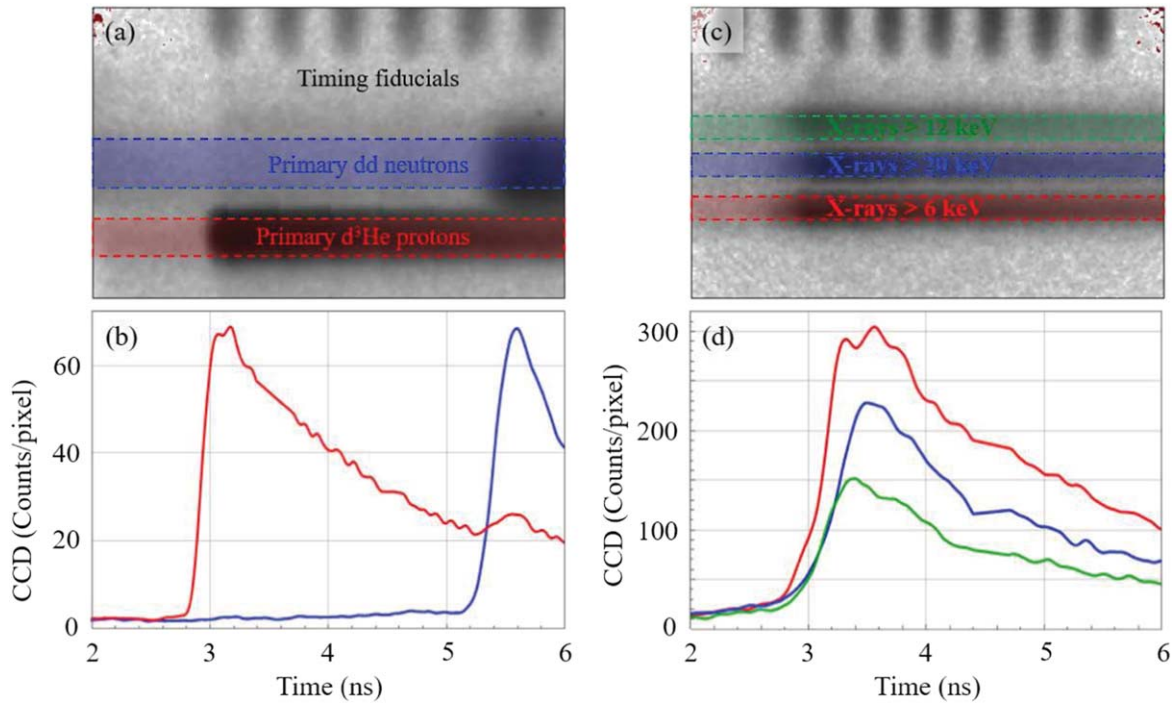
Figure 14. (a) 2-channel PXTD streak image of the primary *dd*-neutron and *d*³He-proton signals. This data was generated by a D³He gas-filled (with trace argon) capsule implosion (shot 77119). Due to a higher velocity, the *d*³He protons arrive at the scintillator ∼2 ns before the *dd* neutrons. (b) Projected *d*³He-proton and *dd*-neutron signals on the time axis. (c) 3-channel PXTD streak image of the x-ray signal in three energy bands. This data was obtained from a T_2 gas-filled (capsule implosion (shot 80705)). (d) Projected x-ray signals on the time axis. Reprinted from [134], with the permission of AIP Publishing.
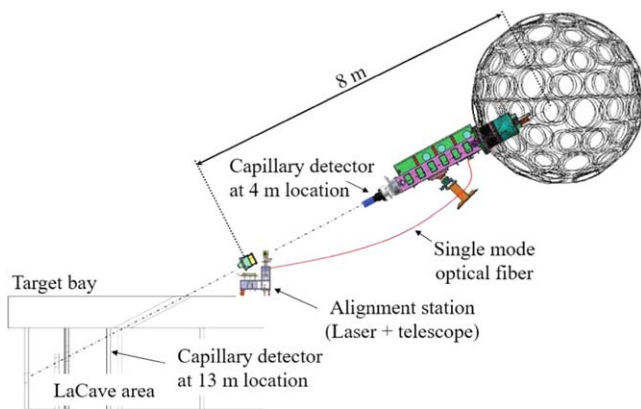
Figure 15. The CEA neutron imaging system on OMEGA-60. The penumbral aperture is centered at 26.6 cm from the implosion, and the detector can be positioned at either 4 or 13 m from the implosion for different magnifications. Reprinted from [138], with the permission of AIP Publishing.

of broken molecular chains and free radicals. The level of damage along the path is related to the rate at which energy is lost by the charged particle (or dE/dX in the CR-39). The second step involves making the trails of damage visible for detection. This is done by etching the CR-39 in NaOH, in which the CR-39 surface is etched away at a bulk-etch rate (of ∼2 μm h^{-1} in 80 °C 6 M NaOH), while damaged material along the particle trail etches at a faster rate called track-etch rate.

To determine the absolute primary-neutron yield from the CR-39 data, the neutron-interaction processes and generation

of tracks in the CR-39, and thus the CR-39 neutron detection efficiency, must be understood. Both *dd* and *dt* neutrons can scatter elastically, producing recoil protons, carbon and oxygen nuclei in the forward direction in the laboratory system. The *dt* neutrons can also undergo (n, p) or (n, α) reactions with carbon or oxygen nuclei, generating charged particles that can produce tracks on the front and/or back side of the CR-39. The CR-39 neutron detection efficiency is the probability that an incident neutron generates a charged particle, which leaves a visible track on the etched CR-39 surface, and it is ∼10^{-4} for *dd* neutrons and ∼5 × 10^{-5} for *dt* neutrons. For more details about how the CR-39 is used as neutron detector for ICF applications, the reader is referred to [143, 144].

5.6. Recoil-particle systems

5.6.1. Magnet-based spectrometers. As discussed in section 2, obtaining experimental information about T_i, Y_n, ρR and their asymmetries is central to building a picture of an implosion during the nuclear phase. To access this information, a neutron spectrometer called a magnetic recoil spectrometer (MRS) has been implemented and extensively used for measurements of the absolute neutron spectrum in the range of 5–30 MeV at OMEGA-60 and the NIF [145–149]. This range covers all essential details of the ICF neutron spectrum shown in figure 1. In addition, the MRS nicely complements the nTOF spectrometers used to diagnose the same implosion parameters.

As discussed in detail in [145, 146], the MRS consists of either a CD (or CH) foil positioned close to the implosion for generation of recoil deuterons (or protons), a focusing magnet
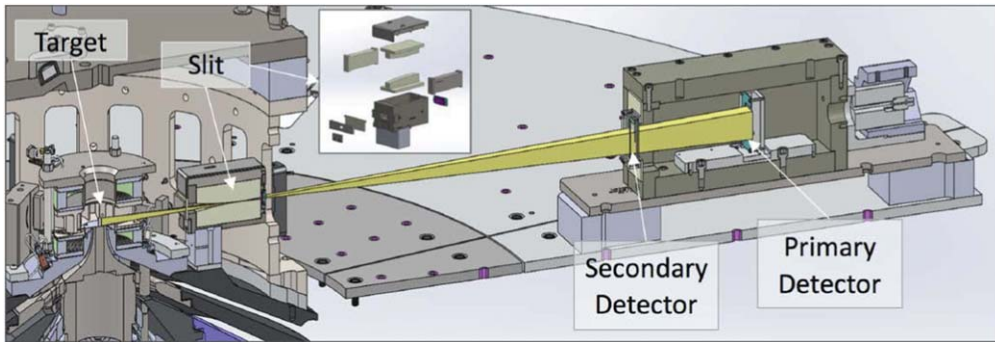
Figure 16. The one-dimensional imager of neutrons (ODIN) on the *Z*-facility. The ray trace shown as yellow indicates the signal trajectories through the system. An exploded view of the slit assembly is shown in the insert. The primary and secondary detector locations are also shown. Reprinted from [139], with the permission of AIP Publishing.
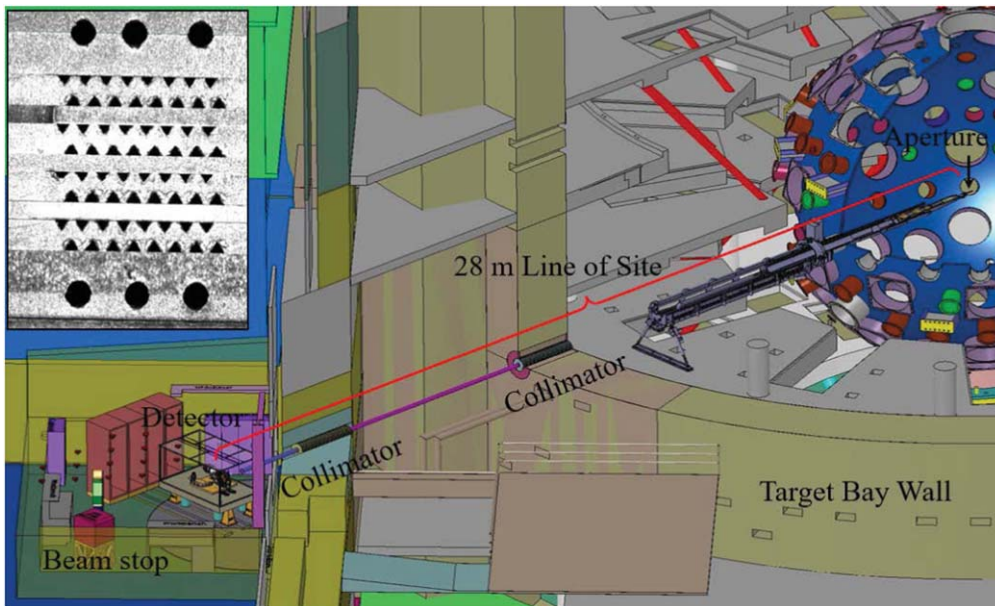
Figure 17. The NIF neutron imaging system for simultaneously imaging primary and down-scattered neutrons. The system consists of an aperture, two collimators and a detector system. The insert in the top-left corner illustrates the array of pinholes and penumbral apertures used for the neutron-imaging system. Adapted with permission from [142]. © (2017) Society of Photo-Optical Instrumentation Engineers (SPIE).
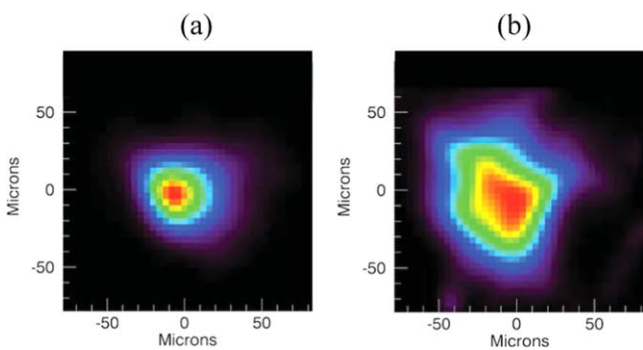
Figure 18. An example of (a) a primary-neutron image, and (b) a down-scattered neutron image obtained from NIF shot N120205. The size of the primary-neutron image is $28 \pm 3 \, \mu$m, and the down-scattered neutron image is $44 \pm 5 \, \mu$m. Qualitatively, the size difference between these images provides information about the configuration of the high-density fuel shell that surrounds the hot-spot.

located outside the target chamber for energy dispersion and focusing of the recoil particles onto the focal plane of the spectrometer, and an array of CR-39 detectors positioned at the focal plane. The foil thickness and area are of order $100 \, \mu$m and $10 \, \text{cm}^2$, respectively. An aperture of $\sim 20 \, \text{cm}^2$ is positioned in front of the magnet for the selection of forward-scattered recoil particles, and the array of CR-39 detectors records the position of each recoil particle with a detection efficiency of 100%. A schematic of the MRS on OMEGA-60 and the NIF is shown in figure 19.

The efficiency (ε_{MRS}) of the system is given by

$$\varepsilon_{MRS} = \frac{\Omega_f}{2} n_d t_f \int_0^{\theta_{\max}} \sin\theta \frac{d\sigma(\theta)}{d\Omega_{lab}} d\theta. \tag{5.7}$$

Here, Ω_f is the solid angle subtended by the foil, n_d is the deuterium (or hydrogen) number density in the foil, t_f is the thickness of the foil, and $d\sigma(\theta)/d\Omega_{lab}$ is the differential cross
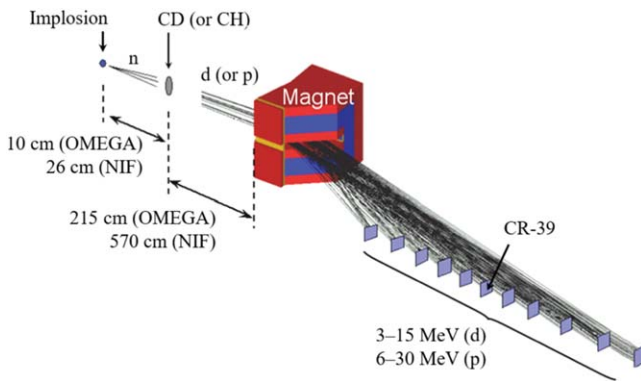
Figure 19. A schematic of the MRS. The main components of the MRS are a CD (or CH) foil, a magnet, and an array of CR-39 detectors. The foil is positioned 10 and 26 cm from the implosion at OMEGA and the NIF, respectively; the magnet is positioned 215 cm from the foil on OMEGA and 570 cm from the foil on the NIF. An array of eleven and nine $7 \times 5 \, cm^2$ CR-39 detectors are positioned at the OMEGA-MRS and NIF-MRS focal plane that is 166 and 84 cm long, respectively. The trajectories shown are for proton energies from 6 to 30 MeV, corresponding to deuteron energies from 3 to 15 MeV. Reprinted from [146], with the permission of AIP Publishing.

section for the elastic scattering in the laboratory system, which is integrated over the scattering angles defined by the aperture. Typical efficiencies are in the range of 10^{-9} to 10^{-12}, depending on configuration. The total energy resolution (ΔE_{MRS}) is part of the spectrometer IRF, which is defined as the recoil-particle spectrum at the detector plane when viewing a fluence of mono-energetic neutrons, and can be expressed as

$$\Delta E_{MRS} = \sqrt{\Delta E_{foil}^2 + \Delta E_{kin}^2 + \Delta E_{magnet}^2}, \qquad (5.8)$$

where ΔE_{foil} is the broadening associated with the energy-loss distribution of the recoil particles in the foil (depending on the scattering location in the foil, the recoil particles show an energy-loss distribution from zero up to a maximum energy loss proportional to t_f), ΔE_{kin} is the kinematic-energy broadening dictated by the scattering-angle distribution of the recoil particles (which depends on the position and area of the foil and magnet aperture), and ΔE_{magnet} ion-optical broadening due to focusing aberrations in the magnet. These mechanisms are to the first order uncorrelated and Gaussian in shape. The MRS system is optimized to maximize the detection efficiency ε_{MRS} for a specified ΔE_{MRS}.

The main source of background are neutrons scattered by the chamber wall and other structures nearby the MRS. x-rays and gamma-rays are not an issue since the CR-39 is insensitive to these types of radiation. Even though the CR-39 efficiency for detecting primary neutrons is small, the impact of the neutron background must be reduced significantly for the down-scattered neutron measurement at OMEGA and the NIF. This is achieved by fully enclosing the spectrometer with polyethylene shielding as a first step (see figure 20), and positioning the CR-39 detector array in the shadow of the NIF-target chamber. Through neutron-transport simulations using the MCNP code [150], it was established

that the shielding reduces the neutron fluence about two orders of magnitude at the NIF. Additional reduction of the neutron-induced and intrinsic background is required for the down-scattered neutron measurement [151]. This is accomplished by the coincidence counting technique (CCT), which utilizes the fact that incident signal particles (protons or deuterons) pass straight through the CR-39 material, resulting in front and backside tracks that are correlated, while neutron-induced and intrinsic background tracks are mainly on one of the surfaces. Applying the CCT to OMEGA-MRS data has demonstrated orders of magnitude S/B improvement [151].

Several options are available for configuring the MRS: the foil composition determines whether recoil protons or deuterons are used, and the foil area and thickness dictate the energy resolution and detection efficiency. As for other neutron diagnostics, the MRS performance improves as yield and ρR increases (under the assumption that the signal and background levels do not saturate the diagnostic). Another system, based on the MRS concept has also been designed in China [152].

The neutron spectrum is determined from a forward-fit, convolved with the IRF, to the measured position histogram of the recoil protons (or deuterons). An important strength of the MRS is that the technique is accurately characterized from first principles (*ab-initio*), enabling quantitative IRF calculations to be performed before the system has been built. An *in-situ* calibration was required, however, to check that the systems had been built and installed according to specification. An example of MRS data from the NIF is shown in figure 21.

6. Gamma-ray diagnostics

In contrast to the many types of neutron diagnostics used at an ICF facility, the number of gamma-ray techniques used to diagnose an implosion is quite limited. One of the reasons for this is that the gamma-ray yield per produced neutron is very low [153] (see the branching ratios in equations (3.2), (3.3), (3.6) and (3.11)), limiting the types of diagnostics that can be used for ICF applications. The advantage of using gamma-rays to diagnose an ICF implosion, however, is that they do not display time-of-flight broadening at the diagnostic, which enables gamma-ray-based systems to be positioned at relatively large distances from an implosion in well-shielded locations. This makes gamma-ray diagnostics ideal for measurements of the nuclear burn history in environments with large x-ray and neutron backgrounds. As discussed in the next section, gamma-ray diagnostics also represent an excellent complement to the NTD, PTD and PXTD as discussed in section 5.3.

6.1. Gas-Cherenkov detectors

Diagnostic systems based on the Cherenkov technique have been implemented and extensively used at high-yield facilities such as OMEGA-60 and the NIF [154, 155]. In these systems, the gamma-rays interact with a high-Z converter,
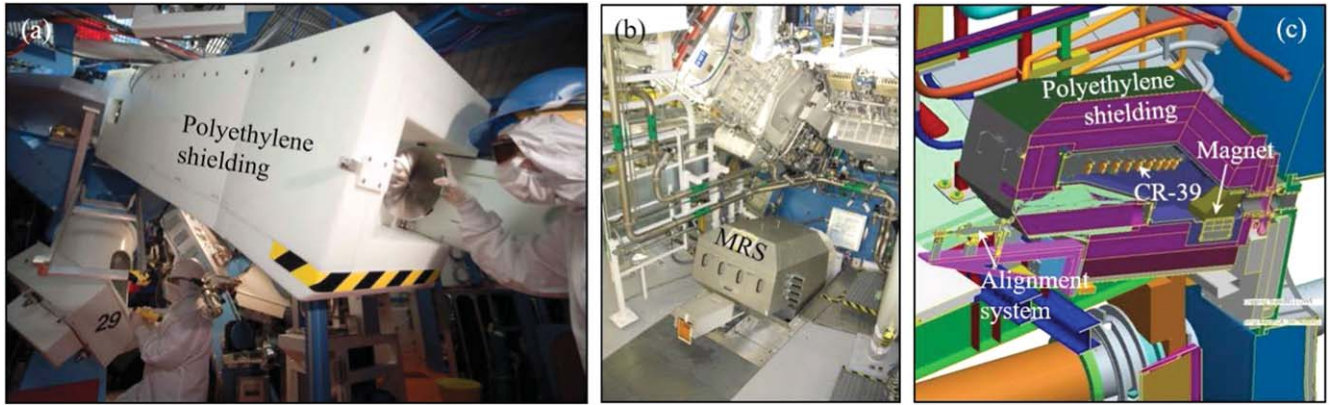
Figure 20. (a) The OMEGA-MRS fully enclosed by polyethylene shielding. (b) The NIF-MRS fully enclosed by polyethylene shielding. (c) Cut-out view of the NIF-MRS illustrating the spectrometer inside the shielding. Reprinted from [146], with the permission of AIP Publishing.
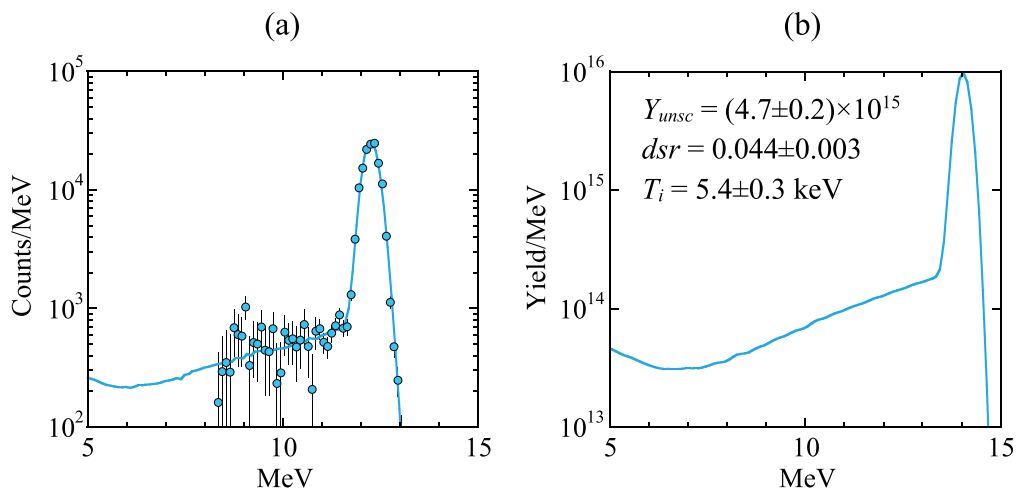
Figure 21. (a) MRS spectrum from NIF shot N150218. A CD foil with thickness and area of 55.8 μm and 3 cm^2 was used, respectively. (b) Modeled neutron spectrum that provides the best fit to measured recoil-deuteron spectrum. From the modeled neutron spectrum, Y_{unsc}, dsr (or ρR) and T_i were determined.

positioned at the diagnostic front end, which generates forward-directed relativistic electrons (mainly through the Compton-scattering process) that are emitted into a high-pressure gas cell. If the electrons travel faster than the speed of light in the gas, typically CO_2 gas, the electrons generate Cherenkov light in the UV/visible range. The minimum gamma-ray energy ($E\gamma$) required for generation of Cherenkov light is described by [156]

$$E_\gamma = \left[\frac{1}{\sqrt{1 - 1/n^2}} - \frac{1}{2} \right] m_e c^2, \qquad (6.1)$$

where n is the refractive index of the medium, m_e is the rest mass of the electron, and c is the speed of light in vacuum. This expression is derived under the consideration that the full backscatter (i.e. 180° Compton-scattering) sets the lower energy limit.

The generated Cherenkov light is relayed to either an optical streak camera or PMT, using a series of off-axis parabolic mirrors. The voltage signal from the PMT is used to modulate a light signal, via a Mach–Zehnder interferometer, which is relayed with high fidelity to a digitizer.

Two types of Cherenkov-based diagnostics have been implemented by LANL and collaborators on OMEGA-60 and the NIF. The first system is the Gamma Reaction History (GRH) system [154, 155], which is positioned on the OMEGA-60 and NIF target chamber at approximately 1.7 m and 6 m from implosion, respectively. The GRH system on the NIF consists of four high-pressure gas cells, each pressurized to a specific pressure to probe gamma-rays above a certain energy (see figure 22). With four channels operated with different energy thresholds, typically at 2.9, 5.0, 8.0, and 10 MeV, this diagnostic probes the emission history of 16.75 MeV gamma-rays produced by dt reactions and 4.44 MeV γ-rays generated by $^{12}C(n, n\gamma)$ reactions in the remaining HDC or CH ablator [157, 158]. The NIF-GRH uses a PMT, resulting in an IRF of 86 ps, which prevents measurements of high-order moments in the gamma-ray emission history.

As higher-order moments in the nuclear burn history contain important information about shock reverberations and burn truncation (due to various implosion failure modes), a faster gamma cherenkov detector (GCD) shown in figure 23
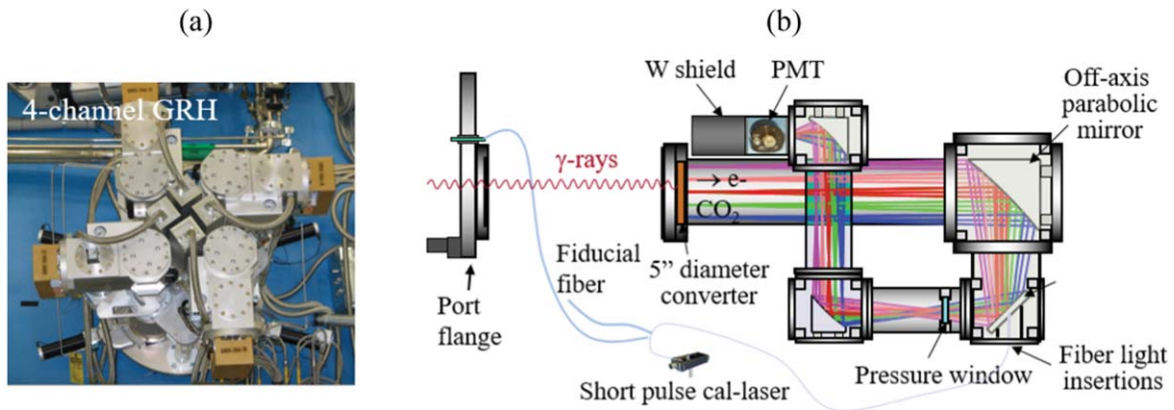
Figure 22. (a) Picture of the 4-channel gamma reaction history (GRH) diagnostic on the NIF for measurement of the gamma-ray emission history. (b) Schematic of one GRH channel. This configuration generates a time delay of 4.3 ns that allows the detector to recover from prompt radiation due to laser-plasma interactions from the target. See text for more details.
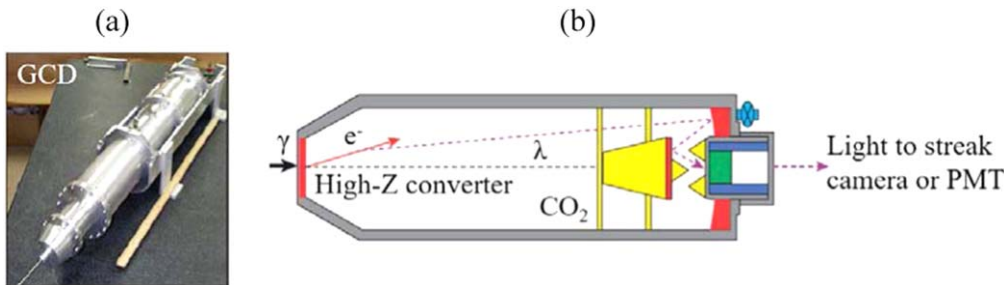

Figure 23. (a) Picture of the 1-channel gamma cherenkov detector (GCD) for measurement of the gamma-ray emission history. (b) Schematic of the GCD design and light-collection scheme.

was implemented on both OMEGA-60 and the NIF by LANL and collaborators [159]. The GCD is based on the same principle as GRH but with a different geometry and light collection scheme. The system can also be inserted inside the target chamber for maximum efficiency and measure gamma-ray emission at low yield levels [160, 161]. An example of GCD data obtained at OMEGA-60 is shown in figure 24. The latest incarnation of this system, currently known as Super GCD [162], has an energy threshold of 1.8 MeV and high sensitivity. As discussed in section 9, a GCD combined with a pulse-dilation-drift tube (PDDT) for significantly improved time response represents the next-generation system. Other media for the generation of Cherenkov light are also being explored [163].

7. Charged-particle diagnostics

In contrast to neutrons, charged particles interact electro-magnetically with the fuel, ablator and fields, and thus carry inherently more information about an ICF implosion than neutrons. As shown by equations (3.1)–(3.23), a wide variety of discrete lines and continua made up by protons, deuterons, tritons and alphas are generated, where the discrete lines are generally produced by fusion reactions and continua are caused by elastic scattering, inelastic scattering, and in-flight nuclear reactions. As discussed in section 4 and in the paper
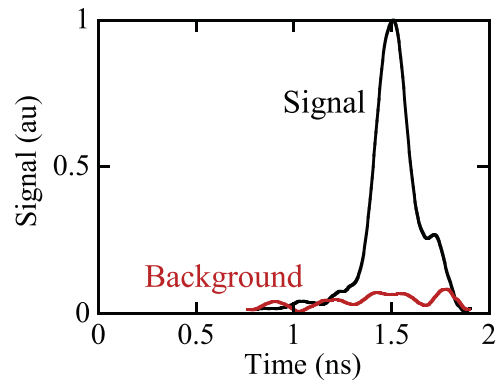
Figure 24. An example dt gamma-ray emission history measured with the GCD system on OMEGA (shot 55983). The GCD was operated with a CO_2 gas at 100 psi, which sets the threshold for generating Cherenkov light at an energy of 6.3 MeV. The background signal was obtained on another shot (shot 55989) when the GCD was operated with no gas.

by Séguin *et al* [164], yields and energy spectra of these charged particles are directly related to the properties of an ICF implosion, and specifically carry information about fusion yields, T_i, convergence, ρR, T_e, nuclear-burn history, and mix (in some specific cases). In this section, the charged-particle diagnostics used to routinely diagnose an ICF implosion are discussed.

(a)   (b)
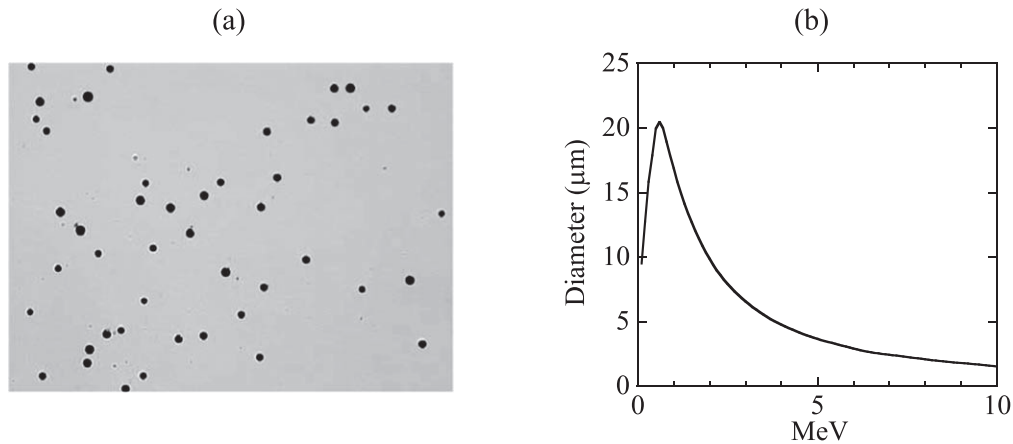
Figure 25. (a) Microscope image of proton tracks with diameters in the range of 5–10 μm, which were revealed by etching the CR-39 for 6 h at 80 °C in 6.0-Molar NaOH. These tracks were generated by protons with energies in the range of 2–4 MeV. (b) Typical proton-track diameter as function of energy for CR-39 etched for 6 h at 80 °C in 6.0-Molar NaOH. It should be noted that some variations in the diameter-versus-energy curve are often observed, depending on the quality of the CR-39.

7.1. CR-39 detectors

While neutrons interact volumetrically with the CR-39 material (see section 5.5), energetic charged particles start to interact immediately with the CR-39, resulting in a nanometer sized trail of damage at the front surface that depends on dE/dX. As discussed briefly in section 5.5, these trails are revealed by etching the CR-39 in NaOH at certain temperature and concentration (80 °C 6-Molar NaOH is commonly used). If the charged particle enters the CR-39 surface with perpendicular incidence, the etched track is round and the diameter provides information about energy and particle specie. Figure 25(a) shows an image of proton tracks with diameters in the range of 5–10 μm, and figure 25(b) shows the track diameter as a function of proton energy when the CR-39 was etched in 6.0-Molar NaOH at 80 °C for 6 h.

7.2. Wedge-range-filter (WRF) spectrometers

WRF spectrometers are compact systems that consist of a piece of CR-39 positioned behind a wedge-shaped filter [164] (see figure 26). The wedge filter, typically made of aluminum (but zirconia ceramic has also been used), disperses charged particles onto the CR-39 based on the particle-energy ranging in the filter. The combination of the wedge filter and CR-39 limits the minimum and maximum detectable charged-particle energies at a certain location on the CR-39. The reason for this is that charged particles must be energetic enough to penetrate the wedge filter but not too energetic not to be registered on the CR-39[13]. This means that at each location along the dispersion direction, there exists a narrow energy range over which charged particles are detected with 100% detection efficiency. From the diameter of a track, combined with the information about the local wedge-filter thickness, the energy of the incoming charged particle is determined. The low-energy cutoff for proton measurement is ∼4 MeV, while the high-
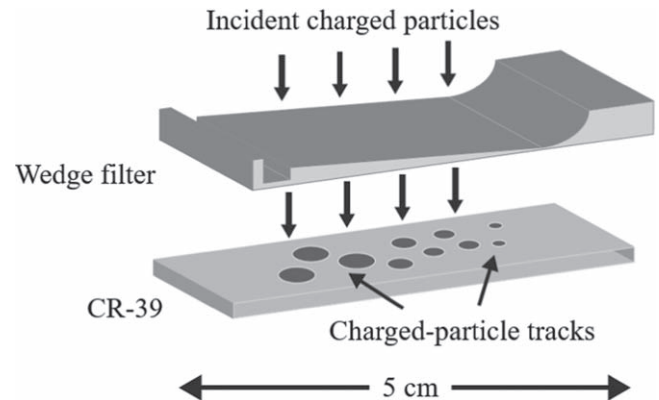

Figure 26. A schematic of the WRF spectrometer, which consists of a wedge filter on top of a piece of CR-39. Due to its compactness (∼5 cm in diameter), several spectrometers can be fielded around the implosion at close distances. See text for more details.

energy cutoff is ∼20 MeV for protons. As the minimum and maximum energies at each location behind the wedge filter are known by design and the fact that they correspond to the largest and smallest track diameters, respectively, only information about the relative shape of the CR-39 response curve is required to interpolate between these points (a typical curve is illustrated in figure 25(b)). This characteristic makes the WRF spectrometer relatively immune to piece-to-piece variations in the absolute CR-39 response to charged particles. Figure 27 illustrates the WRF spectrometers fielded inside the OMEGA and the NIF target chambers.

WRF spectrometers have been used extensively for directional measurements of primary D^{3}He-protons for studies of ρR asymmetries, fuel-shell mix, implosion dynamics, hydrodynamic equivalence and ablator burn-through in D^{3}He gas-filled implosions [165–176]; for measurements of secondary D^{3}He-protons for studies of ρR asymmetries in D$_2$ gas-filled warm, shock-ignition, fast-ignition, and cryogenically-layered implosions [79, 176–186]; and for measurements of knock-on protons produced in DT gas-filled implosions [187–189]. Given the compactness of the WRF

---

[13] If a charged particle have too high energy, the dE/dX is not high enough to create enough damage in the CR-39 to generate a track that can be made visible with the NaOH etching process.
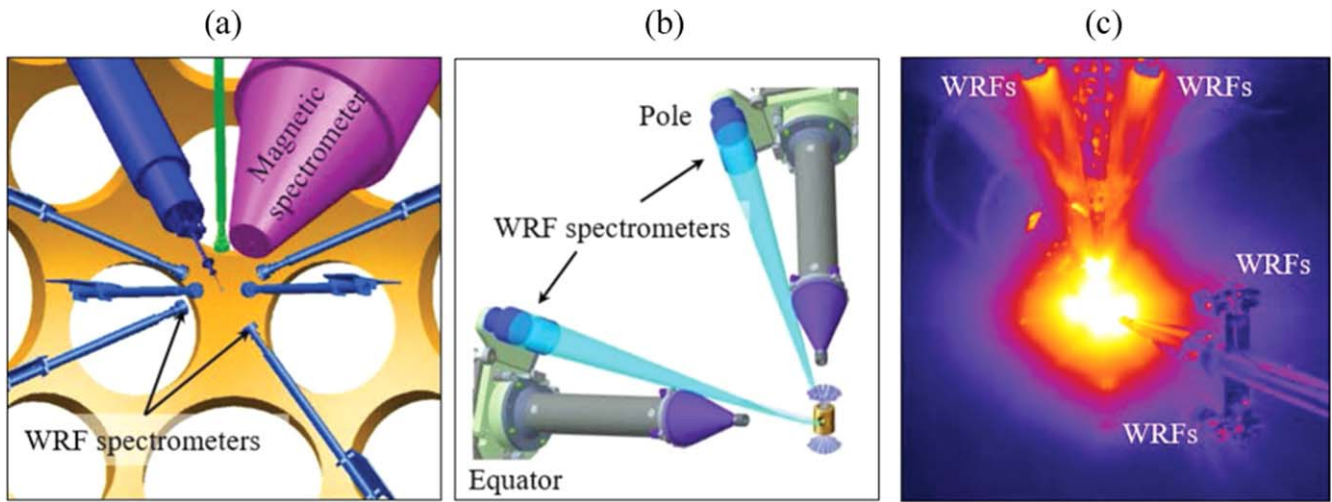
Figure 27. (a) Seven WRF spectrometers (six marked blue and one green) and a magnetic spectrometer (magenta) fielded on OMEGA. (b) Four WRF spectrometers fielded on the pole and equator on the NIF. The WRF spectrometers are mounted on the DIMs using external mounting brackets. (c) Picture of a NIF shot on which the WRF spectrometers were used on the pole and equator.
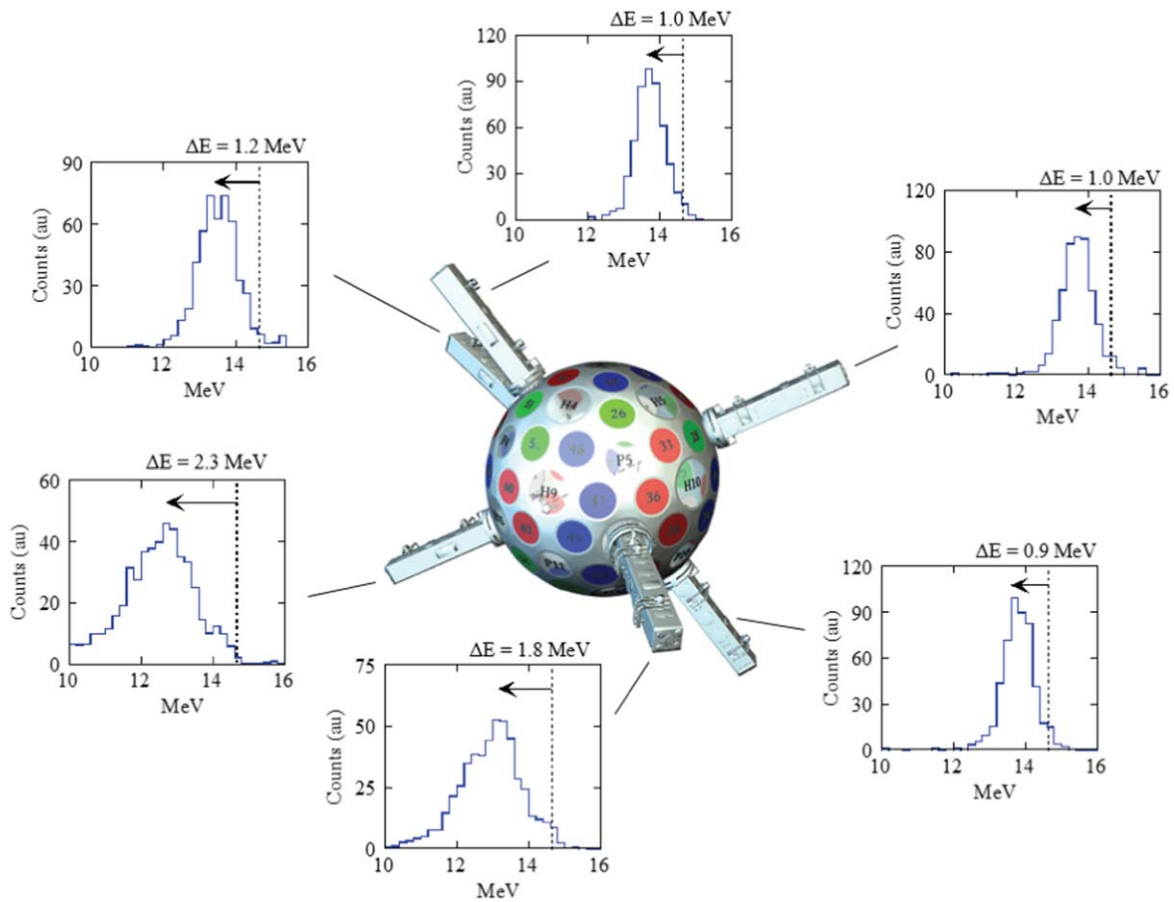
Figure 28. Primary d^3He-proton spectra measured with WRF spectrometers positioned at various locations around an OMEGA implosion (shot 21240). A 15 atm D^{3}He gas-filled CH capsule with a wall thickness of 20 μm, and sixty laser beams delivering 12 kJ in a 1 ns square pulse to the capsule were used in this experiment. The WRF spectrometers were inserted by the ten-inch manipulators (TIM, six indicated in the figure). Both the average d^3He-proton birth energy (vertical dashed line) and average energy loss measured in the different directions are indicated. The variation in the observed energy loss is substantial, indicating significant ρR asymmetries.

spectrometers, they are routinely fielded in-close and around the implosion to provide information about yield and ρR asymmetries for primary and secondary yields above 10^5 and 10^6, respectively. These systems have been essential to both basic physics studies and to the main ICF programs at OMEGA and the NIF. A few examples of WRF-measured
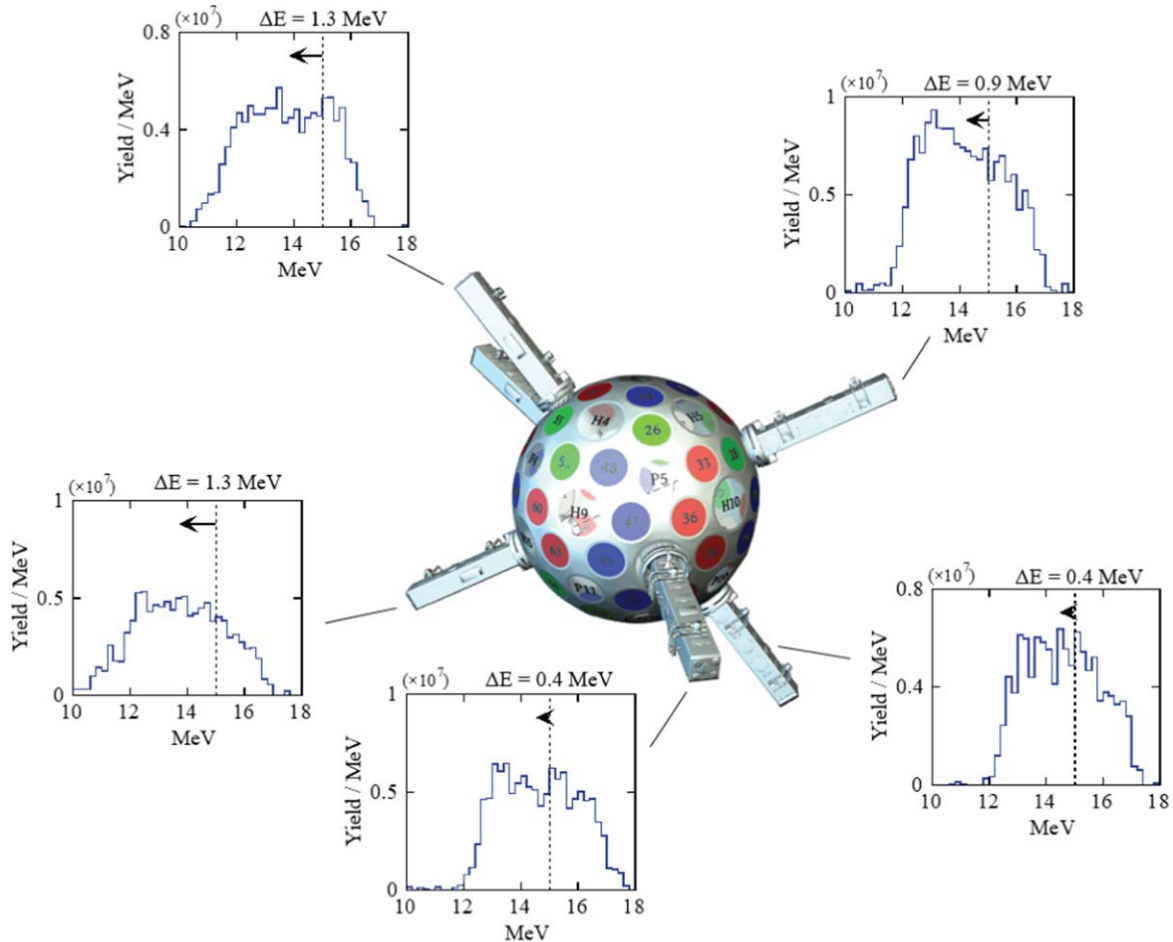
Figure 29. Secondary d^3He-proton spectra measured with WRF spectrometers positioned at various locations around an OMEGA cryogenic implosion (shot 24096). A 100 μm D_2 layer inside a 930 μm diameter GDP capsule, illuminated by sixty laser beams delivering 24 kJ in a 1.0 ns square pulse were used in this experiment. The average secondary d^3He-proton yield was 2.4×10^7 and the primary dd-neutron yield was 3.1×10^{10}. Both the average secondary d^3He-proton birth energy (vertical dashed line) and average energy loss measured in the different directions are indicated.

spectra are shown in figures 28–31. In addition, similar WRF spectrometers are now in operation at the SG-III laser in China [190, 191].

Although WRFs spectrometers are well-suited for measurements of protons, they cannot be used accurately for spectral measurements of heavier ions for a couple of reasons. The WRFs rely on charged-particle track diameter and contrast on the CR-39 for the discrimination of ion species. Though the differences in contrast and diameter are measurable between protons and heavier ions, they are subtle among heavy ions. Thus, it is difficult, if not impossible, to discern different heavy-ion species using this approach. In addition, the thin end of the wedge readily stops energetic heavy ions, thereby significantly increasing the low-energy limit for this measurement.

7.3. Magnetic spectrometers

7.3.1. The charged particle spectrometer. Magnetic spectrometers have been implemented for ICF applications at both OMEGA and the NIF, and these spectrometers use a permanent magnet to separate ions based on their gyro radius (classical)

$$r = \frac{1}{Z_i eB}\sqrt{2m_i E_i}, \qquad (7.1)$$

where Z_i is the ion-charge number, e is the elementary charge, m_i is the ion mass, and E_i is the ion kinetic energy. The magnetic Charged-Particle Spectrometers (CPS1 and CPS2), implemented on OMEGA, utilize a 7.6 kGauss permanent magnet and CR-39 detectors for momentum-dispersion and detection of different types of ions, respectively (see figure 32). As these systems are not focusing devices, a narrow and interchangeable vertical slit (width in the range of 0.1–2.0 mm) is used as an aperture to provide the required energy resolution and efficiency for different applications. These spectrometers are used routinely at OMEGA for measurements of primary and secondary charged fusion products. They also complement the WRF spectrometers in their ability to measure spectra down to a proton-equivalent energy of 100 keV for yields above 10^8. From equation (7.1), it is clear that degeneracy exists between different ions species. For example, a 1.1 MeV triton will have the same gyro radius as a 3.3 MeV proton and 3.3 MeV alpha, and
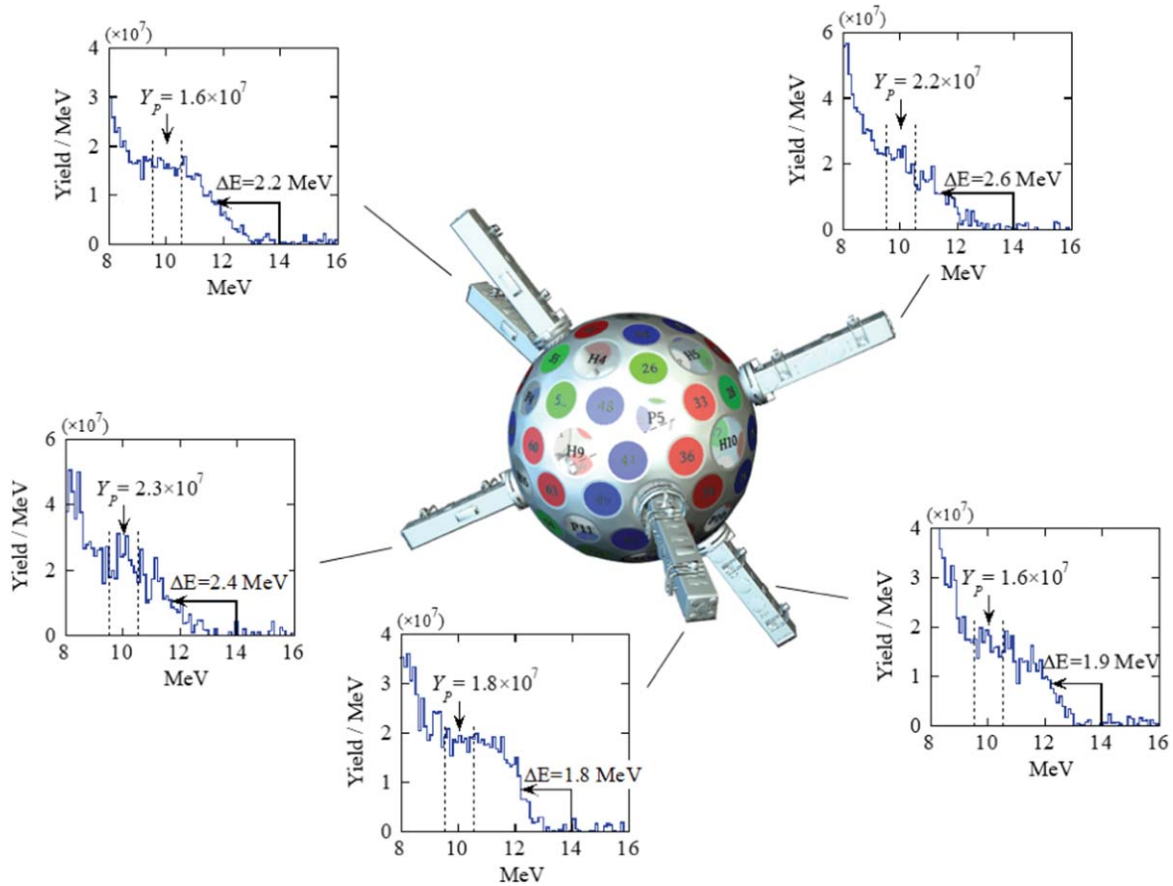
Figure 30. Knock-on proton spectra measured with WRF spectrometers positioned at different locations around an OMEGA implosion (shot 23471). A 15 atm DTH gas-filled (5% D, 5% T and 90% H) CD capsule with a wall thickness of 20 μm, and sixty laser beams delivering 24 kJ in a 1.0 ns square pulse to the capsule were used in this experiment. The average knock-on proton yield (per MeV) was 1.9×10^7 and the primary *dt*-neutron yield was 1.6×10^{11}. A ρR_{fuel} of 6.4 mg cm^{-2} was inferred from the average knock-on proton yield (in the range of 9.5–10.5 MeV), and from the average energy loss of the maximum knock-on proton energy (i.e. 14 MeV), a ρR_{shell} of 70 mg cm^{-2} was determined. The spectra observed in the different directions display a ρR_{shell} asymmetry of 25 mg cm^{-2}. The knock-on deuteron component from the CD shell is evident at proton-equivalent energies below ∼9 MeV. Reprinted from [187], with the permission of AIP Publishing.

hence end up at the same location along the dispersion plane. However, these ions can be separated based on track diameter and contrast, as illustrated figure 33. Examples of CPS-measured spectra are shown in figures 34 and 35.

CPS1 and CPS2 cannot be used for spectral measurements of heavy ions ($Z > 2$). The reason for this is that discrimination of heavy-ion species is difficult because the variation of track diameter and contrast are weak among heavy ions with different energies and charge states. On the other hand, spectral measurements of low-Z ions in the presence of heavy ions are possible because filters (made of either Mylar, aluminum or tantalum), thick enough to stop the heavy ions (e.g. carbon), are positioned in front of the CR-39 detectors.

7.3.2. The magnetic particle-time-of-flight (magPTOF) diagnostic. On the NIF, the magPTOF diagnostic has been implemented primarily for simultaneous measurements of shock-bang time and compression-bang time in D^{3}He gas-filled implosions, using d^3He-protons and *dd*-neutrons,

respectively [192]. This diagnostic, which is an extension of the pTOF diagnostic discussed in section 5.2.2, utilizes a bending magnet combined with a shielded CVD detector. It can also be used in spectrometry mode by replacing the CVD with a CR-39 detector. The diagnostic, shown in figure 36, is nominally positioned 50 cm from the implosion using a DIM.

The primary motivation for magPTOF is to reduce the large x-ray flux generated in a gas-filled hohlraum implosion, which typically overwhelms the shock-generated d^3He-proton signal. The inclusion of the thick x-ray filter in front of the CVD detector and a deflecting magnet increases the d^3He-proton signal to x-ray background about 1000×. The d^3He protons are deflected around the x-ray filter by the magnet, while the x-rays are greatly attenuated through it. An example of magPTOF data is shown in figure 37 for NIF shot N151221. As shown by the signal trace, the data is of high quality and indicates a shock-bang time of 6.7 ± 0.2 ns and a compression-bang time of 7.3 ± 0.1 ns (when the flight time and IRF have been deconvolved from the measured signal trace). This differential measurement of the shock-bang
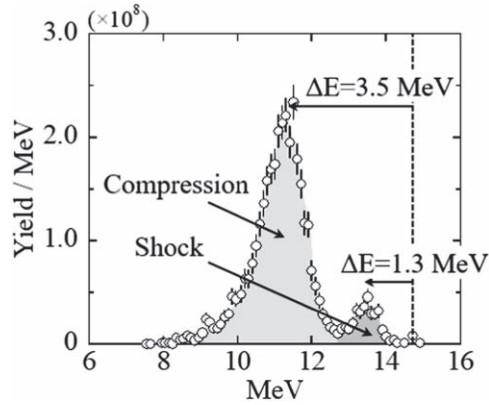
Figure 31. An example of a WRF-measured primary d^3He-proton spectrum from NIF implosion N091123. For this experiment, a 135 μm thick CH capsule filled with 10% D_2 and 90% ^{3}He was used. The spectrum displays two components, the first is a shock component where d^3He protons are generated shortly after the shock rebounds at the center of the implosion when the total ρR is relatively low. The second component is due to d^3He protons produced during the compression phase, about 400 ps after the shock phase, when the total ρR is substantially higher. Thus, the time-integrated spectrum is a mainly a reflection of the ρR time evolution (other effects such as Doppler broadening and geometrical energy-loss effects play a role when the ρR is relatively low).

and compression-bang times provides valuable additional constraints on the 1D physics of the shock propagation and shell deceleration, improving the understanding of the in-flight conditions of the fuel and shell.

7.4. Thomson parabolas (TP)

A TP utilizes the combination of electric and magnetic fields and has the advantage over magnetic spectrometers because it breaks the charge-to-mass $Z_i e/m_i$ degeneracy associated with magnetic dispersion. On the other hand, as TP requires a small pinhole as aperture to provide acceptable energy resolution, the efficiency is very low in comparison to the efficiency provided by magnetic spectrometers.

A TP system utilizes a parallel (or anti-parallel) arrangement of electric and magnetic fields, which generates discrete signal parabolas on the detector plane with constant $Z_i e/m_i$ ratios. Each position along one of these parabolas corresponds to a unique energy of the detected ion. In the case of parallel homogeneous E and B fields, the position of the charged particles with a given $Z_i e/m_i$ at the detector plane is given by

$$x \approx \frac{Z_i e E}{m_i v_i^2} L_1 (D_1 + 0.5 L_1), \quad (7.2)$$

and

$$y \approx \frac{Z_i e B}{m_i v_i} L_2 (D_2 + 0.5 L_2), \quad (7.3)$$

where e is fundamental charge, m_i is the ion mass, E and B are the electric and magnetic field strengths, respectively; L_1 and L_2 are the lengths of E-field and B-field deflection, respectively; and D_1 and D_2 are the detector distances to the

deflection regions. These expressions are valid for small deflections. The TP system thus enables simultaneous spectral measurements of a number of heavy-ions species. For this reason, two TP systems were implemented on OMEGA [193, 194].

One system, called Thomson Parabola Ion Spectrometer (TPIS) [193], was built to probe heavy ions. This system, shown in figure 38, comprises of a 400 μm diameter tantalum aperture positioned about 50 cm from the experiment, a permanent magnet, electrostatic deflector plates, and a detector assembly consisting of a piece of CR-39 and an image plate (IP). The aperture defines the energy resolution and field of view (and thus efficiency). The magnet has a 1 cm pole gap and 5.1×5.1 cm^2 pole surfaces, resulting in a uniform magnetic field of 5.3 kG. The electrostatic deflector plates are 2 cm apart, and these plates can be operated with a voltage up to 80 kV. 10×10 cm^2 sized CR-39 and a Fuji-TR IP, or a stacked assembly of both can be fielded in the diagnostic. To facilitate absolute measurements of proton spectra, the Fuji-TR-IP response to protons was determined for energies in the range of 1–8 MeV [193]. In addition, as the Fuji-TR IP does not have a protective layer of Mylar normally found on other IPs, carbon ions can also be detected while heavier ions are stopped before they can deposit energy in the active IP layer. The Fuji-TR IP is therefore ideal for measurements of energetic protons while CR-39 is more important for detecting heavier ions.

Another TP system is the Thomson Parabola Ion Energy (TPIE) analyzer [194]. This system was originally designed for studies of fast ions generated by short-pulse laser-plasma interactions at OMEGA-EP, but it has also been used for measurements of fast ions generated in ICF implosions at OMEGA. The TPIE system, shown in figure 39, uses an interchangeable square tungsten aperture with a diameter of 100 μm, 250 μm or 1 mm, an interchangeable permanent magnet with 10×5 cm^2 pole surfaces (and with either 5.6 or 8.4 kG peak field strengths), a pair of 21 cm long parallel electrodes with a 1 cm separation gap that can generate a voltage of 20 kV (total), and a detector. The detector pocket accommodates a 10×5 cm^2 piece of CR-39, an IP, or an assembly of both. An IP is needed for detection of high-energy (>10 MeV) protons, while CR-39 is needed for detection of heavy ions. As the TPIE is fielded by a TIM, the distance from the aperture to the experiment can be varied from 37 to 150 cm. In contrast to the TPIS, this flexibility, combined with the interchangeable aperture, allows for a trade-off between the energy resolution and efficiency. Examples of TPIE data are shown in figure 40.

7.5. Nuclear burn-history detectors

Both the PTD and PXTD have been used routinely for measurements of the emission history of charged fusion products. As these diagnostics are discussed in detail in section 5.3 and by Sio et al [134], further elaboration will not be made here.
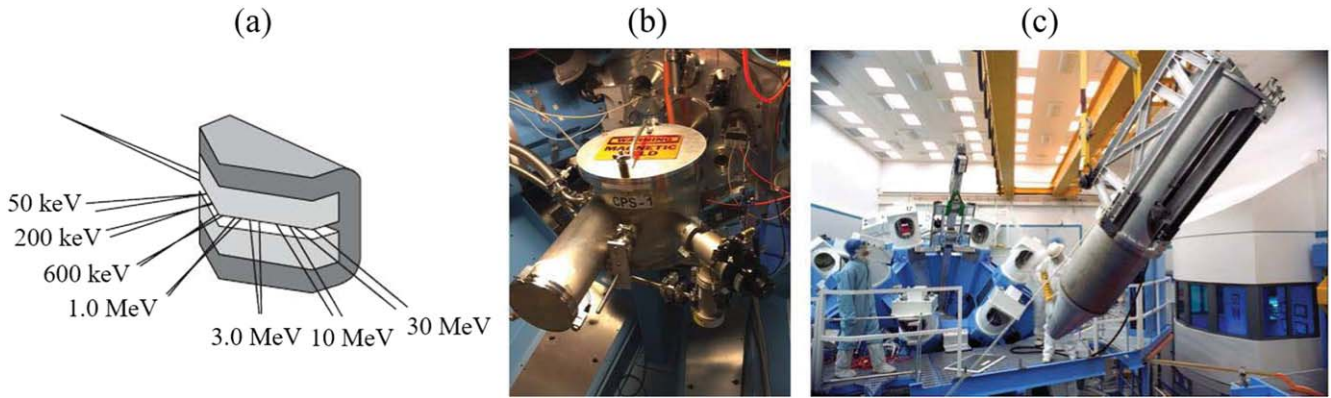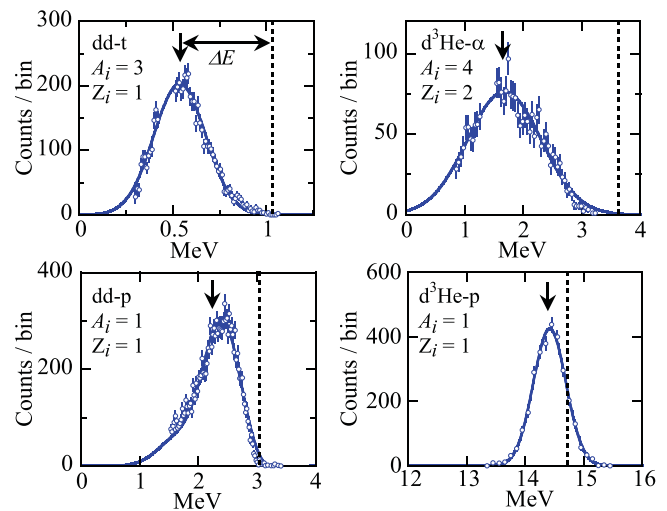
Figure 32. (a) Schematic of the charged-particle spectrometer (CPS). (b) Picture of CPS1 system (new location) on the OMEGA chamber. The magnet is inside the cylindrical vacuum chamber. (c) Picture of the shielded CPS2 system during installation. The magnet is located in front of the assembly. Both spectrometers are permanently mounted on fixed diagnostic ports on the OMEGA target chamber. The CPS1 and CPS2, which are positioned 100 cm and 235 cm from an implosion, respectively, provide close-to orthogonal views of it, thereby allowing for an assessment of yield and ρR asymmetries. Reprinted from [164], with the permission of AIP Publishing.
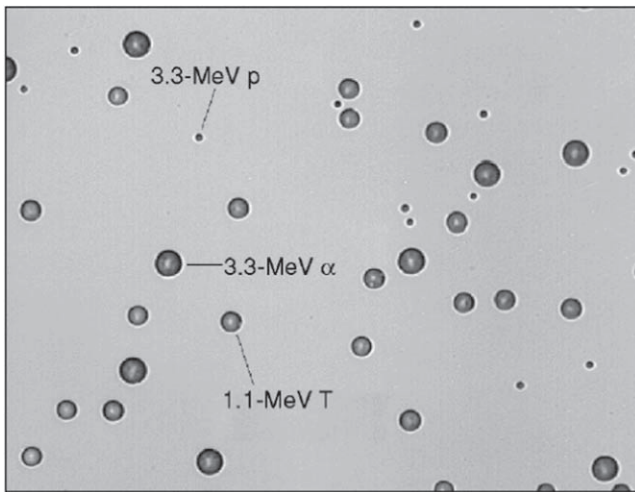
Figure 33. Microscope image of 1.1 MeV triton tracks, 3.3 MeV proton tracks, and 3.3 MeV alpha tracks recorded by the CPS2 system. These ions were generated by dd and d^3He reactions in a D^3He gas-filled, thin-glass implosion (OMEGA shot 20297). Reprinted from [164], with the permission of AIP Publishing.

Figure 34. dd-triton, d^3He-alpha, dd-proton, and d^3He-proton spectra measured simultaneously with CPS2 for OMEGA shot 75699. These fusion products are produced by the reactions shown in equations (3.5) and (3.10). The vertical arrows and dashed lines indicate measured median energy and average birth energy, respectively. Reprinted figure with permission from [73], Copyright 2019 by the American Physical Society.

7.6. Imaging systems

As discussed in section 5.4, significant efforts have been made over the last couple of decades to image dt-burn profiles using 14 MeV neutrons. During this time period, a complementary approach has been developed and used to image dd- and d^3He-burn profiles using 3.0 MeV protons and 14.7 MeV protons [196, 197], respectively. In contrast to the neutron-imaging technique that uses a long and tapered pinhole (and/or penumbral aperture), this charged-particle-imaging technique is performed with a penumbral imaging system that is based on a thin aperture. In addition to the thin aperture, which is significantly larger than the size of the dd- and d^3He-burn profiles, this system consists of CR-39 detectors that are separated by ranging filters for detection of the different charged fusion products (see figure 41). As the

aperture is larger than the dd- and d^3He-burn profiles, all information about the burn region is encoded in the penumbra of the image, which must be post-processed with special inversion algorithms that reconstruct the burn distributions. Up to three imaging systems can be fielded on OMEGA using TIMs with nearly orthogonal view of the implosion, as illustrated in figure 42.

Figure 43 illustrates a set of images of the d^3He-proton surface-brightness observed in the three directions, as indicated in figure 42(b), for an intentionally asymmetrically-driven implosion with a symmetry axis around the view-1 axis. For more in-depth discussion about this type of measurement, the reader is referred to [86, 198, 199].
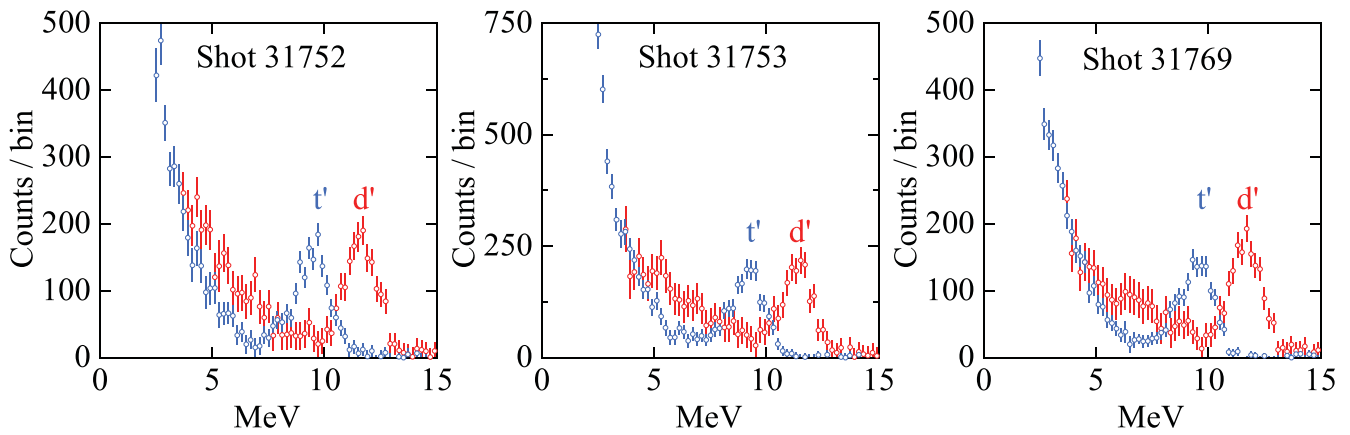
Figure 35. Knock-on deuteron (d') and triton (t') spectra measured simultaneously with CPS2 for three OMEGA shots. These spectra were generated by 14 MeV dt neutrons elastically scattered off fuel ions (equations (3.13) and (3.14)) in DT gas-filled, thin-glass implosions. The broadening of the spectra is mainly due to Doppler broadening and CPS-spectrometer response. Adapted figure with permission from [63], Copyright 2011 by the American Physical Society.
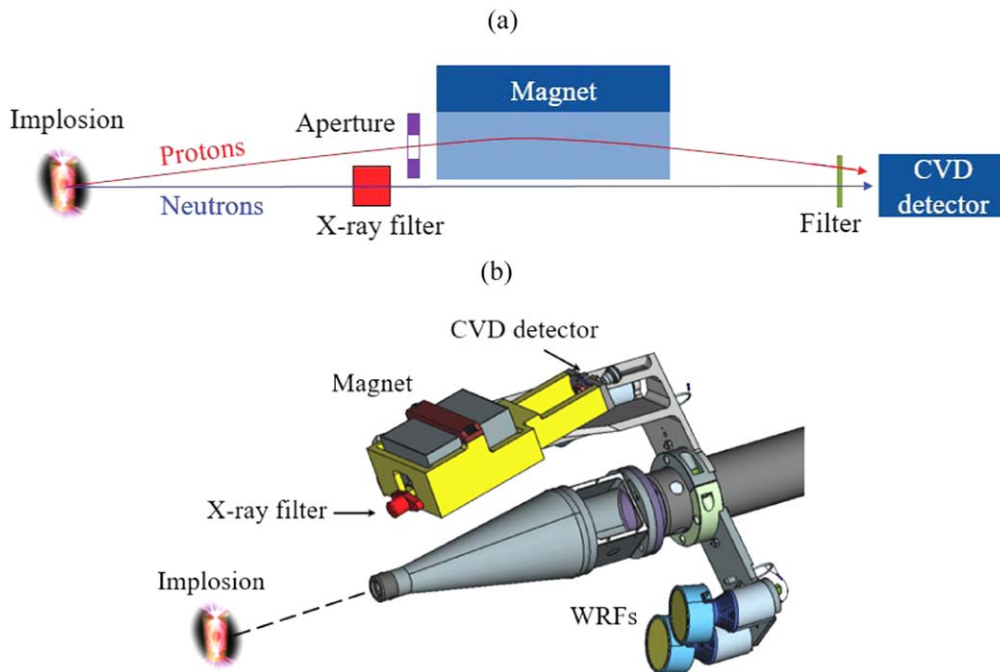
Figure 36. The magPTOF on the NIF. (a) A schematic of the magPTOF main components. The x-ray filter blocks the CVD detector from x-rays coming directly from the implosion, while the d^3He-protons are deflected around it. (b) A CAD drawing of the magPTOF and WRF spectrometers attached to a snout inserted by a DIM.

7.7. Mono-energetic charged-particle radiography

The use of quasi-mono-energetic charged particles, from primary fusion reactions, to radiograph ICF-relevant plasmas has opened a new window to, and provided several profound insights about, the physics governing ICF-relevant plasmas [88, 89, 91, 92, 200–221]. In contrast to x-rays, which have been used for decades to radiograph plasma-density distributions, charged particles are sensitive to both matter and electromagnetic fields, where the latter is the physics of main interest in most radiography experiments. To interrogate the electromagnetic fields in an ICF-relevant plasma, a point-projection backlighter that produces primary fusion products

is typically used in combination with a CR-39 detector[14]. The backlighter is generally positioned $\sim$1 cm from the subject and the CR-39 detector is positioned on the other side of the subject $\sim$30 cm away, resulting in a magnification of $\sim$30. In addition, a mesh is used in some experiments, and this mesh is positioned in front of the detector package. A schematic of the experimental configuration for a charged-particle-radiography experiment is shown in figure 44.

The backlighter consists typically of a thin-glass capsule (outer diameter of $\sim$420 μm and wall thickness of $\sim$2 μm) filled with equimolar D^3He gas (total pressure of 18 atm).

---

[14] IPs are used in some experiments.
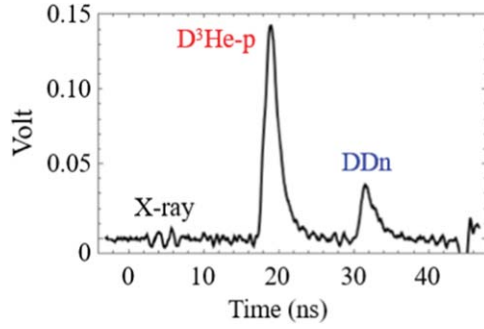
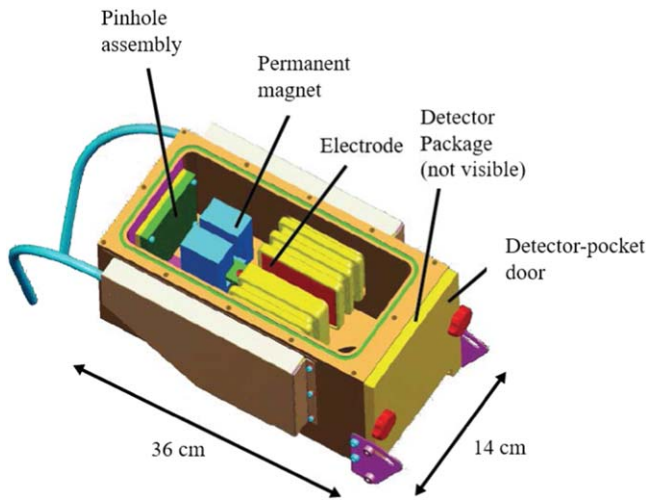**Figure 37.** MagPTOF data for shot N151221. After the IRF and particle flight times have been corrected for, a shock-bang and compression-bang time of 6.7 ± 0.2 ns and 7.3 ± 0.1 ns were determined, respectively, indicating a time difference of 0.6 ns.
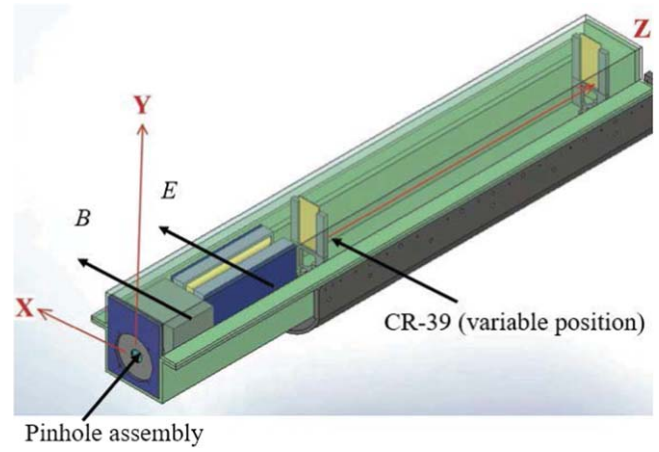

Figure 38. A cutaway view of TPIS, which includes a pinhole aperture, permanent magnet (blue), electrodes (red), and detector pocket. The outer dimensions of the diagnostic are also indicated. Reprinted from [195], with the permission of AIP Publishing.

This capsule is illuminated by $\sim$20 non-smoothed laser beams, delivering $\sim$9 kJ to the capsule in a 1 ns square pulse. This allows for the other 40 laser beams to be used for the actual experiment. The D^{3}He gas in the backlighter is shock-heated and compressed to T_i of $\sim$10 keV and number densities of order 10^{23} cm^{-3}, which generates $\sim$10^9 and $\sim$10^{10} d^3He and dd reactions, respectively, over a burn duration in the range if 100–150 ps and burn volume (source size) with a diameter of order 50 μm.

As the Lorentz force causes charged-particle deflections, information about the path-integrated electromagnetic fields in the subject plasma is contained in the charged-particle spatial fluence variations at the detector plane. Given the mono-energetic nature of the charged-particle backlighter, there is a direct correlation between the deflection angle and path-integrated E and B fields as described by

$$\theta_B = \frac{Z_i e}{\sqrt{2 m_i E_i}} \int B_\perp \, dl, \qquad (7.4)$$

Figure 39. A cutaway view of TPIE, which includes a pinhole assembly, permanent magnet (blue), electrodes (yellow), and a CR-39 detector. The diagnostic is fielded using a TIM. Reprinted from [194], with the permission of AIP Publishing.
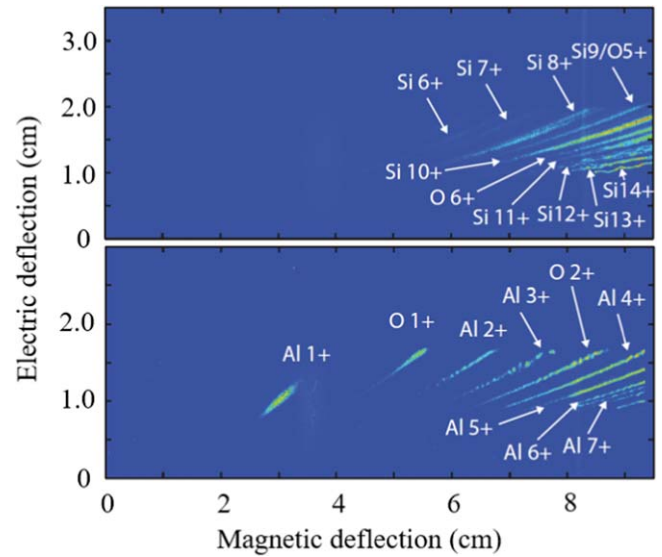
Figure 40. An example of TPIE data obtained from two ICF implosions at OMEGA. (Top image) TPIE data from a thin-glass implosion (shot 64685), and (bottom image) from an aluminum flash-coated, CD-capsule implosion (shot 65273). The ion track density is represented by a color value. Several lines of highly ionized silicon and oxygen ions are observed from the thin-glass capsule implosion, and several lines of ionized aluminum and oxygen ions are observed from the flash-coated CD-capsule implosion. These data were obtained by operating the TPIE with a piece of CR-39 as detector and peak magnetic and electric fields of 5.4 kG and 2.8 kV cm^{-1}, respectively.

and

$$\theta_E = \frac{Z_i e}{2 E_i} \int E_\perp \, dl, \qquad (7.5)$$

where Z_i is the ion-charge number, e is the elementary charge, m_i is the ion mass, and E_i is the ion kinetic energy. $B_\perp$ and $E_\perp$ are the magnetic and electric fields perpendicular to the charged-particle trajectory. From these two equations, it is clear that the effect of both E and B fields can be determined
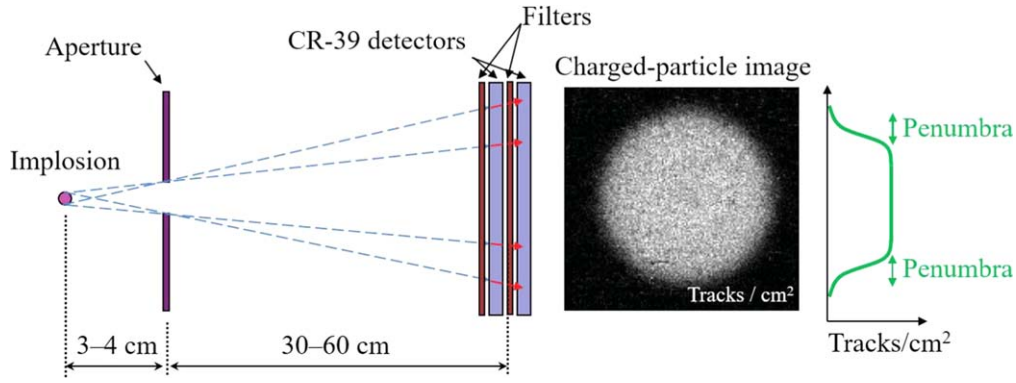
Figure 41. A schematic drawing of the charged-particle imaging system. With an aperture of $\sim$2000 μm that is significantly larger than the burn region, information about the source exists in the penumbra. The surface brightness of the charged-particle emission is reconstructed from the measured image shown to the right.

Figure 42. (a) A drawing of the charged-particle imaging system that is used to primarily measure the dd and d^3He burn regions. The CR-39 detector (separated from the system in this figure) can be positioned at three different slots at different distances for different magnification. (b) Cutaway view of the OMEGA-target chamber, showing three imaging systems pointed toward the implosion (located at the center of the chamber). The blue structure holds the capsule. Adapted from [196], with the permission of AIP Publishing.
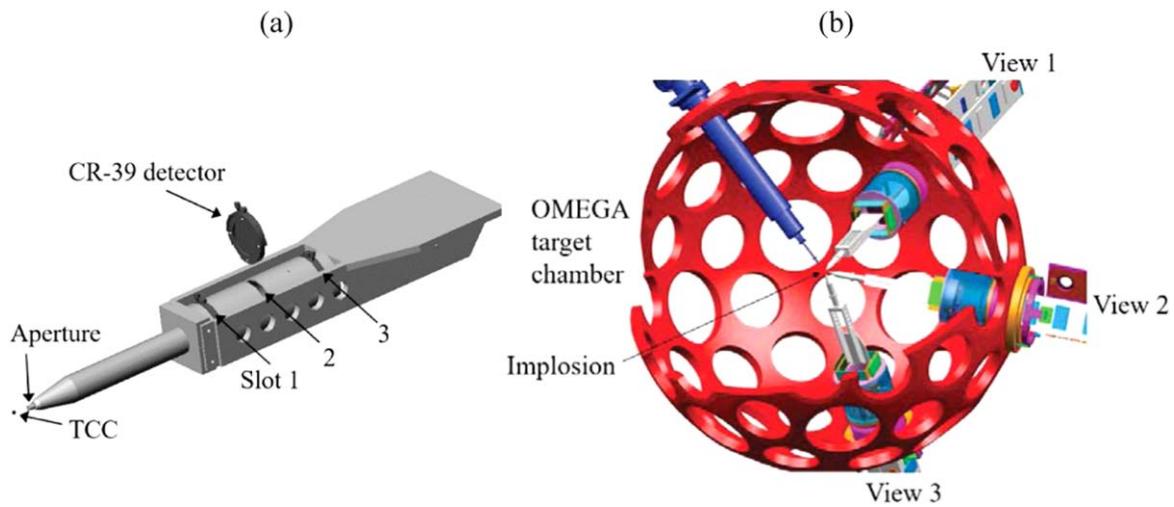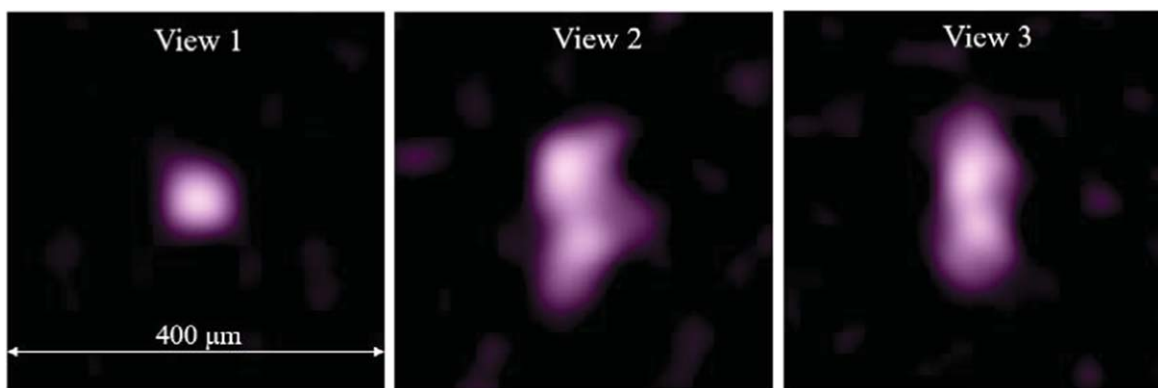

Figure 43. Three d^3He-proton surface-brightness images observed in three nearly orthogonal directions. These images were obtained from a D^{3}He gas-filled CH-capsule implosion (OMEGA shot 35172), which was asymmetrically driven (with a symmetry axis parallel with View 1).

from radiographs of, for instance, 3 MeV dd-protons and 14.7 MeV d^3He-protons. To extract this information from the radiographs, a fundamental understanding of the spectral, temporal, and emission characteristics of the charged particles emitted from the backlighter must be obtained. An

understanding of how the finite source size, scattering in the plasma subject, and scattering in the detector impact the radiograph must also be obtained. By design, the latter two are insignificant and can be ignored, which means that the spatial resolution is limited by the charged-particle source
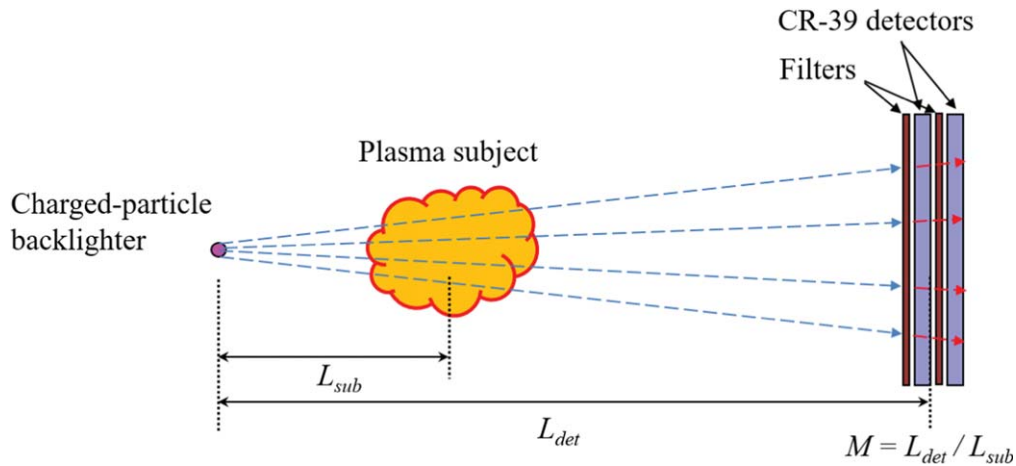
Figure 44. Schematic of the charged-particle radiography measurement. The backlighter generates quasi-mono-energetic charged particles that are used to radiograph a plasma subject. A package of CR-39 detectors, properly filtered for the different charged particles, is used for detection of these particles. Most experiments to date have utilized 3 MeV dd-protons and 14.7 MeV d^3He-protons, in which two pieces of CR-39 were fielded, where each one was filtered to optimally detect these particles. As discussed in section 9.3, advances are being made to this platform, where three charged particles will be used simultaneously to radiograph a plasma subject.

size. Examples of charged-particle radiographs are shown in figures.

8. Radiochemical diagnostics

Two types of radiochemical diagnostics are being used routinely to support the ICF program at the NIF. These are the radiochemical analysis of gaseous samples (RAGS) system [222] and solid radiochemistry collector (SRC) [223, 224], which are both used to measure nuclear reactions between neutrons or charged particles, emitted from an implosion, and a particular type of nuclei implanted in either the capsule or hohlraum. After an implosion, the resultant radioactive gas or solid debris are collected from the NIF target chamber and analyzed via radiation detection or mass spectrometry to determine the number of reaction products produced in the implosion or hohlraum (mass spectrometry is used to analyze non-radioactive isotopes). Essential to both techniques is to have a clear understanding of the spatial distribution of the implanted ions with respect to the source and flux distributions of the neutrons or charged particles. The reason for this is that the number of reaction products depends strongly on these distributions, as well as on the spectrum and reaction cross sections.

These radiochemical methods are being used to diagnose the ratios of radioactive isotopes generated by charged particles and neutrons at lower energies and 14 MeV, and from these ratios a spatially-averaged fuel ρR can be determined.

8.1. System for RAGS

The hardware for RAGS consists of a pre-filter that removes water vapor, particulates and reactive gases, and a cryogenic noble gas-collection system (see figure 45). The RAGS was designed to collect and analyze activated gases produced in the implosion. After an implosion, the activated gases in the target chamber are pumped out by a series of turbo pumps and

directed to the first stage of RAGS where water vapor, unwanted species and reactive gases are filtered out from the gas. This procedure generates a noble-gas fraction for additional purification. The RAGS is typically set to collect xenon or a combination of xenon and krypton. This selection is done by adjusting the temperature in a cryo trap. Radioactive isotopes are first analyzed using high-purity germanium gamma-ray spectrometer, and isotopes with half-lives as short as eight seconds can be measured [225]. The gases are subsequently transferred to a removable sample bottle where they are frozen and analyzed with gamma-ray or noble-gas-mass spectroscopy. To determine the total number of radioactive nuclei in the gas that were generated by the implosion, the RAGS efficiency for collecting reaction products from the target chamber must be determined. This is done in a three-step process. First, a small but known amount of either stable or radioactive tracer gas is injected into the NIF target chamber directly after a shot. Second, the gaseous products are pumped out and into the RAGS system. From the collected gas, the efficiency is determined by comparing the number of injected tracer atoms to the number of radioactive isotopes produced by the implosion. The collection and analysis of the gas is conducted with efficiencies in the range of 80%–100%.

An example of a RAGS application is when ^{127}I and ^{124}Xe are implanted into the capsule ablator. From ^{127}I(d, $2n$)^{127}Xe and ^{124}Xe(n, $2n$)^{123}Xe reactions, the ratio of the xenon isotopes in the collected gas provides information about fuel-ablator mix. The challenge with this kind of measurement is to estimate the level of mix in an implosion. The reason for this is that an absolute calibration of the collection efficiency of the different isotopes is required.

8.2. Solid radiochemistry collector

The SRC diagnostic is used primarily to collect solid debris produced by an implosion. Two SRC designs were initially

Figure 45. The RAGS hardware at the NIF. Directly after a shot, the gaseous products inside the target chamber are pumped out and into RAGS, where unwanted species are filtered out from the gas (this happen in the right cart shown in the figure). The noble gases are subsequently frozen and analyzed to quantify the number of nuclear reactions that occurred in an implosion. This happens in the left cart shown in the figure. Reprinted from [222], with the permission of AIP Publishing.

Figure 46. (a) Pictures of the SRC systems. (a) The SRC with a 2 inch diameter disc of either tantalum, vanadium or carbon. Up to four SRC systems can be fielded on one DIM. Reprinted from [224], with the permission of AIP Publishing. (b) The Vast Area Detector for Experimental Radiochemistry (VADER) system for solid radiochemistry collection.

implemented. The first design consists of a 2 inch diameter disc of either tantalum, vanadium or carbon. This disc is mounted in the same holder as used for a WRF spectrometer, discussed in section 7.2, and up to four of them can be mounted on a DIM about 50 cm from an implosion (figure 46(a)) [226]. The second design consists of a large-area detector, called Vast Area Detector for Experimental Radiochemistry (VADER) [223] (figure 46(b)), and this design has a six times larger solid angle than the standard 2 inch-disc design. After an implosion, the SRC discs or VADER are removed for analysis using gamma-ray spectroscopy. Depending on the application, the SRC samples may be first processed chemically to separate the material of interest from interfering background products.

The SRC system has routinely been used to collect activated gold debris from the holhraum. When the gold is exposed to the ICF neutron spectrum at the NIF (see typical spectra in (figures 1 and 21(b))), different gold isotopes are generated by the ^{197}Au$(n, n'\gamma)^{198}$Au and ^{197}Au$(n, 2n)^{196}$Au reactions. As the $(n, n'\gamma)$ cross section dominates the $(n, 2n)$ cross section at lower energies, and vice-versa at 14 MeV, the ratio of the two gold isotopes provides relative information of the spatially-averaged fuel ρR in an implosion. For an absolute determination of the ρR, the SRC-gold data is cross-referenced to the dsr data obtained by the down-scattered-neutron method (see figure 47).

9. Next-generation nuclear diagnostics

Since the initiation of the experimental ICF program in the 70s, substantial progress has been made, facilitated in part by the innovation and development of novel nuclear diagnostics that provided new and unprecedented measurements. Higher
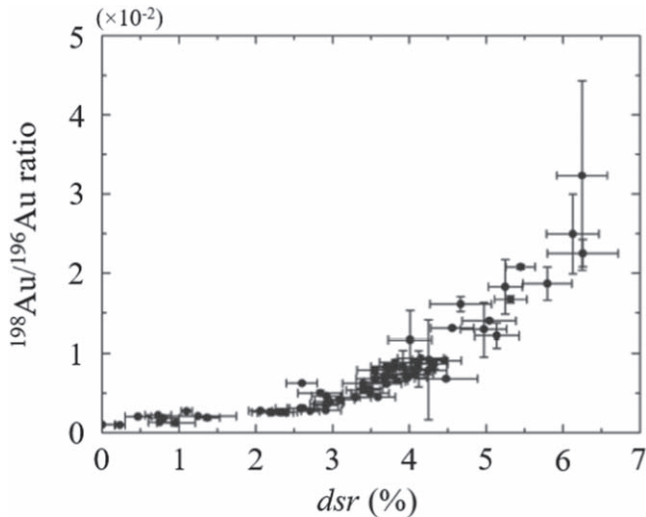
Figure 47. ^{198}Au/^{196}Au ratio determined from gamma-ray spectroscopy of the resultant debris collected by the SRC on several DT cryogenic implosions at the NIF (each data point represents one implosion). The ^{198}Au is produced by ^{197}Au$(n, \gamma)^{198}$Au induced by low-energy neutrons, which are generated single and multiple scatter in the fuel, and the ^{196}Au is produced by ^{197}Au$(n, 2n)^{196}$Au reactions that are induced by 14 MeV neutrons. Reproduced from [118]. © IOP Publishing Ltd. All rights reserved.

fusion yields have also enabled higher-quality measurements with improved spatial, temporal or spectral information. The ability to gather more data in a single implosion experiment has also facilitated an increased level of understanding about the physics governing the nuclear phase of an ICF implosion. With the implementation of high-fusion-yield facilities worldwide, such as the NIF, LMJ, UFL-2M and SG-IV facilities, the next-generation nuclear diagnostics will play an even more important role for decades to come. In this section, we discuss today's perspective on them.

9.1. Neutron diagnostics

9.1.1. Real-time neutron activation diagnostics.
As discussed in section 5.1.2, the zirconium NADs positioned around an implosion at the NIF are used to measure the directional yield of unscattered neutrons emitted from a high-ρR implosion. From this type of data, a fluence (and ρR) map with asymmetry modes up to $L = 2$ can be reconstructed. However, the number of NADs has been insufficient to characterize asymmetries with modes larger than $L = 2$. To address this issue, 48 real-time nuclear activation diagnostics (RT-NADs) are currently being implemented at various locations on the NIF chamber. A key-feature of this system is that it operates without depending on manual retrieval and off-line analysis of the RT-NAD activation.

Each RT-NAD consists of a zirconium disc, with a mass of about 400 g, a lanthanum-bromide-scintillator crystal coupled to a photomultiplier, and a compact gamma-ray spectrometer, which is used to record 909 keV gamma-rays from the activated ^{89}Zr. The light generated in the crystal is converted to an electronic signal that is amplified and

analyzed by the gamma-ray spectrometer. The times of arrival and pulse-height are recorded by a digitizer. Subsequently, data-analysis routines are used to determine the characteristic gamma-ray events from the ^{89}Zr. As the rate of ^{89}Zr events is decaying with a 3.2 d half-life, the total number of neutrons incident on that detector from a particular shot is determined by extrapolating back to the time of the shot. For more detailed information about the RT-NADs, the reader is referred to [227, 228].

9.1.2. Cherenkov-based nTOF spectrometers.
As discussed in section 5.2, nTOF spectrometers are being used to routinely measure the 0th moment (yield), 1st moment (hot-spot velocity), and 2nd moment (spectral broadening) of the dt-neutron spectrum. This has been done by recording neutron arrival times along different LOS using a scintillator coupled to a PMT. Recently, it has become clear that more precise measurements of the different spectral moments, than provided by standard nTOFs, are required. As typical hot-spot flow velocities in NIF implosions are ~ 50 km s^{-1}, measurement of the 1st moment in dt-neutron spectrum must be conducted to an accuracy much better than 0.1%. With an nTOF spectrometer positioned about 20 m from the implosion, this translates to a temporal precision of much better than 30 ps. To achieve this, the timing of the nTOF signal trace relative to the neutron production time must be extremely well known (equation (5.4)). The IRF also needs be narrow and known accurately.

A new and exciting effort is under way within the ICF program in the US to implement Cherenkov-based nTOF spectrometers that will meet these requirements [229–231]. The technique is based on Cherenkov radiation generated by $(n, n'\gamma)$ reactions in fused silica followed by Compton scatter and pair production. Several prototype systems have been built and implemented recently on the NIF and OMEGA, and the first set of tests look very promising. The nuclear excitations and subsequent Cherenkov radiation generate a signal that is significantly shorter than the decay time of scintillator decay times. As the fused silica is sensitive to implosion (and hohlraum) gamma-rays, which are not affected by Doppler shifts, an accurate gamma-ray measurement of t can also be made simultaneously with the neutron measurement. Concerns about the detection efficiency still remain to be addressed for certain applications.

9.1.3. Three-dimensional neutron imaging.
Diagnosing the 3D morphology of the nuclear burn and surrounding high-density fuel with high spatial resolution is essential to constructing an adequate picture of the assembled hot-spot and surrounding high-density fuel-shell. To that end, a 3D neutron-imaging system for imaging both primary and down-scattered neutrons is currently being implemented at the NIF. The system will view the implosion along three close-to orthogonal LOS [232], which simplifies the reconstruction of an asymmetric implosion. Similar to the existing systems, these neutron-imaging systems consist of an array of pinholes and penumbral apertures, a scintillator-based detector with
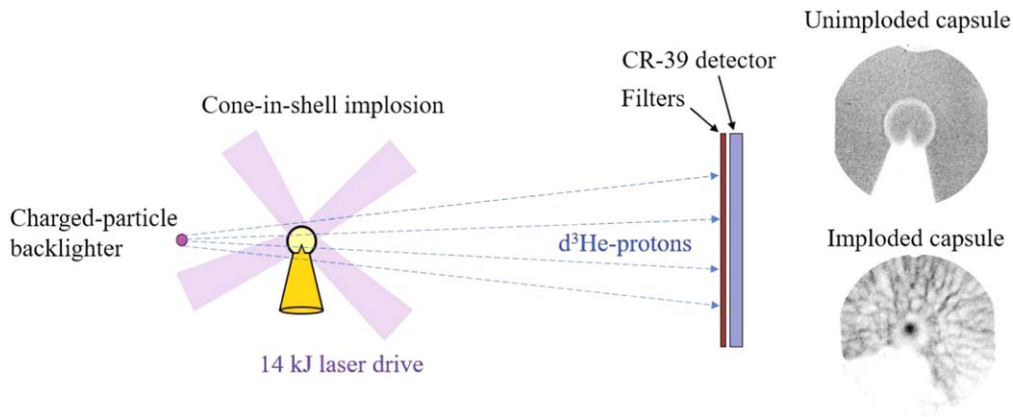
Figure 48. (Left) Schematic of the experimental setup for radiographing a cone-in shell implosion. For this measurement, a quasi-isotropic emission of $\sim 3 \times 10^8$ d^3He-protons from the backlighter was used. These protons had a spectral linewidth of less than 3%, and they were produced over a time duration of 130 ps. (Right) Fluence radiographs of an unimploded cone-in shell capsule (shot 46531) and an imploded cone-in shell capsule (shot 46529). The dark areas in the radiographs correspond to regions of higher proton fluence. From these radiographs, details of the path-integrated field distributions surrounding the capsule can be determined. From [202]. Adapted with permission from AAAS.

gated cameras to collect two timed images, one for 14 MeV neutrons and one for down-scattered neutrons.

Using three orthogonal images of both primary and down-scattered neutrons, analysis methods are currently being developed to generate a 3D picture of the burn region, surrounding high-density fuel-shell, and remaining ablator [233–235].

9.1.4. Time-resolving neutron spectrometry. Current neutron spectrometers are used routinely to measure the time-integrated neutron spectrum, from which burn-averaged values of ρR, Y_n, and apparent T_i are determined, as discussed in sections 5.2 and 5.6. Although these data have been essential in guiding our understanding of the physics governing the nuclear phase of an ICF implosion, the current suite of spectrometers does not provide any information about the evolution of the fuel assembly, hot-spot formation, alpha heating, and nuclear burn. This information will be obtained with the next-generation MRS for time-resolved measurements of the neutron spectrum. The plan with this system is to measure the spectrum in the range of 12–16 MeV with high accuracy (<5%), energy resolution ($\sim$300 keV) and, for the first time, time resolution ($\sim$30–40 ps). The system is called MRSt that is based on the existing MRS principle and PDDT technology [236, 237]. Current point-design includes a 40 μm thick, 400 μm diameter CD foil positioned on the outside of a hohlraum for production of recoil deuterons from incident neutrons [238]; two dipoles and three quadrupoles, positioned outside the NIF target chamber for energy analysis and focusing of forward-scattered recoil deuterons onto a short focal plane of the spectrometer; and a PDDT with a CsI photocathode positioned at the focal plane. In the CsI photocathode, the recoil deuterons generate secondary electrons, which are subsequently accelerated by a spatially- and time-varying electric field that unskews and stretches the signal over a distance of $\sim$1 m. This signal is subsequently amplified by an MCPs and detected by an array of anodes. By dilating the pulse about 10–20 times, fast temporal features (of order 10 ps) can be recorded and analyzed

with standard acquisition systems. Shielding will surround the detector system for suppression of the ambient background of neutrons and gamma-rays [239].

9.2. Gamma-ray diagnostics

9.2.1. Three-dimensional gamma-ray imaging. The 3D neutron imaging system on the NIF is also being developed with 4.44 MeV gamma-ray imaging in mind [234, 240]. With an additional time gate, imaging of gamma-rays can also be done. This data would provide 3D information about the location of the CH (or HDC) ablator and ablator mix into the *dt* fuel.

9.2.2. Gamma-ray emission-history diagnostic. The current GCD system has been used at both OMEGA and the NIF for measurements of the nuclear burn history using *dt* gamma-rays (equation (3.2)) or the ablator-ρR evolution using 4.44 MeV gamma-rays from the ^{12}C(n, $n\gamma$) reaction (equation (3.17)). With a standard PMT on the backend of this diagnostic, the time resolution was limited to >100 ps, which prompted an upgrade of the system by incorporating the PDDT technology. The first phase of the project involved the installation of the GCD into an insertion-well at a position of 3.9 m from the implosion [155]. The second phase involved the incorporation of the PDDT technology to improve the time resolution to $\sim$10 ps [241, 242], and tests of the GCD-PDDT performance [242].

9.2.3. Gamma-ray spectroscopy. High-resolution gamma-ray spectroscopy is a nuclear technique that has not been well-utilized for ICF-diagnostic applications. The reason for this is that the gamma-ray yields produced by the relevant nuclear reactions are extremely low, orders of magnitude lower than the main reaction branches (see equations (3.1)–(3.7) and
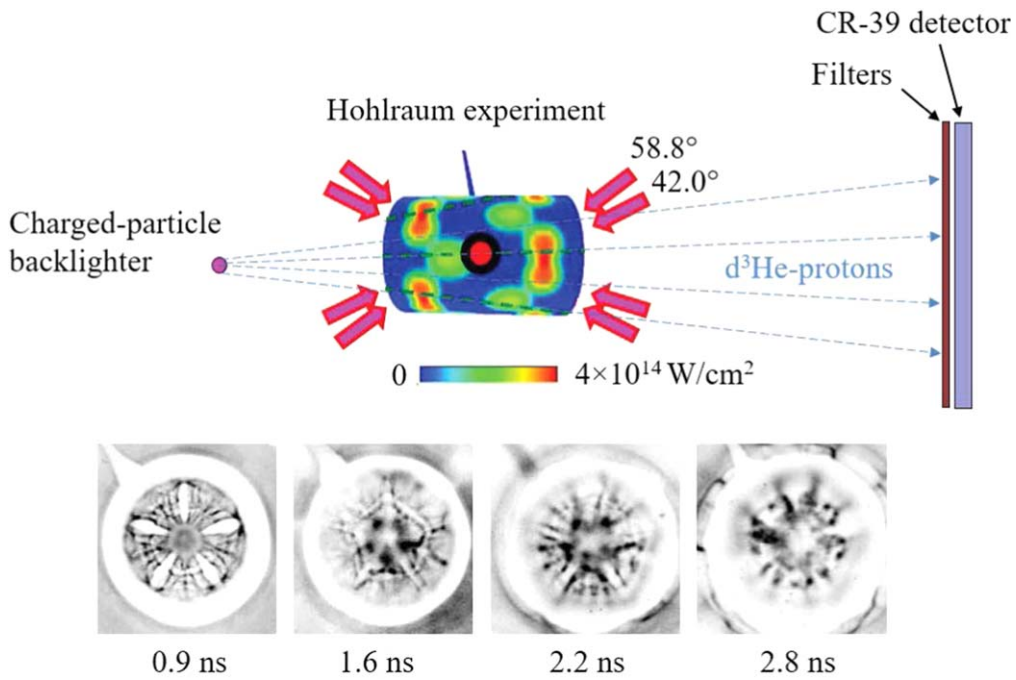
Figure 49. (Top) Schematic of the experimental setup for radiographing an indirect-drive implosion. For this experiment, five and ten laser beams that entered each end of the hohlraum with incident angles of 42° and 58.8° were used, respectively. The colors on the hohlraum wall illustrate the laser-intensity distribution. In this particular experiment, the charged-particle backlighter was driven by thirty laser beams, which delivered a laser energy of ~11 kJ in a 1 ns square pulse. The backlighter produced d^3He-protons that were used to backlight the holhraum. (Bottom) d^3He-proton-fluence radiographs recorded at different times of the indirect-drive implosion (each image represents one implosion). The dark areas in the radiographs correspond to regions of higher proton fluence. From these radiographs, the path-integrated field distributions can be determined. From [206]. Adapted with permission from AAAS.
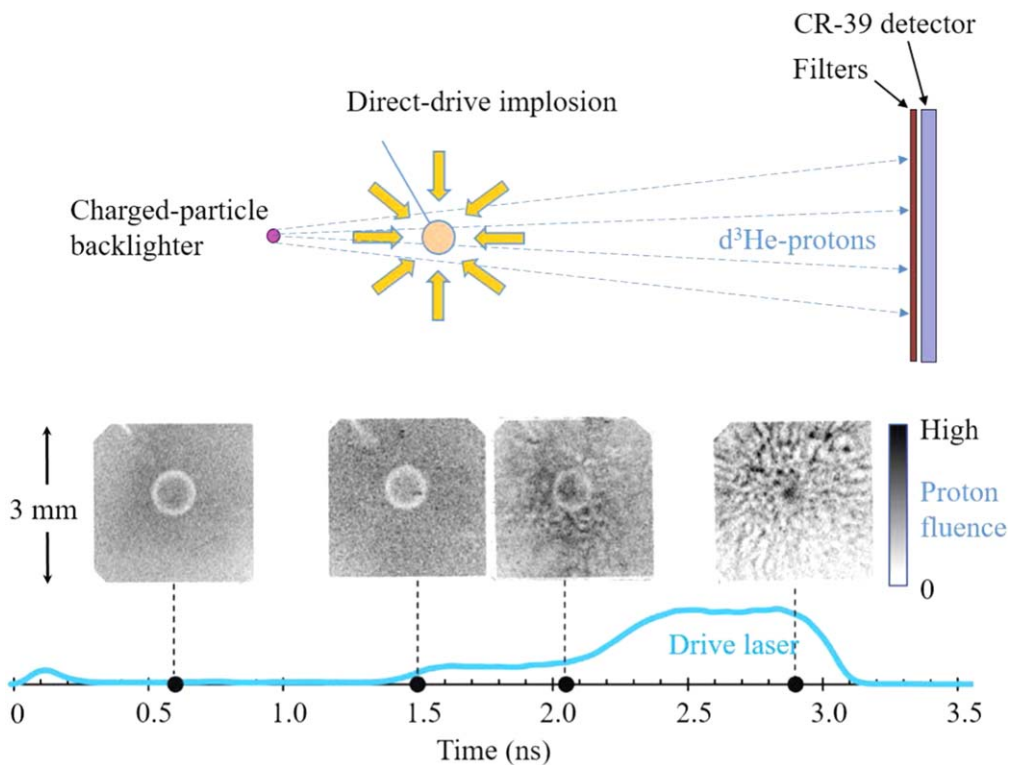
Figure 50. (Top) Schematic of the experimental setup for radiographing a direct-drive implosion. In this experiment, a series of 850 μm diameter CH capsules (with a 35 μm wall thickness), filled with 15 am of H_2 gas, were backlit by d^3He-protons. These CH capsules were driven with a subset of laser beams, delivered in a shaped pulse (OMEGA type RD1501p, which is shown at the bottom of the figure). From left to right, the images are from OMEGA shots 51244, 51246, 51247, and 51250. Adapted from [209], with the permission of AIP Publishing.

(3.10)–(3.11)), which put stringent requirements on the efficiency and resolution.

In addition to the *dt*-fusion gamma-rays and 4.44 MeV gamma-rays from the $^{12}C(n, n\gamma)$ reaction, there is a large range of gamma-rays that can be used to diagnose an ICF implosion. To that end, a high-efficiency, high-resolution gamma-ray spectrometer would open up a window for exploring new physics in an ICF experiment. With adequate efficiency and energy resolution, the 15.58 MeV gamma-rays from the $^{2}H(n, \gamma)^{3}H$ reaction can be used to diagnose fuel ρR, and the 14.18 MeV and 17.87 MeV gamma-rays from $^{12}C(n, \gamma)^{13}C$ can also be used to diagnose the ablator. In addition, short-range knock-on fuel ions and fusion alphas that generate gamma-ray lines can be used to probe fuel-ablator mix. In particular, 4.91 MeV and 5.69 MeV gamma-ray lines from $^{13}C(^{2}H, n)^{14}N$; the 2.80 MeV, 3.40 MeV, 4.49 MeV, and 6.03 MeV gamma-ray lines from $^{9}Be(^{2}H, n)^{10}B$; and the 4.40 MeV gamma-ray line from $^{9}Be(^{4}He, n)^{12}C$ can be used for this purpose.

Although the 4-channel GRH has some energy-resolving capabilities and that there are ideas and concepts for gamma-ray-spectroscopy for ICF applications [243], this is an area of research that needs to be advanced significantly.

9.3. Charged-particle diagnostics

As discussed in section 7, charged-particle diagnostics have been used extensively to diagnose ICF implosions with ρR-values up to about 200 mg cm^{-2}. Although this area is at the fore-front of diagnostic-development for ICF applications, there are new and exciting ideas that would open a new window to ICF implosions.

9.3.1. Radiography with multiple mono-energetic charged particles. Mono-energetic charged-particle radiography, based on the D^{3}He gas-filled backlighter that generates 14.7 and 3.0 MeV protons, has been used with great success at various facilities, as discussed in section 7.7. However, such backlighter has some limitations particularly when it is being applied to an environment with strong fields and large ρR values because of large deflections and scattering of 3.0 MeV protons. Consequently, a new backlighter platform that will overcome these challenges is currently being developed at OMEGA and the NIF [244]. This platform is based on a tri-particle, mono-energetic backlighter that provides a 9.5 MeV deuterons in addition to the two 14.7 and 3.0 MeV protons from a DT^{3}He gas-filled capsule implosion. The additional 9.5 MeV deuterons will be important for backlighting experiments, allowing discriminatory, high-quality radiographs of E and B fields and plasma matter. In general, three distinct mono-energetic particles are needed in radiography to distinguish between the three unique 'effects' of electric fields, magnetic fields, and plasma matter (essentially three equations for three unknowns).

10. Concluding remarks

Since the early 70s, each decade has displayed new ICF facilities and nuclear diagnostics that were orders of magnitude more capable than those used during the preceding decade. This is generally a consequence of the fact that the efforts, lessons learned, and experience gained on previous facilities enabled more sophisticated diagnostics on the next-generation ICF facilities. Higher fusion yields have also facilitated higher-quality measurements, which enabled an increased level of understanding about the physics governing the nuclear phase of an ICF implosion. This in turn provided essential guidance of the ICF programs, resulting in further improved fusion yields. With the implementation of new high-fusion-yield facilities world-wide, the next-generation nuclear diagnostics will play an even more important role for decades to come.

ORCID iDs

J A Frenje ⓘ https://orcid.org/0000-0001-6846-0378

References

[1] Nuckolls J H 2007 Contributions to the genesis and progress of ICF *Inertial Confinement Nuclear Fusion: A Historical Approach by its Pioneers* (Guillermo Velarde and Natividad Santamaria, Foxwell & Davies (UK) Ltd ©)

[2] Nuckolls J H 1998 Early steps toward Inertial Confinement Fusion energy (IFE) (1952–1962) UCRL-ID-131075 Lawrence Livermore National Laboratory

[3] Yonas G 2007 A pulsed power Inertial Confinement Fusion journey *Inertial Confinement Nuclear Fusion: A Historical Approach by its Pioneers* (Guillermo Velarde and Natividad Santamaria, Foxwell & Davies (UK) Ltd ©)

[4] Bock R M 2007 Historical remarks on the heavy ion Inertial Confinement Fusion activities in Germany 1976–1985 *Inertial Confinement Nuclear Fusion: A Historical Approach by its Pioneers* (Guillermo Velarde and Natividad Santamaria, Foxwell & Davies (UK) Ltd ©)

[5] Nuckolls J, Wood L, Thiessen A and Zimmerman G 1972 Laser compression of matter to super-high densities *Nature* **239** 139

[6] Sasaki T *et al* 1978 Thermonuclear fusion study by glass laser GEKKO II *Tech. Rep. Osaka Univ.* **28** 169–83

[7] Azechi H *et al* 1978 Inertial Confinement Fusion research in Osaka *Presented at 7th Conf. Plasma Phys. Controlled Nuclear Fusion Research (Innsbruck, Austria* (23–30 August IAEA-CN-37/M-4

[8] Campbell P M, Charatis G and Montry G R 1975 Laser-driven compresison of glass microspheres *Phys. Rev. Lett.* **34** 74

[9] Slivinsky V W, Ahlstrom H G, Tirsell K G, Larsen J, Glaros S, Zimmerman G and Shay H 1975 Measurement of the ion temperature in laser driven fusion *Phys. Rev. Lett.* **35** 1083

[10] Soures J M *et al* 1981 A review of high density, laser driven, implosion experiments at the laboratory for laser energetics *Laser Interaction and Related Plasma Phenomena* vol 5 ed H J Schwarz *et al* (New York: Plenum) pp 463–81

[11] Mitchell K B, Van Hulsteyn D B, McCall G H, Lee P and Greim H 1979 Compression measurements of neon filled glass microballons irradiated by CO_2 laser light *Phys. Rev. Lett.* **42** 232

Perkins R B 1978 Recent progress in Inertical Confinement Fusion Research at the Los Alamos scientific Laboratory *Los Alamos Scientific Laboratory Report* LA-UR-78-1629

[12] Hunt J T and Speck D R 1989 Present and future performance of the NOVA laser system *Opt. Eng.* **28** 461

[13] Yamanaka C 1985 Inertial Confinement Fusion research by Gekko XII glass laser *Fusion Technol.* **8** 179

[14] Thiell G, Adolf A, Andre M, Fleurot N, Friart D, Juraszek D and Schirmann D 1988 The PHEBUS experimental facility operating at 250 ps and 0.53 μm *Laser Part. Beams* **6** 93

[15] Kochemasov G G 1993 Laser fusion investigations on high-power photodissociation iodine lasers ISKRA *Proc. SPIE 1980, Iodine Lasers and Applications*

[16] Kirillov G A, Murugov V M, Punin V T and Shemyakin V I 1990 High power laser system ISKRA V *Laser Part. Beams* **8** 827

[17] Zhao Y 1997 Development of ICF laser driver technology in China *Proc. SPIE 3047, Solid State Lasers for Application to Inertial Confinement Fusion: Second Annual Int. Conf.*

[18] Soures J M, Hutchison R J, Jacobs S D, Lund L D, McCrory R L and Richardson M C 1983 OMEGA: a short-wavelength laser for fusion experiments *Proc. 10th IEEE/NPSS Symp. on Fusion Engineering, SOFE'83* (New York: IEEE) pp 1392–7

[19] Takabe H *et al* 1988 Scalings of implosion experiments for high neutron yield *Phys. Fluids* **31** 2884

[20] Campbell E M, Hunt J T, Bliss E S, Speck D R and Drake R P 1986 Nova experimental facility *Rev. Sci. Instrum.* **57** 2101

[21] McCrory R L *et al* 1988 Laser-driven implosion of thermonuclear fuel to 20 to 40 g cm^{-3} *Nature* **335** 225

[22] Boehly T R *et al* 1997 Initial performance results of the OMEGA laser system *Opt. Commun.* **133** 495

[23] 1997 Review of the department of energy's Inertial Confinement Fusion program, the national ignition facility *Committee for the Review of the Department of Energy's Inertial Confinement Fusion Program, Commission on Physical Sciences, Mathematics, and Applications, National Research Council* (Washington, DC: National Academic Press) (http://nap.edu/catalog/5730.html)

[24] Miller G H, Moses E I and Wuest C R 2004 The National Ignition Facility: enabling fusion ignition for the 21st century *Nucl. Fusion* **44** 228

[25] André M L 1999 The french megajoule laser project (LMJ) *Fusion Eng. Des.* **44** 43

[26] Lindl J, Landen O, Edwards J, Moses E D and NIC Team 2014 Review of the national ignition campaign 2009–2012 *Phys. Plasmas* **21** 020501

[27] Kritcher A L *et al* 2016 Integrated modeling of cryogenic layered highfoot experiments at the NIF *Phys. Plasmas* **23** 052709

[28] Le Pape S *et al* 2018 Fusion energy output greater than the kinetic energy of an imploding shell at the national ignition facility *Phys. Rev. Lett.* **120** 245003

[29] Sangster T C *et al* 2010 Shock-tuned cryogenic DT-implosion performance on OMEGA *Phys. Plasmas* **17** 056312

[30] Regan S P *et al* 2016 Demonstration of fuel hot-spot pressure in excess of 50 Gbar for direct-drive, layered deuterium-tritium implosions on OMEGA *Phys. Rev. Lett.* **117** 025001

[31] Zhao D, Wan L, Lin Z, Shao P and Zhu J 2015 SG-II-Up prototype final optics assembly: optical damage and clean-gas control *High Power Laser Sci. Eng.* **3** e7

[32] Zheng W *et al* 2016 *High Power Laser Sci. Eng.* **4** e21

[33] He X T, Zhang W Y and the Chinese ICF team 2013 Advances in the national inertial fusion program of China *EPJ Web Conf.* **59** 01009

[34] Garanin S G, Bel'kov S A and Bondarenko S V 2012 Conception of UFL-2M laser facility *39th Zvenigorod Int. Conf. on Plasma Physics and Controlled Fusion (Zvenigorod, Russia, 6–10 February)* R-12

[35] Tabak M, Hammer J, Glinsky M E, Kruer W L, Wilks S C, Woodworth J, Campbell E M, Perry M D and Mason R J 1994 Ignition and high gain with ultrapowerful lasers *Phys. Plasmas* **1** 1626

[36] Kodama R *et al* 2001 Fast heating of ultrahigh-density plasma as a step towards laser fusion ignition *Nature* **412** 798

[37] Shiraga H *et al* 2011 Fast ignition integrated experiments with Gekko and LFEX lasers *Plasma Phys. Control. Fusion* **53** 124029

[38] Azechi H *et al* 2013 Present status of fast ignition realization experiment and inertial fusion energy development *Nucl. Fusion* **53** 104021

[39] Batani D *et al* 2011 The HiPER project for Inertial Confinement Fusion and some experimental results on advanced ignition schemes *Plasma Phys. Control. Fusion* **53** 124041

[40] Slutz S A, Herrmann M C, Vesey R A, Sefkow A B, Sinars D B, Rovang D C, Peterson K J and Cuneo M E 2010 Pulsed-power-driven cylindrical liner implosions of laser preheated fuel magnetized with an axial field *Phys. Plasmas* **17** 056303

[41] Gomez M R *et al* 2105 Demonstration of thermonuclear conditions in magnetized liner inertial fusion experiments *Phys. Plasmas* **22** 056306

[42] Lindl J D, Amendt P, Berger R L, Glendinning S G, Glenzer S H, Haan S W, Kauffman R L, Landen O L and Suter L J 2004 The physics basis for ignition using indirect-drive targets on the national ignition facility *Phys. Plasmas* **11** 339

[43] Edwards M J *et al* 2013 *Phys. Plasmas* **20** 070501

Moses E I and Boyd R N 2013 Progress towards ignition on the national ignition facility *Phys. Plasmas* **20** 070501

[44] Freidberg J P 2007 *Fusion Energy and Plasma Physics* (Cambridge: Cambridge University Press)

[45] Betti R, Anderson K S, Chang P Y, Nora R, Zhou C D, Spears B, Edwards J, Haan S W and Lindl J 2010 Thermonuclear ignition in Inertial Confinement Fusion and comparison with magnetic confinement *Phys. Plasmas* **17** 058102

[46] Bose A, Betti R, Shvarts D and Woo K M 2017 The physics of long- and intermediate-wavelength asymmetries of the hot spot: compression hydrodynamics and energetics *Phys. Plasmas* **24** 102704

[47] Bodner S E 1974 Rayleigh–Taylor instability and laser-pellet fusion *Phys. Rev. Lett.* **33** 761

[48] Smalyuk V A, Hu S X, Hager J D, Delettrez J A, Meyerhofer D D, Sangster T C and Shvarts D 2009 Spherical Rayleigh–Taylor growth of three-dimensional broadband perturbations on OMEGA *Phys. Plasmas* **16** 112701

[49] Smalyuk V A, Xu S X, Hager J D, Delettrez J A, Meyerhofer D D, Sangster T C and Shvarts D 2009 Rayleigh-Taylor growth measurements in the acceleration phase of spherical implosions on OMEGA *Phys. Rev. Lett.* **103** 105001

[50] Frenje J A *et al* 2013 Diagnosing implosion performance at the National Ignition Facility (NIF) by means of neutron spectrometry *Nucl. Fusion* **53** 043014

[51] Fisher R K, Parks P B, McChesney J M and Rosenbluth M N 1994 Fast alpha particle diagnostics using knock-on ion tails *Nucl. Fusion* **34** 1291

[52] Ballabio L, Gorini G and Källne J 1997 α-particle knock-on signature in the neutron emission of DT plasmas *Phys. Rev. E* **55** 3358

[53] Källne J, Ballabio L, Frenje J, Conroy S, Ericsson G, Tardocchi M, Traneus E and Gorini G 2000 Observation of the alpha particle 'Knock-On' neutron emission from magnetically confined DT fusion plasmas *Phys. Rev. Lett.* **85** 1246

[54] Petrasso R D *et al* 1996 Measuring implosion symmetry and core conditions in the national ignition facility *Phys. Rev. Lett.* **77** 2718

[55] Casey D T *et al* 2017 Thermonuclear reactions probed at stellar-core conditions with laser-based inertial-confinement fusion *Nat. Phys.* **13** 1227–31

[56] Brysk H 1973 Fusion neutron energies and spectra *Plasma Phys.* **15** 611

[57] Ballabio L, Kallne J and Gorini G 1998 Relativistic calculation of fusion product spectra for thermonuclear plasmas *Nucl. Fusion* **38** 1723

[58] Appelbe B and Chittenden J 2011 The production spectrum in fusion plasmas *Plasma Phys. Control. Fusion* **53** 045002

[59] Munro D H 2016 Interpreting inertial fusion neutron spectra *Nucl. Fusion* **56** 036001

[60] Gatu Johnson M *et al* 2013 Measurements of collective fuel velocities in deuterium-tritium exploding pusher and cryogenically layered deuterium-tritium implosions on the NIF *Phys. Plasmas* **20** 042707

[61] Munro D H 2017 Impact of temperature-velocity distribution on fusion neutron peak shape *Phys. Plasmas* **24** 056301

[62] Murphy T J 2014 The effect of turbulent kinetic energy on inferred ion temperature from neutron spectra *Phys. Plasmas* **21** 072701

[63] Frenje J A *et al* 2011 Measurements of the differential cross section for the elastic n-^{3}H and n-^{2}H scattering at 14.1 MeV by using an Inertial Confinement Fusion (ICF) facility *Phys. Rev. Lett.* **107** 122502

[64] Allred J C, Armstrong A H and Rosen L 1953 The interaction of 14 MeV neutrons with protons and deuterons *Phys. Rev.* **91** 90

[65] Dave J H and Gould C R 1983 Optical model analysis of scattering of 7 to 15 MeV neutrons from 1−p shell nuclei *Phys. Rev. C* **28** 2212

[66] Knoll G F 2010 *Radiation Detection and Measurement* 4th edn (New York: Wiley)

[67] Frenje J A, Li C K, Séguin F H, Casey D T, Petrasso R D, Sangster T C, Betti R, Glebov V Y and Meyerhofer D D 2009 Diagnosing fuel ρR and ρR asymmetries in cryogenic deuterium-tritium implosions using charged-particle spectrometry at OMEGA *Phys. Plasmas* **16** 042704

[68] Atzeni S and Meyer-Ter-Vehn J 2004 The physics of inertial fusion: beam plasma interaction, hydrodynamics, hot dense matter *International Series of Monographs on Physics* (Oxford: Oxford University Press)

[69] Brown L S *et al* 2005 Charged particle motion in a highly ionized plasma *Phys. Rep.* **410** 237

[70] Li C K and Petrasso R D 1993 Charged-particle stopping powers in Inertial Confinement Fusion plasmas *Phys. Rev. Lett.* **70** 3059

Li C K and Petrasso R D 2015 Erratum: charged-particle stopping powers in Inertial Confinement Fusion plasmas [Phys. Rev. Lett. 70, 3059 (1993)] *Phys. Rev. Lett.* **114** 199901

[71] Maynard G *et al* 1985 Born random phase approximation for ion stopping in an arbitrarily degenerate electron fluid *J. Physique* **46** 1113

[72] Frenje J A, Grabowski P E, Li C K, Séguin F H, Zylstra A B, Gatu Johnson M, Petrasso R D, Yu Glebov V and Sangster T C 2015 Measurements of ion stopping around the bragg peak in high energy-density plasmas *Phys. Rev. Lett.* **115** 205001

[73] Frenje J A *et al* 2019 Experimental validation of low-Z ion-stopping formalisms around the bragg peak in high-energy-density plasmas *Phys. Rev Lett.* **122** 015002

[74] Azechi H *et al* 1986 Experimental determination of fuel density-radius product of Inertial Confinement Fusion targets using secondary nuclear fusion reactions *Appl. Phys. Lett.* **49** 555

[75] Azechi H, Stapf R O, Miyanaga N, Tsuji R, Yamanaka M, Ido S, Nishihara K, Yabe T and Yamanaka C 1987 Study of fuel-pusher mixing in laser-driven implosions, using secondary nuclear fusion reactions *Phys. Rev. Lett.* **59** 2635

[76] Azechi H, Cable M D and Stapf R O 1991 Review of secondary and tertiary reactions, and neutron scattering as diagnostic techniques for Inertial Confinement Fusion targets *Laser Part. Beams* **9** 119

[77] Cable M D and Hatchett S P 1987 Neutron spectra from Inertial Confinement Fusion targets for measurement of fuel areal density and charged particle stopping powers *J. Appl. Phys.* **62** 2233

[78] Séguin F H *et al* 2002 Using secondary-proton spectra to study the compression and symmetry of deuterium-filled capsules at OMEGA *Phys. Plasmas* **9** 2725

[79] Kurebayashi S *et al* 2005 Using nuclear data and Monte Carlo techniques to study areal density and mix in D_2 implosions *Phys. Plasmas* **12** 032703

[80] Rinderknecht H G *et al* 2015 Using multiple secondary fusion products to evaluate fuel ρR, electron temperature, and mix in deuterium-filled implosions at the NIF *Phys. Plasmas* **22** 082709

[81] Springer P T *et al* 2019 A 3D dynamic model to assess impacts of low-mode asymmetry, aneurysms, and mix induced radiative loss on capsule performance across ICF platforms *Nucl. Fusion* **59** 032009

[82] Rosenberg M J *et al* 2014 Exploration of the transition from the hydrodynamiclike to the strongly kinetic regime in shock-driven implosions *Phys. Rev. Lett.* **112** 185001

[83] Rinderknecht H G *et al* 2014 Kinetic mix mechanisms in shock-driven Inertial Confinement Fusion implosions *Phys. Plasmas* **21** 056311

[84] Rinderknecht H G *et al* 2015 Ion thermal decoupling and species separation in shock-driven implosions *Phys. Rev. Lett.* **114** 025001

[85] Hoffman N M *et al* 2015 Approximate models for the ion-kinetic regime in inertial-confinement-fusion capsule implosions *Phys. Plasmas* **22** 052707

[86] Rosenberg M J *et al* 2015 Assessment of ion kinetic effects in shock-driven Inertial Confinement Fusion implosions using fusion burn imaging *Phys. Plasmas* **22** 062702

[87] Sio H *et al* 2019 Observations of multiple nuclear reaction histories and fuel-ion species dynamics in Shock-Driven Inertial Confinement Fusion implosions *Phys. Rev. Lett.* **122** 035001

[88] Li C K *et al* 2006 Monoenergetic proton backlighter for measuring E and B fields and for radiographing implosions and high-energy density plasmas *Rev. Sci. Instrum.* **77** 10E725

[89] Li C K *et al* 2006 Measuring E and B fields in laser-produced plasmas with monoenergetic proton radiography *Phys. Rev. Lett.* **97** 135003

[90] Rygg J R *et al* 2008 Supplementary material: proton radiography of inertial fusion implosions *Science* **319** 1223

[91] Li C K *et al* 2008 Monoenergetic-proton-radiography measurements of implosion dynamics in direct-drive inertial-confinement fusion *Phys. Rev Lett.* **100** 225001

[92] Li C K *et al* 2009 Study of direct-drive capsule implosions in Inertial Confinement Fusion with proton radiography *Plasma Phys. Control. Fusion* **51** 014003

[93] Hahn K D, Ruiz C L, Cooper G W, Nelson A J, Chandler G A, Leeper R J, McWatters B R, Smelser R M and Torres J A 2012 Calibration of neutron-yield diagnostics in attenuating and scattering environments *Rev. Sci. Instrum.* **83** 10D914

[94] Ruiz C L, Leeper R J, Schmidlapp F A, Cooper G and Malbrough D J 1992 Absolute calibration of a total yield indium activation detector for DD and DT neutrons *Rev. Sci. Instrum.* **63** 4889

[95] Barnes C W, Murphy T J and Oertel J A 2001 High-yield neutron activation system for the national ignition facility *Rev. Sci. Instrum.* **72** 818

[96] Bleuel D L *et al* 2012 Neutron activation diagnostics at the national ignition facility *Rev. Sci. Instrum.* **83** 10D313

[97] Yeamans C B, Bleuel D L and Bernstein L A 2012 Enhanced NIF neutron activation diagnostics *Rev. Sci. Instrum.* **83** 10D315

[98] Lerche R A, McLerran W R and Tripp G R 1976 *UCRL Report No.* 50021-76 Lawrence Livermore National Laboratory, Livermore, CA

[99] Cooper G W *et al* 2012 Copper activation deuterium-tritium neutron yield measurements at the national ignition facility *Rev. Sci. Instrum.* **83** 10D918

[100] Hahn K D, Cooper G W, Ruiz C L, Fehl D L, Chandler G A, Knapp P F, Leeper R J, Nelson A J, Smelser R M and Torres J A 2014 Fusion-neutron-yield, activation measurements at the Z accelerator: design, analysis, and sensitivity *Rev. Sci. Instrum.* **85** 043507

[101] Cooper G W and Ruiz C L 2001 NIF total neutron yield diagnostic *Rev. Sci. Instrum.* **72** 814

[102] Landoas O *et al* 2011 Absolute calibration method for laser megajoule neutron yield measurement by activation diagnostics *Rev. Sci. Instrum.* **82** 073501

[103] Caillaud T *et al* 2016 Recent advance in target diagnostics on the Laser MégaJoule (LMJ) *Proc. SPIE 9966, Target Diagnostics Physics and Engineering for Inertial Confinement Fusion V* 996606

[104] Yeamans C B and Bleuel D L 2016 The spatially distributed neutron activation diagnostic FNADs at the national ignition facility *Fusion Sci. Technol.* **72** 120

[105] Casey D T *et al* 2015 Improved performance of high areal density indirect drive implosions at the national ignition facility using a Four-Shock adiabat shaped drive *Phys. Rev. Lett.* **115** 105001

[106] Zifeng S, Jiabin C, Zhongjie L, Xiayu Z and Qi T 2017 The calibration of DD neutron indium activation diagnostic *Plasma Sci. Technol.* **17** 337

[107] Zifeng S, Jiabin C, Zhongjie L, Xiayu Z and Qi T 2014 Evaluation of uncertainty in DD neutron yield diagnosis by indium activation *High Power Laser Part. Beams* **26** 1165

[108] Glebov V Y, Stoeckl C, Sangster T C, Meyerhofer D D, Radha P B, Padalino S, Baumgart L, Colburn R and Fuschino J 2003 Carbon activation diagnostic for tertiary neutron measurements *Rev. Sci. Instrum.* **74** 1717

[109] Kilkenny J D 1992 Recent diagnostic developments at Nova *Rev. Sci. Instrum.* **63** 4688

[110] Murphy T J, Jimerson J L, Berggren R R, Faulkner J R, Oertel J A and Walsh P J 2001 Neutron time-of-flight and emission time diagnostics for the national ignition facility *Rev. Sci. Instrum.* **72** 850

[111] Yu Glebov V *et al* 2010 The national ignition facility neutron time-of-flight system and its initial performance *Rev. Sci. Instrum.* **81** 10D325

[112] Chen Z *et al* 2018 Ion temperature measurements of indirect-drive implosions with the neutron time-of-flight detector on SG-III laser facility *Rev. Sci, Instrum.* **89** 023504

[113] Nagai T *et al* 2014 The development of the neutron detector for the fast ignition experiment by using LFEX and Gekko XII facility *Plasma Fusion Res.* **9** 4404105

[114] Johnson M G *et al* 2012 Neutron spectrometry—an essential tool for diagnosing implosions at the national ignition facility *Rev. Sci. Instrum.* **83** 10D308

[115] Sayre D B *et al* 2013 Measurement of the T + T neutron spectrum using the national ignition facility *Phys. Rev. Lett.* **111** 052501

[116] Johnson M G *et al* 2018 Experimental evidence of a variant neutron spectrum from the T(t,2n)4He reaction at center-of-mass energies in the range of 16–50 keV *Phys. Rev. Lett.* **121** 042501

[117] Hatarik R *et al* 2015 Analysis of the neutron time-of-flight spectra from Inertial Confinement Fusion experiments *J. Appl. Phys.* **118** 184502

[118] Cerjan C J *et al* 2018 Dynamic high energy density plasma environments at the national ignition facility for nuclear science research *J. Phys. G: Nucl. Part. Phys.* **45** 033003

[119] Hatarik R, Bernstein L A, Caggiano J A, Carman M L, Schneider D H G, Zaitseva N P and Wiedeking M 2012 Characterizing time decay of bibenzyl scintillator using time correlated single photon counting *Rev. Sci. Instrum.* **83** 10D911

[120] Yu Glebov V *et al* 2012 Testing a new NIF neutron time-of-flight detector with a bibenzyl scintillator on OMEGA *Rev. Sci. Instrum.* **83** 10D309

[121] Kabadi N V *et al* 2016 Sensitivity of chemical vapor deposition diamonds to DD and DT neutrons at OMEGA and the national ignition facility *Rev. Sci. Instrum.* **87** 11D817

[122] Rinderknecht H G *et al* 2012 A novel particle time of flight diagnostic for measurements of shock- and compression-bang times in D3He and DT implosions at the NIF *Rev. Sci. Instrum.* **83** 10D902

[123] Tietbohl G L, Cable M D, Nelson M B, Bennett C E, Mant G, Deane D J and Connolly N A 1990 LANSA: a large neutron scintillator array for neutron spectroscopy at Nova *Rev. Sci. Instrum.* **61** 3231

[124] Chrien R E, Simmons D F and Holmberg D L 1992 Neutron time-of-flight ion temperature diagnostic for inertial-confinement-fusion experiments *Rev. Sci. Instrum.* **63** 4886

[125] Knauer J P, Kremens R L, Russotto M A and Tudman S 1995 Using cosmic rays to monitor large scintillator arrays *Rev. Sci. Instrum.* **66** 926

[126] Izumi N, Yamagajo T, Nakano T, Kasai T, Azechi H, Kato Y and Nakai S 1996 Development of multi channel neutron spectrometer at GEKKO XII laser fusion facility *AIP Conf. Proc.* **369** 550

[127] Gamalii E G, Yu Gus'Kov S, Krokhin O N and Ruzanov V B 1975 Possibility of determining the characteristics of laser plasma by measuring the neutrons of the DT reactions *JETP Lett.* **21** 70

[128] Cable M D and Hatchett S P 1987 Neutron spectra from Inertial Confinement Fusion targets for measurement of fuel areal density and charged particle stopping powers *J. Appl. Phys.* **62** 2233

[129] Lerche R A, Hatchett S P, Cable M D, Nelson M B and Murphy T J 1992 Plasma temperatures from first-hit neutron time-of-flight spectra *Rev. Sci. Instrum.* **63** 4877

[130] Chrien R E, Klare K A and Murphy T J 1997 Measurements of neutron spectra from Nova targets *Rev. Sci. Instrum.* **68** 607

[131] Lerche R A, Phillion D W and Tietbohl G L 1995 25 ps neutron detector for measuring ICF-target burn history *Rev. Sci. Instrum.* **66** 933

[132] Stoeckl C, Yu Glebov V, Roberts S, Sangster T C, Lerche R A, Griffith R L and Sorce C 2003 Ten-inch manipulator-based neutron temporal diagnostic for

cryogenic experiments on OMEGA *Rev. Sci. Instrum.*
74 1713

[133] Frenje J A *et al* 2004 Measuring shock-bang timing and ρR
evolution of D^{3}He implosions at OMEGA *Phys. Plasmas*
11 2798

[134] Sio H *et al* 2016 A particle x-ray temporal diagnostic (PXTD)
for studies of kinetic, multi-ion effects, and ion-electron
equilibration rates in Inertial Confinement Fusion plasmas at
OMEGA *Rev. Sci. Instrum.* **87** 11D701

[135] Guler N, Volegov P, Danly C R, Grim G P, Merrill F E and
Wilde C H 2012 Simultaneous usage of pinhole and
penumbral apertures for imaging small scale neutron sources
from Inertial Confinement Fusion experiments *Rev. Sci.
Instrum.* **83** 10D316

[136] Ress D, Lerche R A, Ellis R I and Lane S M 1988 *Rev. Sci.
Instrum.* **59** 1694

Ress D, Lerche R A, Ellis R J, Heaton G W and Lehr D E 1995
High-sensitivity scintillating-fiber imaging detector for high-
energy neutrons *Rev. Sci. Instrum.* **66** 4943

[137] Disdier L, Lerche R A, Bourgade J L and Yu Glebov V 2004
Capillary detector with deuterated scintillator for Inertial
Confinement Fusion neutron images *Rev. Sci. Instrum.*
75 2134

[138] Caillaud T *et al* 2012 Development of the large neutron
imaging system for Inertial Confinement Fusion experiments
Rev. Sci. Instrum. **83** 033502

[139] Ampleford D J *et al* 2018 One dimensional imager of
neutrons on the Z machine *Rev. Sci. Instrum.* **89** 10I132

[140] Grim G P *et al* 2013 Nuclear imaging of the fuel assembly in
ignition experiments *Phys. Plasmas* **20** 056320

[141] Merrill F E *et al* 2012 The neutron imaging diagnostic at NIF
(invited) *Rev. Sci. Instrum.* **83** 10D317

[142] Fatherley V E, Batha S H, Danly C R, Goodwin L A and
Herrmann H W 2017 System design of the NIF neutron
imaging system north pole *Proc. SPIE 10390, Target
Diagnostics Physics and Engineering for Inertial
Confinement Fusion VI* 103900F

[143] Frenje J A *et al* 2002 Absolute measurements of neutron
yields in DD and DT implosions at the OMEGA laser
facility using CR-39 track detectors *Rev. Sci. Instrum.*
73 2597

[144] Lahmann B, Milanese L M, Han W, Gatu Johnson M,
Séguin F H, Frenje J A, Petrasso R D, Hahn K D and
Jones B 2016 Application of the coincidence counting
technique to DD neutron spectrometry data at the NIF,
OMEGA, and Z *Rev. Sci. Instrum.* **87** 11D801

[145] Frenje J A *et al* 2001 A neutron spectrometer for precise
measurements of DT neutrons from 10 to 18 MeV at
OMEGA and the national ignition facility *Rev. Sci. Instrum.*
72 854

[146] Frenje J A *et al* 2008 First measurements of the absolute
neutron spectrum using the magnetic recoil spectrometer at
OMEGA *Rev. Sci. Instrum.* **79** 10E502

[147] Frenje J A *et al* 2010 Probing high areal-density (ρR)
cryogenic DT implosions using down scattered neutron
spectra measured by the magnetic recoil spectrometer
(MRS) *Phys. Plasmas* **17** 056311

[148] Casey D T *et al* 2012 Measuring the absolute deuterium–
tritium neutron yield using the magnetic recoil spectrometer
at OMEGA and the NIF *Rev. Sci. Instrum.* **83** 10D912

[149] Gatu Johnson M *et al* 2014 Measurements of fuel and ablator
ρR in symmetry-capsule implosions with the magnetic recoil
neutron spectrometer (MRS) on the national ignition facility
Rev. Sci. Instrum. **85** 11E104

[150] X-5 Monte Carlo Team 2003 MCNP-A general Monte Carlo
n-particle transport code *Los Alamos National Laboratory*
Report No. LA-UR-03-1987 Version 5

[151] Casey D T *et al* 2011 The coincidence counting technique for
orders of magnitude background reduction in data obtained

with the magnetic recoil spectrometer at OMEGA and the
NIF *Rev. Sci. Instrum.* **82** 073502

[152] Zhang J *et al* 2015 Development of a compact magnetic
proton recoil spectrometer for measurement of deuterium-
tritium neutrons *Rev. Sci. Instrum.* **86** 125115

[153] Kim Y *et al* 2012 D-T gamma-to-neutron branching ratio
determined from Inertial Confinement Fusion plasmas *Phys.
Plasmas* **19** 056313

[154] Herrmann H W *et al* 2010 Diagnosing Inertial Confinement
Fusion gamma ray physics *Rev. Sci. Instrum.* **81** 10D333

[155] Herrmann H W *et al* 2016 Next generation gamma-ray
Cherenkov detectors for the national ignition facility *Rev.
Sci. Instrum.* **87** 11E732

[156] Rubery M S *et al* 2010 GEANT4 simulations of Cherenkov
reaction history diagnostics *Rev. Sci. Instrum.* **81** 10D328

[157] Hoffman N M, Wilson D C, Herrmann H W and Young C S
2010 Using gamma-ray emission to measure areal density of
Inertial Confinement Fusion capsules *Rev. Sci. Instrum.* **81**
10D332

[158] Cerjan C, Sayre D B, Landen O L, Church J A, Stoeffl W,
Grafil E M, Herrmann H W, Hoffman N M and Kim Y 2015
Gamma reaction history ablator areal density constraints
upon correlated diagnostic modeling of national ignition
facility implosion experiments *Phys. Plasmas* **22** 032710

[159] Herrmann H W *et al* 2018 Progress on next generation
gamma-ray Cherenkov detectors for the national ignition
facility *Rev. Sci. Instrum.* **89** 10I148

[160] Zylstra A B, Herrmann H W, Kim Y H, McEvoy A M,
Schmitt M J, Hale G, Forrest C, Yu Glebov V and Stoeckl C
2017 Simultaneous measurement of the HT and DT fusion
burn histories in inertial fusion Implosions *Rev. Sci. Instrum.*
88 053504

[161] Zylstra A B, Herrmann H W, Kim Y H, Meaney K,
Geppert-Kleinrath H, Schmitt M J, Hoffman N M,
Leatherland A and Gales S 2018 Cherenkov detector
analysis for implosions with multiple nuclear reactions *Rev.
Sci. Instrum.* **89** 10I103

[162] Herrmann H W *et al* 2014 Extended performance gas
Cherenkov detector for gamma-ray detection in high-energy
density experiments *Rev. Sci. Instrum.* **85** 11E124

[163] Kim Y, Herrmann H W, McEvoy A M, Young C S,
Hamilton C, Schwellenbach D D, Malone R M,
Kaufman M I and Smith A S 2016 Aerogel Cherenkov
detector for characterizing the intense flash x-ray source,
Cygnus, spectrum *Rev. Sci. Instrum.* **87** 11E723

[164] Séguin F H *et al* 2003 Spectrometry of charged particles from
inertial-confinement-fusion plasmas *Rev. Sci. Instrum.* **74** 975

[165] Séguin F H *et al* 2002 Measurements of ρR asymmetries at
burn time in inertial-confinement-fusion capsules *Phys.
Plasmas* **9** 3558

[166] Li C K *et al* 2002 Effects of fuel-shell mix upon direct-drive,
spherical implosions on OMEGA *Phys. Rev. Lett.* **89** 165002

[167] Petrasso R D *et al* 2003 Measuring implosion dynamics
through ρR evolution in inertial-confinement fusion
experiments *Phys. Rev. Lett.* **90** 095002

[168] Smalyuk V A *et al* 2003 Time-resolved areal density
measurements with proton spectroscopy in spherical
implosions *Phys. Rev. Lett.* **90** 135002

[169] Li C K *et al* 2003 Capsule areal density asymmetries inferred
from 14.7 MeV protons in direct-drive OMEGA implosions
Phys. Plasmas **10** 1919

[170] Li C K *et al* 2004 Effects of fuel-shell mix upon direct-drive,
spherical implosions on OMEGA *Phys. Rev. Lett.* **92**
205001

[171] Rygg J R *et al* 2006 Tests of the hydrodynamic equivalence
of direct-drive implosions with different D$_2$ and ^{3}He
mixtures *Phys. Plasmas* **13** 052702

[172] Wilson D C, Singleton R L Jr, Grondalski J P, Hoffman N M,
Nobile A Jr, Séguin F H, Frenje J A, Li C K and

Petrasso R D 2006 Diagnosing ablator burn through in ignition capsules using $D_2 + {}^3$He gas filled surrogates *Rev. Sci. Instrum.* **77** 10E711

[173] Zhou C D *et al* 2006 High-ρR implosions for fast-ignition fuel assembly *Phys. Rev. Lett.* **98** 025004

[174] Rygg J R *et al* 2007 Nuclear measurements of fuel-shell mix in Inertial Confinement Fusion implosions at OMEGA *Phys. Plasmas* **14** 056306

[175] Delamater N D *et al* 2008 Use of d-^{3}He proton spectroscopy as a diagnostic of shell ρR in capsule implosion experiments with $\sim$0.2 NIF scale high temperature Hohlraums at Omega *Rev. Sci. Instrum.* **79** 10E526

[176] Zylstra A B *et al* 2012 Charged-particle spectroscopy for diagnosing shock ρR and strength in NIF implosions *Rev. Sci. Instrum.* **83** 10D901

[177] Séguin F H *et al* 2002 Diagnostic use of secondary d-^{3}He proton spectra for *dd* OMEGA targets *Phys. Plasmas* **9** 2275

[178] Sangster T C *et al* 2003 Direct-drive cryogenic target implosion performance on OMEGA *Phys. Plasmas* **10** 1937

[179] McKenty P W *et al* 2004 Direct-drive cryogenic target implosion performance on OMEGA *Phys. Plasmas* **11** 2790

[180] Sangster T C *et al* 2007 Cryogenic DT and D_2 targets for Inertial Confinement Fusion *Phys. Plasmas* **14** 058101

[181] Theobald W *et al* 2008 Initial experiments on the shock-ignition Inertial Confinement Fusion concept *Phys. Plasmas* **15** 056306

[182] Goncharov V N *et al* 2008 Performance of direct-drive cryogenic targets on OMEGA *Phys. Plasmas* **15** 056310

[183] Sangster T C *et al* 2008 High-areal-density fuel assembly in direct-drive cryogenic implosions *Phys. Rev. Lett.* **100** 185006

[184] Stoeckl C *et al* 2008 Fast-ignition target design and experimental-concept validation on OMEGA *Plasma Phys. Control. Fusion* **50** 124044

[185] Theobald W *et al* 2009 Advanced-ignition-concept exploration on OMEGA *Plasma Phys. Control. Fusion* **51** 124052

[186] Li C K *et al* 2010 Diagnosing indirect-drive inertial-confinement-fusion implosions with charged particles *Plasma Phys. Control. Fusion* **52** 124027

[187] Frenje J A *et al* 2002 Studies of fuel and shell areal densities of OMEGA capsule implosions using scattered protons *Phys. Plasmas* **9** 4719

[188] Frenje J A *et al* 2009 Diagnosing ablator ρR and ρR asymmetries in capsule implosions using charged-particle spectrometry at the national ignition facility *Phys. Plasmas* **16** 022702

[189] Frenje J A, Li C K, Séguin F H, Casey D T, Petrasso R D, Sangster T C, Betti R, Yu Glebov V and Meyerhofer D D 2009 Diagnosing fuel ρR and ρR asymmetries in cryogenic deuterium-tritium implosions using charged-particle spectrometry at OMEGA *Phys. Plasmas* **16** 042704

[190] Zhang X *et al* 2017 Preliminary diagnosis of areal density in the deuterium fuel capsule by proton measurement at SG-III facility *Proc. SPIE* **10173** 101730T

[191] Zhang X *et al* 2015 The application of proton spectrometers at the SG-III facility for ICF implosion areal density diagnostics *High Power Laser Sci. Eng.* **3** e28

[192] Rinderknecht H G *et al* 2014 A magnetic particle time-of-flight (MagPTOF) diagnostic for measurements of shock- and compression-bang time at the NIF *Rev. Sci. Instrum.* **85** 11D901

[193] Freeman C G *et al* 2011 Calibration of a Thomson parabola ion spectrometer and Fujifilm imaging plate detectors for protons, deuterons, and alpha particles *Rev. Sci. Instrum.* **82** 073301

[194] Cobble J A, Flippo K A, Offermann D T, Lopez F E, Oertel J A, Mastrosimone D, Letzring S A and Sinenian N 2011 High-resolution Thomson parabola for ion analysis *Rev. Sci. Instrum.* **82** 113504

[195] Sinenian N *et al* 2012 Heavy-ion emission from short-pulse laser-plasma interactions with thin foils *Phys. Plasmas* **19** 093118

[196] Séguin F H *et al* 2004 D^{3}He-proton emission imaging for inertial-confinement-fusion experiments *Rev. Sci. Instrum.* **75** 3520

[197] DeCiantis J L *et al* 2006 Proton core imaging of the nuclear burn in Inertial Confinement Fusion implosions *Rev. Sci. Instrum.* **77** 043502

[198] Séguin F H *et al* 2006 Measured dependence of nuclear burn region size on implosions parameters in Inertial Confinement Fusion experiments *Phys. Plasmas* **13** 082704

[199] Séguin F H *et al* 2016 Effects of fuel-capsule shimming and drive asymmetry on inertial-confinement-fusion symmetry and yield *Phys. Plasmas* **23** 032705

[200] Li C K *et al* 2007 Observation of the decay dynamics and instabilities of megagauss field structures in laser-produced plasmas *Phys. Rev. Lett.* **99** 015001

[201] Li C K, Séguin F H, Frenje J A, Rygg J R, Petrasso R D, Town R P J, Landen O L, Knauer J P and Smalyuk V A 2007 Observation of megagauss-field topology changes due to magnetic reconnection in laser-produced plasmas *Phys. Rev Lett.* **99** 055001

[202] Rygg J R *et al* 2008 Proton radiography of inertial fusion implosions *Science* **319** 1223

[203] Li C K *et al* 2009 Proton radiography of dynamic electric and magnetic fields in laser-produced high-energy-density plasmas *Phys. Plasmas* **16** 056304

[204] Li C K *et al* 2009 Observations of electromagnetic fields and plasma flow in hohlraums with proton radiography *Phys. Rev Lett.* **100** 205001

[205] Li C K *et al* 2009 Pressure-driven, resistive magnetohydrodynamic interchange instabilities in laser-produced high-energy-density plasmas *Phys. Rev. E* **80** 016407

[206] Li C K *et al* 2010 Charged-particle probing of x-ray-driven inertial-fusion implosions *Science* **327** 1231

[207] Li C K *et al* 2012 Impeding hohlraum plasma stagnation in inertial-confinement Fusion *Phys. Rev. Lett.* **108** 025001

[208] Manuel M J-E, Sinenian N, Séguin F H, Li C K, Frenje J A, Rinderknecht H G, Casey D T, Zylstra A B, Petrasso R D and Beg F N 2012 Mapping return currents in laser-generated Z-pinch plasmas using proton *Appl. Phys. Lett.* **100** 203505

[209] Séguin F H *et al* 2012 Time evolution of filamentation and self-generated fields in the coronae of directly driven inertial-confinement fusion capsules *Phys. Plasmas* **19** 012701

[210] Manuel M J-E *et al* 2012 First measurements of Rayleigh–Taylor-induced magnetic fields in laser-produced plasmas *Phys. Rev. Lett.* **108** 255006

[211] Rosenberg M J, Ross J S, Li C K, Town R P J, Séguin F H, Frenje J A, Froula D H and Petrasso R D 2012 Characterization of single and colliding laser-produced plasma bubbles using Thomson scattering and proton radiography *Phys. Rev. E* **86** 056407

[212] Manuel M J-E, Zylstra A B, Rinderknecht H G, Casey D T, Rosenberg M J, Sinenian N, Li C K, Frenje J A, Séguin F H and Petrasso R D 2012 Source characterization and modeling development for monoenergetic-proton radiography experiments on OMEGA *Rev. Sci. Instrum.* **83** 063506

[213] Manuel M J-E *et al* 2012 Rayleigh–Taylor-induced magnetic fields in laser-irradiated plastic foils *Phys. Plasmas* **19** 082710

[214] Li C K *et al* 2013 Proton imaging of hohlraum plasma stagnation in inertial-confinement-fusion experiments *Nucl. Fusion* **53** 073022

[215] Li C K *et al* 2013 Structure and dynamics of colliding plasma jets *Phys. Rev. Lett.* **111** 235003

[216] Manuel M J-E *et al* 2013 Instability-driven electromagnetic fields in coronal plasmas *Phys. Plasmas* **20** 056301

[217] Rosenberg M J *et al* 2014 Empirical assessment of the detection efficiency of CR-39 at high proton fluence and a compact, proton detector for high-fluence applications *Rev. Sci. Instrum.* **85** 043302

[218] Manuel M J-E *et al* 2015 Collisional effects on Rayleigh–Taylor-induced magnetic fields *Phys. Plasmas* **22** 056305

[219] Rosenberg M J, Li C K, Fox W, Igumenshchev I, Séguin F H, Town R P J, Frenje J A, Stoeckl C, Glebov V and Petrasso R D 2015 A laboratory study of asymmetric magnetic reconnection in strongly driven plasmas *Nat. Commun.* **6** 6190

[220] Rosenberg M J, Li C K, Fox W, Zylstra A B, Stoeckl C, Séguin F H, Frenje J A and Petrasso R D 2015 Slowing of magnetic reconnection concurrent with weakening plasma inflows and increasing collisionality in strongly driven laser-plasma experiments *Phys. Rev. Lett.* **114** 205004

[221] Li C K *et al* 2016 Scaled laboratory experiments explain the kink behavior of the Crab Nebula jet *Nat. Commun.* **7** 13081

[222] Shaughnessy D A, Velsko C A, Jedlovec D R, Yeamans C B, Moody K J, Tereshatov E, Stoeffl W and Riddle A 2012 The radiochemical analysis of gaseous samples (RAGS) apparatus for nuclear diagnostics at the national ignition facility *Rev. Sci. Instrum.* **83** 10D917

[223] Gostic J M, Shaughnessy D A, Moore K T, Hutcheon I D, Grant P M and Moody K J 2012 Solid debris collection for radiochemical diagnostics at the national ignition facility *Rev. Sci. Instrum.* **83** 10D904

[224] Shaughnessy D A *et al* 2014 Radiochemical determination of Inertial Confinement Fusion capsule compression at the national ignition facility *Rev. Sci. Instrum.* **85** 063508

[225] Stoyer M A, Velsko C A, Spears B K, Hicks D G, Hudson G B, Sangster T C and Freeman C G 2012 Collection of solid and gaseous samples to diagnose Inertial Confinement Fusion implosions *Rev. Sci. Instrum.* **83** 023505

[226] Galbraith J, Bettencourt R, Shaughnessy D, Gharibyan N, Talison B, Morris K and Smith C 2015 Vast area detection for experimental radiochemistry (VADER) at the national ignition facility *Proc. SPIE* **9591** 95910G

[227] Edwards E R, Jedlovec D R, Carrera J A and Yeamans C B 2016 Development of enhanced, permanently-installed, neutron activation diagnostic hardware for NIF *J. Phys.: Conf. Ser.* **717** 012091

[228] Root J R, Jedlovec D R, Edwards E R, Yeamans C B, Golod T, Hernandez J, Adams P and Brunton G 2017 Development of the real time neutron activation diagnostic system for NIF *Proc. SPIE 10390, Target Diagnostics Physics and Engineering for Inertial Confinement Fusion VI* 103900J

[229] Schlossberg D J, Moore A S, Beeman B V, Eckart M J, Grim G P, Hartouni E P, Hatarik R, Rubery M S, Sayre D B and Waltz C 2018 *Ab initio* response functions for Cherenkov based neutron detectors *Rev. Sci. Instrum.* **89** 10I136

[230] Moore A S *et al* 2018 A fused silica Cherenkov radiator for high precision time-of-flight measurement of DT and neutron spectra *Rev. Sci. Instrum.* **89** 10I120

[231] Glebov V Y *et al* 2018 Testing a Cherenkov neutron time-of-flight detector on OMEGA *Rev. Sci. Instrum.* **89** 10I122

[232] Batha S H, Volegov P L, Fatherley V E, Geppert-Kleinrath V and Wilde C H 2018 Optimizing neutron imaging line of sight locations for maximizing sampling of the cold fuel density in Inertial Confinement Fusion implosions at the national ignition facility *Rev. Sci. Instrum.* **89** 10I147

[233] Casey D T, Volegov P L, Merrill F E, Munro D H, Grim G P, Landen O L, Spears B K, Fittinghoff D N, Field J E and Smalyuk V A 2016 Fluence-compensated down-scattered neutron imaging using the neutron imaging system at the national ignition facility *Rev. Sci. Instrum.* **87** 11E715

[234] Volegov P L, Danly C R, Merrill F E, Simpson R and Wilde C H 2015 On three-dimensional reconstruction of a neutron/x-ray source from very few two-dimensional projections *J. Appl. Phys.* **118** 205903

[235] Volegov P L, Danly C R, Fittinghoff D, Geppert-Kleinrath V, Grim G, Merrill F E and Wilde C H 2017 Three-dimensional reconstruction of neutron, gamma-ray, and x-ray sources using spherical harmonic decomposition *J. Appl. Phys.* **122** 175901

[236] Frenje J A *et al* 2016 The magnetic recoil spectrometer (MRSt) for time-resolved measurements of the neutron spectrum at the national ignition facility (NIF) *Rev. Sci. Instrum.* **87** 11D806

[237] Hilsabeck T J, Frenje J A, Hares J D and Wink C W 2016 A stretch/compress scheme for a high temporal resolution detector for the magnetic recoil spectrometer time (MRSt) *Rev. Sci. Instrum.* **87** 11D807

[238] Parker C E *et al* 2018 Implementation of the foil-on-hohlraum technique for the magnetic recoil spectrometer for time-resolved neutron measurements at the national ignition facility *Rev. Sci. Instrum.* **89** 113508

[239] Wink C W, Frenje J A, Hilsabeck T J, Bionta R, Khater H Y, Gatu Johnson M, Kilkenny J D, Li C K, Séguin F H and Petrasso R D 2016 Signal and background considerations for the MRSt on the national ignition facility (NIF) *Rev. Sci. Instrum.* **87** 11D808

[240] Fatherley V E, Fittinghoff D N, Hibbard R L, Jorgenson H J, Martinez J I, Oertel J A, Schmidt D W, Waltz C S, Wilde C H and Volegov P L 2018 Aperture design for the third neutron and first gamma-ray imaging systems for the national ignition facility *Rev. Sci. Instrum.* **89** 10I127

[241] Dymoke-Bradshaw A K L, Hares J D, Milnes J, Herrmann H W, Horsfield C J, Gales S G, Leatherland A, Hilsabeck T and Kilkenny J D 2018 Development of an ultra-fast photomultiplier tube for gamma-ray Cherenkov detectors at the national ignition facility (PD-PMT) *Rev. Sci. Instrum.* **89** 10I137

[242] Geppert-Kleinrath H *et al* 2018 Pulse dilation gas Cherenkov detector for ultra-fast gamma reaction history at the NIF *Rev. Sci. Instrum.* **89** 10I146

[243] Kim Y *et al* 2012 Gamma-to-electron magnetic spectrometer (GEMS): an energy-resolved γ-ray diagnostic for the national ignition facility *Rev. Sci. Instrum.* **83** 10D311

[244] Sutcliffe G *et al* 2018 Development and utilization of the DT^{3}He multi-particle backlighter for stopping-power experiments and for radiography of strong fields at the NIF *Bull. Am. Phys. Soc., Div. Plasma Phys.* **63** 11